




12-2012

Confinement Effects of Solvation on a Molecule Physisorbed on a Metal Particle

Jacob Fosso Tande
jtande@utk.edu

Follow this and additional works at: https://trace.tennessee.edu/utk_graddiss

 Part of the [Biological and Chemical Physics Commons](#), [Materials Chemistry Commons](#), and the [Physical Chemistry Commons](#)

Recommended Citation

Fosso Tande, Jacob, "Confinement Effects of Solvation on a Molecule Physisorbed on a Metal Particle. " PhD diss., University of Tennessee, 2012.
https://trace.tennessee.edu/utk_graddiss/1582

This Dissertation is brought to you for free and open access by the Graduate School at TRACE: Tennessee Research and Creative Exchange. It has been accepted for inclusion in Doctoral Dissertations by an authorized administrator of TRACE: Tennessee Research and Creative Exchange. For more information, please contact trace@utk.edu.

To the Graduate Council:

I am submitting herewith a dissertation written by Jacob Fosso Tande entitled "Confinement Effects of Solvation on a Molecule Physisorbed on a Metal Particle." I have examined the final electronic copy of this dissertation for form and content and recommend that it be accepted in partial fulfillment of the requirements for the degree of Doctor of Philosophy, with a major in Chemistry.

Robert J. Harrison, Major Professor

We have read this dissertation and recommend its acceptance:

Robert J. Hinde, Charles Feigerle, Bobby G. Sumpter

Accepted for the Council:

Carolyn R. Hodges

Vice Provost and Dean of the Graduate School

(Original signatures are on file with official student records.)

Confinement Effects of Solvation on a Molecule Physisorbed on a Metal Particle

A Dissertation

Presented for the

Doctor of Philosophy

Degree

The University of Tennessee, Knoxville

Jacob Fosso Tande

December 2012

© by Jacob Fosso Tande, 2012
All Rights Reserved.

I would like to dedicate this doctoral thesis to my grand parents, Kamla Augustin Marcel and Kengne Marie Josephe for taking very good care of me in my early days of life and setting my path to English education while my parents went for studies. A special dedication to my mother, Toussi Berthe, for instilling the virtues of patience and hardwork in me

Acknowledgements

It would not have been possible to accomplish this work without the help and support of the great people around me, to only some of whom it is possible to mention here. Above all, I would like to thank my wife Valerie, my daughter Angela-Grace, and my son Benjamin for their personal support and great patience at all times. My parents, brothers and sisters have given me their relentless support throughout, as always, for which my mere expression of thanks likewise does not suffice.

This thesis would not have been possible without the help, support and patience of my supervisor, Prof. Robert J. Harrison, not to mention his advice and unsurpassed mastery of computational sciences. His support has been invaluable on both an academic and a personal level, for which I am extremely grateful. My sincere gratitude to Prof. Robert J. Hinde, Prof. Charles Feigerle and Dr. Bobby G. Sumpter for accepting to serve on my thesis committee.

I would like to thank all the members of the Harrison research group for their all-time support and for providing a conducive environment for learning. I acknowledge the financial, academic and technical support of the Department of Chemistry at the University of Tennessee, Knoxville. The library facilities (notably the Hodges library) and computer facilities of Oak Ridge National Laboratory have been indispensable. I am most grateful to Prof. Janice L. Musfeldt for giving me the opportunity to provide computational support to her research group and her Postdoctoral research associate, Dr. O. Gunaydin-Sen, for providing me with the experimental data of the biradical.

Progress is never made by those who fall on their back as a cockroach

Abstract

We describe and present results of the implementation of the surface and volume polarization for electrostatics (SVPE) and the iso-density surface solvation models. Unlike most other implementation of the solvation models where the solute and the solvent are described with multiple numerical representation, our implementation uses a multiresolution, adaptive multiwavelet basis to describe both solute and the solvent. This requires reformulation to use integral equations throughout as well as a conscious management of numerical properties of the basis.

Likewise, we investigate the effects of solvation on the static properties of a molecule physisorbed on a spherical particle, modeled as a polarizable continuum colloid with a static dielectric constant. The effective polarizability of the physisorbed molecule is enhanced by a factor of 10^5 in vacuo and by only 10^2 when solvated. The variation of the polarizability of the molecules with respect to the changes in their environment illustrates the importance of electrostatic interaction in the enhancement of the effective polarizability.

Finally, we investigated the optical properties of 1,4-phenylenedinitrene and 4,4'-stilbenedinitrene biradical molecules. Using our computational model, we establish the structure property relationship in biradical organic compounds. The spin splitting is shown to be inversely proportional to the separation between the two spin carrying centers and is partly driven by the coulombic interaction. The intense peaks on the absorption spectra is the result of the mixing of transitions from the spin carrying centers with those of π (pi) origin.

Contents

1	Introduction	1
1.1	Electrostatics of Macroscopic Media	2
1.2	Dielectric Functions	3
1.3	Surface-Enhanced Raman Spectroscopy:brief background	5
1.4	Molecular Interactions in Solution	8
1.5	Free Radicals: brief background	10
1.5.1	Magnetic Field Interaction and Spin Splitting	11
1.6	Dinitrene Biradicals	13
2	Many Body Methods	15
2.1	The Hartree-Fock Method	16
2.2	Density Functional Theory	17
2.3	Time-dependent Density Functional Theory	19
2.4	Multi-configuration Self-consistent Field	21
2.5	Numerical Environment	21
2.5.1	Basis Sets	22
2.5.2	Multi-resolution Multi-wavelet Fundamentals	23
3	Polarizable Continuum Electrostatic Solvation Models	25
3.1	Molecular Volume and Surface	25
3.1.1	Computed Volume and Surface	27
3.1.2	Molecular Volume and Surface from Soft Spheres	28

3.2	The Iso-density Cavity	30
3.3	Solving The Poisson's Equation	32
3.3.1	Interlocking Spheres	32
3.3.2	Iso-density Cavity	38
3.3.3	Electrostatic Potential	41
3.4	Solute-solvent Reaction	42
3.4.1	The Solute-solvent Reaction Potential	42
3.4.2	Electrostatic Free Energy of Solvation	46
3.4.3	Cavitation Energy	47
3.5	Results and Discussion	49
3.5.1	Molecular Surface and Volume Results	49
3.5.2	SVPE and Iso-density Results	52
3.6	Conclusion	59
4	Gauging Environmental Effects with Static Properties	60
4.1	Molecule in Uniform Static Electric Field	61
4.2	Permanent and Induced Molecular Dipole in a Uniform Static Electric Field	63
4.2.1	Calculating the Electric Polarizability	65
4.3	Molecule Physisorbed on a Polarizable Continuum Colloid	69
4.3.1	Polarizable Continuum Colloid	69
4.3.2	Physisorption Model	71
4.4	Solving Poisson's and Laplace's Equations	73
4.5	Static Properties of Physisorbed Molecule	79
4.6	Results and Discussion	82
4.6.1	Physisorbed Molecules	87
4.6.2	Solvated and Solvated-Physisorbed Molecule	91
4.6.3	Environmental Effects	95
4.7	Conclusion	97

5 Tunability of the Singlet-Triplet Equilibrium in Organic Biradical Compounds	98
5.1 Chemical Systems	99
5.2 Computational Method	100
5.3 Results and Discussion	103
5.3.1 Active Spaces	103
5.3.2 Spin splitting	107
5.3.3 Vertical Excitations and Frequency Analysis	112
5.3.4 Structure Property Relationship	116
5.4 Conclusion	126
6 Conclusions	127
Bibliography	131
Appendix	140
Vita	156

List of Tables

3.1	Molecular surface area of some selected molecules compared to the molecular surface areas computed using hard spheres and iso-density methods. The SVPE surface areas are computed with a surface width of 0.3 and areas are reported in atomic units, squared	51
3.2	Molecular volume of some selected molecules compared to the molecular volumes computed using hard spheres and iso-density methods. The SVPE volumes are computed with a surface width of 0.3 and volumes are reported in atomic units cubed	52
3.3	SVPE solvation free energy (at the RHF with a threshold of 10^{-4} and $\sigma = 0.3$). The total solvation free energy (ΔG_{sol}) is the sum of the electrostatic free energy (ΔG_{elec}) of solvation, and the cavitation free energy (ΔG_{cav}). The free energies are in kcal/mol and a dielectric constant of 78.304 for water is used through out. Our results are compared to the experimental values (ΔG_{expt}) [100, 101] and the literature (electrostatic free energy) values (ΔG_{lit}) [99]	53

3.4	Iso-density solvation free energy (at the RHF with a threshold of 10^{-4} , $\beta = 1.3$ and $\rho_0 = 0.001 a.u/a_0^3$). The total solvation free energy (ΔG_{sol}) is the sum of the electrostatic free energy (ΔG_{elec}) of solvation, and the cavitation free energy (ΔG_{cav}). The free energies are in kcal/mol and a dielectric constant of 78.304 for water is used throughout. Our results are compared to the experimental values (ΔG_{expt}) [100, 101] and the literature (electrostatic free energy) values (ΔG_{lit}) [99]	56
4.1	Components of the dipole moment and the polarizability of Hydrogen Fluoride at different magnitudes of the static electric field. The components are computed with the dipole method at a threshold of 10^{-6}	82
4.2	Components of the second hyper-polarizability of Hydrogen Fluoride at different magnitude of the static electric field. The components are computed with the dipole representation at a threshold of 10^{-6}	83
4.3	Components of the first hyper-polarizability of Hydrogen Fluoride at different magnitude of the static electric field. The components are computed with the dipole method at a threshold of 10^{-6}	84
4.4	Components of the dipole moment and the polarizability of Hydrogen Fluoride at different magnitudes of the static electric field. The components are computed with the energy method at a threshold of 10^{-6}	85
4.5	The dipole moment, and selected components of polarizability of Hydrogen Fluoride compared to other methods [94]. The components are computed with an electric field magnitude $E_0 = 0.001$ a.u.	86

4.6	<p>Static properties of physisorbed pyridine. Effective polarizability α_{eff}, the mean polarizability α_m, the components of polarizability α_{ii} ($i \in \{x, y, z\}$), the enhancement I, the average reaction electric field, F_{cf}, from the polarization of the spherical PCC (with radius of 10.0 Å) by the external field ($E_0 = 0.001$ a.u), and the average reaction electric, F_{cm}, from the interaction of the molecule with the spherical PCC. pyridine is described at the restricted Hartee-Fock level of theory with a threshold of 10^{-4}. These values are computed at different PCC-pyridine separation, r (in Å).</p>	88
4.7	<p>Static properties of physisorbed methane. Effective polarizability α_{eff}, the mean polarizability α_m, the enhancement I, the average reaction electric field, F_{cf}, from the polarization of the spherical PCC (with radius of 10.0 Å) by the external field ($E_0 = 0.01$ a.u), the average reaction electric field, F_{cm}, from the interaction of the molecule with the spherical PCC. The methane molecule is described at the restricted Hartee-Fock level of theory with a threshold of 10^{-6}. These values are computed at different PCC-methane separation, r (in Å).</p>	90
4.8	<p>Static properties of solvated-physisorbed pyridine. Effective polarizability α_{eff}, the mean polarizability α_m, the components of polarizability α_{ii} ($i \in \{x, y, z\}$), the enhancement I, the average reaction electric field, F_{cf}, from the polarization of the spherical PCC (with radius of 10.0 Å) by the external field ($E_0 = 0.001$ a.u), the average reaction electric, F_{cm}, from the interaction of pyridine with the spherical PCC, and the average reaction electric, F_{sm}, from the interaction of pyridine with the solvent. The pyridine molecule is described at the restricted Hartee-Fock level of theory with a threshold of 10^{-4}. These values are computed at different PCC-pyridine separation, r (in Å).</p>	93

4.9	Static properties of solvated-physisorbed methane. Effective polarizability α_{eff} , the mean polarizability α_m , the components of polarizability α_{ii} ($i \in \{x, y, z\}$), the enhancement I , the average reaction electric field, F_{cf} , from the polarization of the spherical PCC (with radius of 10.0 Å) by the external field ($E_0 = 0.001$ a.u), the average reaction electric, F_{cm} , from the interaction of methane with the spherical PCC, and the average reaction electric field, F_{sm} , from the interaction of methane with the solvent. The methane molecule is described at the restricted Hartee-Fock level of theory with a threshold of 10^{-4} . These values are computed at different PCC-solvated methane separation, r (in Å).	94
5.1	Spin splitting from the DFT (B3LYP, 6-311G*) geometry of the 1,4-phenylenedinitrene triplet with MCSCF single point at different active spaces. units are in Kelvin (kcal/mol) for the spin splitting and in Hartree (E_h) for the electronic state energies	107
5.2	Spin splitting from the MCSCF (CASSCF[10, 10], 6-311G*) geometry of the 1,4-phenylenedinitrene with MCSCF single point at different active spaces. units are in Kelvin (kcal/mol) for the spin splitting and in Hartree (E_h)for the electronic state energies	108
5.3	Inter-nuclear angles θ of the MCSCF(6-311G*) at CASSCF active spaces of [6, 6], [8, 8], [10, 10] for singlet(S), triplet(T) and triplet DFT geometries. For clarity, the MCSCF θ is indexed with the electronic state and the number of electrons.	109
5.4	Spin splitting from the MCSCF (CASSCF[6, 6], 6-31G*) geometry of the 4,4'-stilbenedinitrene singlet. The MCSCF/6-31G* single point calculations are carried out at the specified CASSCF active spaces. The units are Kelvin (kcal/mol) for the spin splitting, and Hartree for the electronic energies	110

5.5	Spin splitting from the DFT (B3LYP, 6-31G*) geometry of the 4,4'-stilbenedinitrene triplet. The MCSCF/6-31G* single point calculations are carried out at the specified CASSCF active spaces. The units are Kelvin (kcal/mol) for the spin splitting, and Hartree for the electronic energies	111
5.6	Spin splitting from different experimental techniques. The analysis method used to extract the spin gap is indicated in bracket: population (pop), and Beer's (Beer). The values in squared brackets correspond to the tuning parameter, The results are compared to the MCSCF results from [106] and this work	111
5.7	Configuration state functions (ψ_I). I is the state function index, \hat{H} is the Hamiltonian, $\langle S^2 \rangle$ is the electron spin expectation value and n_1 and n_2 are the occupation numbers of the orbitals.	118
5.8	Transition dipole moments (X, Y) of singlet 4,4'-stilbenedinitrene for selected transitions, at computed wavelength (λ) with the squared dipole oscillator strength (μ^2 , in atomic units)	121
5.9	Transition dipole moments (X, Y) of triplet 4,4'-stilbenedinitrene for selected transitions, at computed wavelength (λ) with the squared dipole oscillator strength (μ^2 , in atomic units)	121
5.10	Non-zero matrix elements, from integral simplification, of the Hartree-Fock equation. We observe that $\langle aa aa \rangle > \langle aa bb \rangle > 0$	122
5.11	Vibrational fine structure extracted from the absorption difference data of the 1,4-phenylenedinitrene biradical (supporting material of [34]) compared with B_u symmetry mode frequencies and assignments from MCSCF-CASSCF (10, 10)/ 6-311G* calculations. The calculated frequencies correspond to the singlet state. Those of the triplet state were not much different.	125

List of Figures

1.1	The effects of a magnetic field on the energies of the α and the β species	11
3.1	Two interlocking spheres	26
3.2	The plots illustrates how $\Theta(\frac{s}{\sigma}) = \frac{1}{2} (1 + erf(\frac{s}{\sigma}))$ gets closer to a step function as $\sigma \rightarrow 0$	29
3.3	Two dimensional plot of the dielectric function $\epsilon[\rho(r)]$ along the x-component of the simulation cube	31
3.4	Two dimensional plot of the electronic charge distribution (in red) and the interlocking spheres cavity function (in blue) of the benzene molecule. The plot is along the x-component of the electronic charge distribution. A fraction of the electronic charge density is outside the molecular cavity.	35
3.5	Comparison of the norm of the log-derivative of the dielectric function for the two forms of the switching function (linear (3.16) and exponential (4.39)) for $\sigma = 0.2$ and $\epsilon_{\infty} = 78$.	36
3.6	Two dimensional plot of the surface charge distribution $\Sigma(r)$ on the interlocking spheres cavity for the benzene molecule. The charge distribution is zero everywhere except on the molecular cavity surface. The plot is along the x-component of the electronic charge distribution	37

3.7	Two dimensional plot of the surface charge distribution $\Sigma(r)$ of the benzene molecule for the iso-density method. The surface charge distribution is an outcome of polarization and is represented by the second term on the RHS of Eq. 3.29. The plot is along the x-component of the electronic charge density.	38
3.8	Two dimensional plot of the quotient of the functional derivative of $\epsilon[\rho(r)]$ with respect to ρ by $\epsilon[\rho(r)]$. Computation is carried out point-wise to control numerical noise.	39
3.9	Two dimensional plot of the functional derivative of $\epsilon[\rho(r)]$ with respect to ρ . The use of cutoff value on electronic density is not enough to eliminate numerical noise.	40
3.10	Two dimensional plot of the total electrostatic potential of the benzene molecule for the iso-density method. The plot is done along the z-axis	41
3.11	Two dimensional plot of the solute-solvent electrostatic reaction potential of the benzene molecule for the iso-density method. The plot is along the x-axis of the simulation cube.	43
3.12	Two dimensional plot of the solute-solvent electrostatic reaction potential of the benzene molecule for the SVPE method. The plot is along the x-axis of the simulation cube.	43
3.13	Two dimensional plot of the solute-solvent electrostatic reaction potential (in red) and the interlocking sphere cavity function of the benzene molecule (in blue).The surface and volume electrostatic potentials are accounted for and are indistinguishable. The plot is along the x-component of the simulation reference.	44
3.14	Parameterizing the molecular cavity of H_2O molecule. σ is the surface width. The surface area decreases with the surface width	55

3.15	Regression analysis of the iso-density solvation model. (a) shows the correlation between calculated (ΔG_{cal}) and the experimental (ΔG_{expt}) solvation free energies, (b) shows the correlation between calculated (ΔG_{cal}) and the literature values of (ΔG_{lit}) solvation free energies, and (c) shows the correlation between calculated (ΔG_{cal}) and the literature values of the cavitation free energy	57
4.1	Polarizable continuum colloid. The colloid-like particle is made up of six interlocking spheres	70
4.2	Polarizable continuum colloid. The colloid-like particle is single sphere of radius 10.0\AA	70
4.3	Convergence study of the total internal energy (E_{int} in a.u.) of water molecule physisorbed on spherical dielectric particle of radius 18.89a.u. The variation of the internal energy is small for a dielectric constant value between 500 and 1600 ($\Delta E_{int} \approx 10^{-4} kcal/mol$).	72
4.4	Convergence study of the physisorption free energy of water molecule physisorbed on spherical dielectric particle of radius 18.89a.u. The distance from the center of nuclear charge of the water molecule to the sphere's surface is 3.778a.u.	74
4.5	Schematic representation of the spherical polarizable continuum colloid. The sphere is polarized by an external electric E_0 . Positive and negative charges are induced on the sphere such that the total surface induced charge is zero.	75
4.6	Exact and computed reaction potential near the PCC (from Laplace's equation) due to the external electric field.	77
4.7	Exact and computed reaction potential near the solvated PCC (from Laplace's equation) due to the external electric field.	77

4.8	Schematic representation of a pyridine molecule physisorbed on spherical polarizable continuum colloid. The molecule and the sphere are in a uniform external electric field (E_0). pyridine and the PCC are held close to each other by the coulombic interactions (here represented as dotted lines)	87
4.9	Schematic representation of a methane molecule physisorbed on spherical polarizable continuum colloid.	91
4.10	Environmental effects on the polarizability of pyridine and methane. (a) and (b) are the effective polarizability (α_{eff}) of the pyridine and methane molecules physisorbed on a spherical PCC. (c) and (d) are the effective polarizability of the solvated pyridine and solvated methane molecules physisorbed on a spherical PCC. (d) is the enhancement of the polarizability of the physisorbed pyridine molecule and (e) is the enhancement of the polarizability of the physisorbed solvated pyridine molecule on a spherical PCC. r (in \AA) is the separation between the molecule and the spherical PCC while I is the enhancement	95
5.1	(a) Chemical structure of the pristine organic precursor 4,4-diazidostilbene (blue) and the dinitrene biradical 4,4-stilbenedinitrene (red) after the photochemical reaction. (b) Energy level scheme showing the 1A_g singlet ground state and the low lying 3B_u triplet excited state of the dinitrene biradical [103]. The triplet state can be accessed with temperature and magnetic field.	99
5.2	(a) Chemical structure of the 1,4-diazidobenzene precursor (blue), the intermediate after partial photolysis (green), and the dinitrene biradical 1,4-phenylenedinitrene (red) after full photochemical reaction. (b) Energy level scheme showing the singlet ground state, low lying triplet, and the high lying quintet excited states of the biradical [103]	100

5.3	Spin configuration for a two electrons and two states scheme. The singlet state is a linear combination of two single reference Slater determinants. The triplet states (lower in energy with respect to the singlet) has one linear combination of two single reference Slater determinant and two single reference Slater determinants	101
5.4	MOLDEN plots of the active space orbitals used in the computations of 1,4-phenylenedinitrene.	105
5.5	MOLDEN plots of the active space orbitals used in the computations of 4,4'-stilbenedinitrene.	106
5.6	TDDFT and selected CI spectra (square of the transition dipole, μ^2 , in atomic units) of 1,4-phenylenedinitrene. For clarity, dipole-allowed transitions are indicated in black. Dipole-forbidden transitions are indicated in red as negative 0.1, weak allowed transitions are increased to 0.1, and intense transitions truncated to 0.5. The most intense feature in the singlet CI spectrum at 251 nm (predominantly $N \rightarrow N^*$ single excitation, with lesser $\pi \rightarrow \pi^*$ single excitation) has $\mu^2 = 12$ and does not appear in the triplet spectrum that has its most intense feature with $\mu^2 = 0.3$ at 162 nm. The spurious low energy features in the singlet TDDFT spectrum are omitted. N and N^* indicate the b_{1g} and b_{3u} orbitals, respectively	113

- 5.7 TDDFT spectra (square of the transition dipole, μ^2 , in atomic units) of 4,4'-stilbenedinitrene. For clarity, dipole-allowed transitions are indicated in black. Dipole-forbidden transitions are indicated in red as negative 0.1, weak allowed transitions are increased to 0.1, and intense transitions truncated to 0.5. The most intense feature in the triplet TDDFT spectrum occurs at 364 nm (equal contributions from $N \rightarrow N^*$ and $\pi \rightarrow \pi^*$ excitations) has $\mu^2 = 10.55$ and does not appear in the singlet spectrum that has its most intense feature with $\mu^2 = 1.607$ at 222.8489 nm. The spurious low energy features in the singlet TDDFT spectrum are omitted. N and N^* indicate the a_g and b_u singly occupied orbitals, respectively 114
- 5.8 Absolute value of the absorption difference, $|\Delta\alpha| = |\alpha(T) - \alpha(T = 5K)|$, vs. wavelength for the photolyzed biradical film at 80, 60, 40, and 20 K. Inset: Example Curie [34] fit at 520 nm. These data allow a direct comparison of electron paramagnetic resonance and optical methods of spin gap determination. The determined $\theta = 230 \pm 22K$, which compares well with that from electron spin resonance (288 K) . A schematic view of the calculated triplet state excitations using the TDDFT method (shown at the bottom) in reasonable agreement with the $|\Delta\alpha|$ data in the main panel. The fine structure in the absorption difference spectrum is discussed in the supplementary material 115

5.9 Molecular properties of 4,4'-stilbenedinitrene (**a**, **b**, **c**) and 1,4-phenylenedinitrene (**d**, **e**, **f**) (**a**) Electronic charge density distribution (contour spacing = 0.01) (**b**) Spin density distribution (contour spacing = 0.02) (**c**)Molecular electrostatic potential(contour spacing = 0.05) (**d**)Electronic charge density distribution (contour spacing = 0.05) (**e**) Spin density distribution (contour spacing = 0.01) and (**f**) Molecular electrostatic potential(contour spacing = 0.01). The electronic charge density of 1,4-phenylenedinitrene is uniformly distributed over the entire molecule whereas the bulk of the electronic charge density in 4,4'-stilbenedinitrene is accumulated over the spacer groups, between the nitrogen atoms. Spin density distribution is localized on the nitrogen atoms in both structures. In (c) and (f) the blue and red contours represent the positive and negative potentials respectively. 117

Chapter 1

Introduction

All chemical, biological and physical processes are influenced by their environment: a molecule is perturbed by the surface on which it is physisorbed, and solvents are known to provide environmental conditions for chemical reactions and electromagnetic interactions. In collaboration with experimentalists, theoreticians develop computational methods to gauge the environmental changes, provide explanations to experiment and give insight into those changes. In this work, the focus is on the development of a theoretical model to study solvent effects on molecules, and gauge environmental effects on a molecule physisorbed on a metal particle, with the metal particle represented as a polarizable continuum. The use of a polarizable continuum metal particle is motivated by the high computational cost involved in the full quantum mechanical representation of the metallic surface.

In the design and implementation of the methodology, we have taken into account the available computational resources, and have emphasized on the detailed description of the molecule while using a polarizable continuum to represent the environmental effects with the aim of capturing the experimental aspects as much as possible.

This work has been divided into six chapters. Chapter one is devoted to background material. In chapter two, we review the many-body method as related to

density functional theory and the Hartree-Fock method. Chapter three is dedicated to the polarizable continuum electrostatic solvation model. In chapter four, the environmental effects are analyzed using the static properties of molecules and in chapter five, we investigate the tunability of the singlet-triplet equilibrium in organic biradical materials.

1.1 Electrostatics of Macroscopic Media

The textbook by J. D Jackson [1], provides a comprehensive description of electrostatics in a macroscopic media. Atoms and molecules are the elements of the media of interest. When a uniform electric field is applied to a “well” of atoms or molecules, the electrons bound to the molecules or atoms respond to the applied field. The molecular charge density in this situation is distorted. In the absence of the field the thermal average multi-pole moment is zero and the dominant molecular multi-pole moment is the dipole (for a neutral molecule). An electric polarization \mathbf{P} (dipole moment per unit volume) is produced in the medium

$$\mathbf{P} = \sum_i N_i \langle \mathbf{p}_i \rangle, \quad (1.1)$$

where $\langle \mathbf{p}_i \rangle$ is the average thermal dipole moment of the *ith* type of molecule and N_i is the average number of the *ith* type of molecule per unit volume. If the molecules have a net charge e_i and a macroscopic excess charge ρ_{excess} , the total charge at the macroscopic level will be defined as

$$\rho = \sum_i N_i \langle e_i \rangle + \rho_{excess}. \quad (1.2)$$

A potential ϕ and an electric field \mathbf{E} is derived from the total charge.

$$\mathbf{E} = -\nabla\phi \quad (1.3)$$

and

$$\nabla(\epsilon\mathbf{E}) = 4\pi[\rho - \nabla \cdot \mathbf{P}]. \quad (1.4)$$

Defining the electric displacement \mathbf{D} as follows:

$$\mathbf{D} = \epsilon\mathbf{E} + 4\pi\mathbf{P}, \quad (1.5)$$

and combining Eq. 1.4 and Eq. 1.5 we obtain

$$\nabla \cdot \mathbf{D} = 4\pi\rho. \quad (1.6)$$

If the uniform medium does not fill the entire space but has different media juxtaposed, then boundary conditions are considered on \mathbf{E} and \mathbf{D} at the interfaces between the media. The boundary conditions is such that the following equations are satisfied:

$$(\mathbf{D}_2 - \mathbf{D}_1) \cdot \hat{\mathbf{n}}_{21} = 4\pi\sigma \quad (1.7)$$

and

$$(\mathbf{E}_2 - \mathbf{E}_1) \times \hat{\mathbf{n}}_{21} = 0. \quad (1.8)$$

1 and 2 stand for regions 1 and 2, n_{21} is the normal to the surface directed from region 1 to region 2, and σ is the macroscopic surface charge density at the boundary surface.

1.2 Dielectric Functions

The dielectric function of a material depends on the changes that occur when the material is subjected to an electric disturbance. In this section we will look at the response of the material to electromagnetic radiation. Typically, polarization is the main response of materials to electromagnetic radiation. The polarizabilities of molecules can be divided into three parts: electronic polarizability (α_e) which is caused by the redistribution of electrons over atoms (for molecules), geometric

polarizability caused by the change in molecular geometry, and finally orientational polarizability which is the realignment of the molecule by an electric field.

To illustrate polarizability from which the dielectric function is obtained, we assume that an electron is harmonically bound to a particular location in the atom. The classical equation of motion of this electron is defined by the differential equation

$$m \left(\ddot{r} + \frac{\dot{r}}{\tau} \right) = -Kr - eE. \quad (1.9)$$

where $-Kr$ is the restoring force and E is the perturbing electric field. By setting $E \propto e^{i\omega t}$, $K = m\omega_0^2$, and $r \propto e^{i\omega t}$, the proposed solution to the differential equation is

$$r = \frac{-eE/m}{-\omega^2 + i\omega/\tau + \omega_0^2} \equiv -\frac{P}{e}, \quad (1.10)$$

The dipole moment of the atom will be $p = -er$ and the polarization $P = Np = -Ner \equiv N\alpha_e E$ N is the number of electrons. The frequency dependent polarizability is naturally obtained as follows:

$$\alpha_e = \frac{(e^2/m) [\omega_0^2 - \omega^2 - i\omega/\tau]}{(\omega_0^2 - \omega^2)^2 + (\omega/\tau)^2}. \quad (1.11)$$

From the electric displacement $\epsilon E = E + 4\pi P$ the dielectric function is defined as $\epsilon = 1 + 4\pi N\alpha_e$. The frequency dependent dielectric function then follows:

$$\epsilon(\omega) = 1 + \frac{(4\pi Ne^2/m) [\omega_0^2 - \omega^2 - i\omega/\tau]}{(\omega_0^2 - \omega^2)^2 + (\omega/\tau)^2}. \quad (1.12)$$

In metals (e.g Drude model) the electrons are free. The restoring force vanishes (i.e $k \rightarrow 0$, or $\omega_0 = 0$) and the electronic polarizability is simplified as follows:

$$\alpha_e = \frac{e^2/m}{-\omega^2 + i\omega/\tau}. \quad (1.13)$$

The frequency dependent polarizability is also simplified to

$$\epsilon(\omega) = 1 + \frac{\omega_p^2}{\omega^2 - i\omega/\tau}. \quad (1.14)$$

The metallic dielectric function can be separated into the real and imaginary parts:

$$R\epsilon(\omega) = 1 - \frac{\omega_p^2\tau^2}{1 + \omega^2\tau^2}, \quad (1.15)$$

and

$$I\epsilon(\omega) = -\frac{\omega_p^2\tau^2}{\omega\tau(1 + \omega^2\tau^2)}. \quad (1.16)$$

where ω_p is the plasmon (oscillating electron cloud) frequency, ω_0 is the frequency of the restoring force on the bound electrons, τ is the relaxation time and is a measure of the duration of the excited state.

1.3 Surface-Enhanced Raman Spectroscopy:brief background

In 1974 Fleischman observed an unusual intensity of Raman signal for pyridine adsorbed on an electro-chemically roughened silver electrode [15]. He attributed the unusual signal to the increased surface area of the electrode. This observation constituted the starting point for the spectroscopic method which is now known as surface-enhanced Raman scattering. Eventually, significant steps were made in providing experimental and theoretical explanations to Fleischman's observation (Martin Moskovits called them the discovery of SERS). In 1977, Jeanmarie and Van Duyne [3] and Albrecht and Creighton [16] began the discovery process when they separately pointed out that the huge increase in effective Raman cross section could not have been from an increase in the number of molecules on the roughened surface. The apogee of discovery was reached in 1978 when Martin Moskovits made the

remarkable observation that the huge increase in effective Raman cross section was as result of the excitation of surface plasmons [19]. Building on the observation and explanations afore mentioned, many other researchers investigated SERS. Kneipp and coworkers [8, 9, 10, 11, 12, 7] and Nie and coworkers [20, 21, 23, 24, 2, 6] simultaneously and independently reported the possibility of single molecule detection by SERS on the condition of intense enough SERS emissions. Moskovits proposal was significant in making a number of predictions such as the expectations of SERS in metal colloids and the establishment of the hierarchy of intensification for SERS active materials. Silver and alkali metals are now known to provide the most intense SERS signals followed by gold and copper. Other good conductors such as aluminum, indium, platinum, and transition metals provide SERS signals as well.

SERS activities are globally defined by two main mechanisms, which are electromagnetic (originating from the electromagnetic radiation) and electronic (defined by the electronic structure of SERS active materials as well as that of the physisorbed/chemisorbed molecule) in nature. Many SERS experiments are aimed at maximizing these mechanisms while theoretical or computational models lay emphasis on one or the other and sometimes on both. The SERS active material is sometime treated as a perfect mirror and the molecule as a point dipole [4] whose image self-triggers a multi-pole moment of infinite order. In some other description the physisorbed molecule is described as a point dipole and the SERS active material described with the jellium model [17] giving it a description which is more realistic than a reflecting mirror. One other popular approach consist of detailed *ab initio* description of the molecule interacting with a metal cluster made up of a few atoms. This method, though it accounts for chemisorption effects, the small metal cluster falls short of reproducing the bulk behavior of the SERS-active material which for a nanosized metal particle is made up of thousands of atoms. S. Corni and J. Tomasi [18] recognized the difficulty of accounting for chemisorption effects while retaining the bulk behavior of SERS-active material. They proposed a model in which the molecule is not chemically bound but is physisorbed on a SERS-active material,

that is described as a continuous body characterized by electric response properties. The solute charge density is *a priori* computed as a sum over occupied molecular atomic orbitals, each typically represented as a superposition of Gaussian-type basis function. The most complex part of the computation follows with a discretization of the cavity encapsulating the continuous body, representation of the surface charge (or reaction field) in basis on the cavity and finally solution of the integral equation.

Electromagnetic and electronic mechanisms alone are not sufficient for an efficient and complete SERS process. The molecule or analyte must be held in a suitable position that allows for maximum exposure to SERS emissions. Electrostatic interaction is the fixing mechanism that keeps the analyte in a suitable position for SERS probing. Nano-materials destined for SERS activities are often coated with charged capping materials. Chemical reducing agents such as sodium citrate, sodium borohydride, hydrazine, and hydroxylamine hydrochloride are adsorbed on the nanoparticle surface giving it a negative charge [14]. Synthesis of positively charge silver nanoparticles have also been reported [22]. Electrostatic-customized nanoparticles will attract and fix ions of opposite charges for an efficient SERS process. Furthermore, electro-chemical studies emphasize what happens once the molecule is on the electrodes neglecting the role of electrostatic interactions in drawing molecules to the places where surface plasmon resonance enhancements will produce signals.

We develop a theoretical model in which the molecule is physisorbed on a SERS-active material, described as a continuous body characterized by electric response properties, and puts into evidence the contribution of electrostatic interactions to SERS activities. This model uses the same adaptive multi-wavelet basis functions representation of the solute and the continuous body, thereby, within the user specified precision, eliminating basis set error.

1.4 Molecular Interactions in Solution

A realistic simulation of the chemical, biological and physical processes, requires the effects of solvation to be included. A solution can be defined *prima facie* as a large assembly of molecules held together by non-covalent interactions. Under this definition, the investigation of such interactions in physical systems of increasing complexity, should begin with dimers, continue through larger clusters and end with solutions. An alternative way of investigating such interactions in physical system is an explicit description of a subunit of the whole solution (the solute) and representing the other components (the solvent) with an interaction potential. This alternative way is commonly known as the implicit solvation model. In contrast to other theoretical approaches to studying solvation, implicit solvation models have substantially evolved to become standard. The theoretical approaches to studying liquid systems can be classified into four main categories as defined by Jacopo Tomasi and Maurizio Persico [59], (a) methods based on elaboration of physical function, (b) methods based on computer simulation of liquids (c) methods based on the continuum (electrostatic) model, and (d) methods based on the super-molecule description of the solution.

The use of an explicit or implicit model depends upon the solvation properties to be probed. Explicit solvation requires a full representation of the electronic structure of the solvent molecules with computational cost of explicit-solvation simulation increasing non-linearly with the number of solvent molecules plus averaging over the degrees of freedom of the molecules [38]. The explicit treatment of the solvent is necessary in situations where the solute is subjected to the average solvent effects (e.g ethanol in cyclohexane). Electrostatic effects of solvation dominates this interactions. The implicit solvation model is therefore more appropriate. The implicit solvation model focuses on describing the electronic structure of the encapsulated solute while describing the solvent environment as an unstructured polarizable dielectric continuum residing outside of the solvation capsule. A typical implicit solvation

model will have two main contributions to its solvation free energy — the electrostatic and the cavitation free energies of solvation. Dispersion repulsion is often considered especially for non polar solutes.

Multitudes of formulations exist to more or less rigorously solve the Poisson equation for a complicated solute cavity to determine the reaction potential. The formulations differ in how the quantum mechanical description of the solute is related to the classical mechanical description of solvent environment. One popular way consists of solving the Poisson’s equation for an apparent surface polarization charge density lying exclusively on the solvent cavity. These formulations are grouped under a variety of appellations and acronyms ranging from the surface polarization of the electrostatics(SPE) or polarizable continuum model (PCM) to the dielectric polarizable continuum model (DPCM) [39, 40, 41, 42, 43, 44, 45, 46, 47, 48, 49, 50, 51]. The assumption that the polarization charge density is exclusively on the surface is a simplification of the solvent environment and the quantum mechanical charge distribution. The other popular way of formulating the solvation method is more general and fully represent the effects of the quantum mechanical charge distribution on the solvent environment that consist of both surface and volume polarizations. The volume polarization results from the tail of the electronic charge density extending into the solvent environment with full solution of the relevant Poisson equation. The generalized methods are often grouped and called surface and volume polarization for electrostatics (SVPE) [52, 53, 56, 57, 58]. The solute charge density is *a priori* computed as a sum over occupied molecular atomic orbitals each typically represented as a superposition of Gaussian-type basis functions. From this and the nuclear charges, the electronic and total potential are computed. The most complex part of the computation then ensues with discretization of the cavity surface, representation of the surface charge (or electric field) in basis on the surface (most simply piecewise constants), and finally solution of the appropriate integral equations.

1.5 Free Radicals: brief background

Radicals impact our lives in many ways. Our bodies make radicals, radicals are produced when we light a fire or drive a car. We also use products (plastics) that are produced from a large scale via radical reactions. The aging process is also impacted by radicals. A radical is an atom or a compound that contains an unpaired electron and is described as “free radical” because it exists independently. Radicals are generally very reactive and are regarded as reactive intermediates. The reactivity in radicals is given by the instability of the unpaired; they pair to form low energy covalent bonds. A reverse process catalyzed by heat or light leads to bond breaking. A system with one unpaired electron, exists as a doublet with two degenerate states, represented as $(\psi_{\frac{1}{2},\frac{1}{2}}, \psi_{\frac{1}{2},-\frac{1}{2}})$, A double doublet is a system with two electrons, far enough apart so that the overlap of their spatial wave function is negligible. The wave function, a quantum mechanical concept, is used to illustrate the singlet and triplet electronic states. The total wave function for a set of particles such as the electron must be antisymmetric with respect to the interchange of the particles. For two non-interacting electrons, the symmetric ground state spatial wave function $\phi_a(1)\phi_a(2)$ must be multiplied by the antisymmetric singlet spin wave function to make the total wave function ${}^1\psi = \phi_a(1)\phi_a(2)\frac{1}{\sqrt{2}}(\alpha(1)\beta(2) - \beta(1)\alpha(2))$. The excited singlet state will be represented by ${}^1\psi^* = \frac{1}{\sqrt{2}}(\phi_a(1)\phi_b(2) + \phi_a(2)\phi_b(1))\frac{1}{\sqrt{2}}(\alpha(1)\beta(2) - \beta(1)\alpha(2))$. The triplet state involving ϕ_a and ϕ_b has an anti-symmetric spatial wave function and is multiplied by the symmetric spin wave functions (Eq. 1.17).

$$\begin{aligned} {}^3\psi^{*1,0} &= \frac{1}{\sqrt{2}}(\phi_a(1)\phi_b(2) - \phi_a(2)\phi_b(1))\frac{1}{\sqrt{2}}(\alpha(1)\beta(2) + \beta(1)\alpha(2)) \quad (1.17) \\ {}^3\psi^{*1,1} &= \frac{1}{\sqrt{2}}(\phi_a(1)\phi_b(2) - \phi_a(2)\phi_b(1))\alpha(1)\alpha(2) \\ {}^3\psi^{*1,-1} &= \frac{1}{\sqrt{2}}(\phi_a(1)\phi_b(2) - \phi_a(2)\phi_b(1))\beta(1)\beta(2) \end{aligned}$$

1.5.1 Magnetic Field Interaction and Spin Splitting

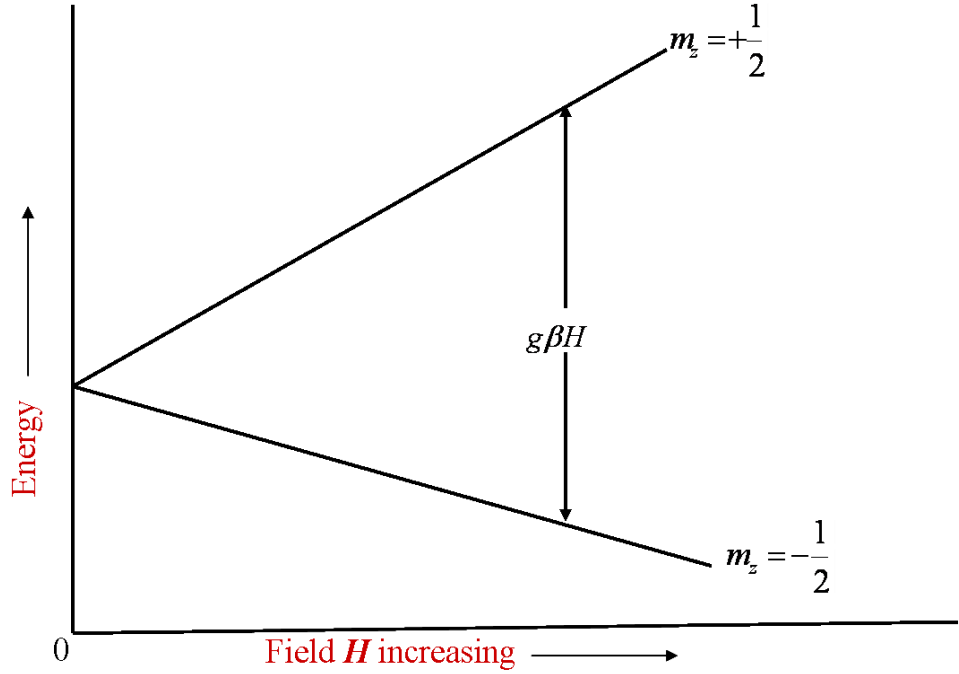


Figure 1.1: The effects of a magnetic field on the energies of the α and the β species

In the absence of a magnetic field, the two electron spin configurations, $(\psi_{\frac{1}{2},\frac{1}{2}}, \psi_{\frac{1}{2},-\frac{1}{2}})$, are degenerate and have the same energy. In a magnetic field however, the degeneracy is lifted. The difference in energy is the electronic Zeeman or fine splitting, it increases with the magnitude of the field. The magnetic field (B) interaction with the electron spin is represented by the spin Hamiltonian (H)

$$H = 2.00231\beta BS + D(S_z^2 - \frac{1}{3}S^2) + E(S_x^2 - S_y^2). \quad (1.18)$$

The first term of the Hamiltonian is the interaction of the total spin with the external field. The next two terms represent the dipole-dipole interaction. β is the electron Bohr magneton, E and D are the zero field parameters and hold information about the spatial distribution of the unpaired spins in the molecule. A large D means the average distance between the two electrons is small [25, 26]. In the triplet states of aromatic hydrocarbons, the orbitals occupied by the unpaired electron extend over the entire molecule. As a consequence D decreases with the number of aromatic rings [25, 26]. E is a measure of the deviation of the two electron distribution from cylindrical symmetry.

Up to this point, generalities about radicals have been covered. Going forward, a selective discussion of many-body systems will be the focus. The properties of many-body systems, depend a great deal on how the the electrons interact with each other and how apart they are from each other. The exchange integral K is an important predictor of radical behavior in a many-body system,

$$K = \langle \phi_a(1)\phi_b(2) | \frac{e^2}{r_{12}} | \phi_a(2)\phi_b(1) \rangle. \quad (1.19)$$

If $K = 0$, the electrons do not “see” each other’s spin, in this case the diradical is a double-doublet rather than triplet or singlet. For $K > 0$, the singlet and triplet states are distinct from each other. Furthermore, if ϕ_a is much lower in energy such that the lower state is almost purely ϕ_a and the upper almost purely ϕ_b . The resulting splitting will include energy contributions from these states (E_a, E_b),

$$E_{triplet} - E_{singlet} = E_b - E_a - 2K. \quad (1.20)$$

The value of K depends on the structural properties of the molecular system. In conjugated systems, if the flexibility of the molecule allows for a closer encounter between the sites holding the two unpaired electrons then the system will exhibit a strong exchange characteristic. In conjugated systems, the unpaired electrons

interact with each other and the exchange interaction is further enhanced if the system exhibit coplanarity. Conjugated dinitrene biradicals fall in this category; they have conjugated pi-system with inter-connected aromatic rings that favor coplanarity.

1.6 Dinitrene Biradicals

For decades, nitrenes (molecular fragments with unpaired electron on nitrogen) have been investigated. It is now well established that they are intermediates in the thermal or photo breakdown of phenyl-azides [27, 28, 29, 30]. The photolysis of aromatic azides is often investigated in organic matrices (at liquid nitrogen temperatures) ,in the process, stable nitrenes with distinctive absorption spectra are produced [31]. These nitrenes intermediates are precursors of the dinitrene biradical [31, 34], with the formation process occurring in two distinctive steps [33, 107]; the second step is twice as efficient as the first.

Trozzolo et al [33] established the ESR spectrum of 1,4-diphenylenedinitrene generated from 1,4-diazidobenzene thereby pioneering the first physical evidence of the existence of a bi-radical in its triplet electronic ground state with electron deficiencies on two separate atoms . Complexity surrounded the bi-radical formed: they are now known to be very unstable and will disappear when the organic matrix in which they are confined is exposed to a temperature as low as 90K [107].

Studies have been made to establish a structure-property relationship with the aim of controlling ground state multiplicity, which is critical to the design and synthesis of molecules with organic backbone and magnetic properties. Spin exchange and spin polarization are the two models generally consider to promote the bi-radical character in dinitrene. The discovery of the singlet ground state of dinitrene was a true theoretical test for the exchange model [35]. The conjugated pi-system in quinonoidal dinitrenes is responsible for the pi-spin polarization that promotes the indirect communication between the conjugatively separated unpaired electrons. Spin polarization or delocalization dilution through the addition of pi-conjugated

spacer group reduces the indirect communication between the conjugatively separated unpaired electrons [36, 37]. The outcome of a complete inhibition of communication between the unpaired spins is the existence of a non-interacting bi-radical very similar to that seen in unconjugated systems.

Furthermore, the zero field splitting of quinonoidals bi-radical is not consistent with what will normally be expected for unpaired electrons with pure bipolar interactions completely localized on the nitrogen atoms. The zero field splitting decreases as the distance between unpaired electrons is increased. The larger value is indicative of the fact that exchange interaction and spin polarization are both responsible for the indirect communication between the unpaired electrons [35]

Nonetheless, little or no information is available to explain the response observed when a magnetic field or photolysis is used to manipulate the singlet-triplet equilibrium populations. To extend our understanding of structure-property relationship, concomitantly providing a theoretical explanation to the magnetic and optical responses from the singlet-triplet equilibrium population manipulation, two simple models of electron configuration are used to explore the splitting mechanism in dinitrene biradicals. In the process, theoretical explanations are provided to the optical- and magnetic-spectral features.

Chapter 2

Many Body Methods

Very few electronic systems can be described in detail. Even a qualitative description is impossible, within the context of classical mechanics, because the electron is a very light particle with a mass close to zero. Quantum mechanics has emerged as the reliable method with which electronic structure can be described. Electronic structures become very difficult to describe as the number of electrons increase. The Schrödinger equation is the fundamental equation of quantum mechanics that describes the electron distribution in electronic systems. The time-independent Schrödinger equation in its simplest form is defined as

$$\hat{H}\psi = E\psi, \tag{2.1}$$

where \hat{H} is the Hamiltonian and ψ is the eigen function of the Hamiltonian. Solutions of Eq. 2.1 are obtained in two ways: without reference to experimental data (*ab initio*) and with reference to experimental data (semi-empirical).

Over the years, significant approximations (Born-Oppenheimer) have been introduced to simplify the complexity of the Schrödinger equation especially for molecular systems. In the light of these approximations, two popular methods have been consciously adopted in the Chemistry community, namely density functional

theory (DFT) and the *ab initio* hierarchy that start with Hartree-Fock (HF). Other static and dynamic methods are built on DFT and HF

2.1 The Hartree-Fock Method

The Hartree-Fock method is a variational method in which the wave functions of the many-electron system are represented as an anti-symmetrized product of the one-electron wave functions, commonly known as a Slater determinant Φ_{SD} ,

$$\Phi_{SD} = \frac{1}{\sqrt{N!}} \begin{vmatrix} \phi_1(1) & \phi_2(1) & \dots & \phi_N(1) \\ \phi_1(2) & \phi_2(2) & \dots & \phi_N(2) \\ \vdots & \vdots & \vdots & \vdots \\ \phi_1(N) & \phi_2(N) & \dots & \phi_N(N) \end{vmatrix}. \quad (2.2)$$

Φ_{SD} can be written in a simple form as follows:

$$\Psi_{SD}(\mathbf{x}_1, \dots, \mathbf{x}_N) = \frac{1}{N!} \sum_{\mathbf{P}} \epsilon_P \mathbf{P} \phi_1(\mathbf{x}_1) \dots \phi_N(\mathbf{x}_N), \quad (2.3)$$

where \mathbf{P} is the permutation operator that permutes the coordinates of the spin-orbitals only and not their labels (otherwise, there will be no effect). ϵ_P is -1 or $+1$ depending on whether the parity of the permutation is odd or even. The direct consequence of the anti-symmetry requirement is the *Pauli principle*, which states that no two electrons can have all quantum numbers equal.

The expectation value of the energy is calculated by applying the Hamiltonian (subject to the Born-Oppenheimer approximation) to the Slater determinant. The result is then minimized with respect to the spin-orbitals in the determinant. Writing the Hamiltonian as follows:

$$H = \sum_i h(i) + \frac{1}{2} \sum_{ij; i \neq j} g(i, j), \quad (2.4)$$

with

$$g(i, j) = \frac{1}{|\mathbf{r}_i - \mathbf{r}_j|} \quad (2.5)$$

and

$$h(i) = -\frac{1}{2}\nabla_i^2 - \sum_n \frac{Z_n}{|\mathbf{r}_i - \mathbf{R}_n|} \quad (2.6)$$

$h(i)$ is the one electron Hamiltonian and $g(i, j)$ is the two electron piece. r_i and r_j are the electron coordinates while Z_n and \mathbf{R}_n represent the the nuclei charge and the nuclei coordinates. The expectation value of the energy is obtained as follows:

$$E = \sum_k \langle \psi_k | h | \psi_k \rangle + \frac{1}{2} \sum_{kl} [\langle \psi_k \psi_l | g | \psi_k \psi_l \rangle - \langle \psi_k \psi_l | g | \psi_l \psi_k \rangle] \quad (2.7)$$

Eq. 2.7 is the energy functional and can be written in a simple form as

$$E = \sum_k \langle \psi_k | h + \frac{1}{2}(\mathbf{J} - \mathbf{K}) | \psi_k \rangle \quad (2.8)$$

\mathbf{J} is called the Coulomb operator and \mathbf{K} the exchange operator, obtained by interchanging the rightmost spin-orbitals of the Coulomb operator. The ground state of the many-electron system is obtained by minimizing Eq. 2.8 as a function of ψ_k subject to the $\langle \psi_k | \psi_l \rangle = \delta_{kl}$ constraint.

Setting $F = h + \mathbf{J} - \mathbf{K}$, the Fock operator F is defined and Eq. 2.9 is the Hartree-Fock equation which can be solved in a self consistent scheme as an eigenvalue problem. Λ_{kl} are the Lagrange multipliers interpreted as molecular orbital energies.

$$F \psi_k = \sum_l \Lambda_{kl} \psi_l \quad (2.9)$$

2.2 Density Functional Theory

Density functional theory (DFT) is based on the papers by Hohenberg [5] and Kohn and by Kohn and Sham [13] wherein they compare the density of the system to that

of a non-interacting particle system moving in a *local* potential $v_s(r)$, defined by the Kohn-Sham equations (in atomic units)

$$\left[-\frac{\nabla^2}{2} + v_s[\rho](r) \right] \phi_i(r) = \epsilon_i \phi_i(r) \quad (2.10)$$

$v_s[\rho](r)$ is a linear combination of three potentials: the external potential v_{ext} and the Hartree potential v_H , which is calculated from the density and the exchange correlation potential v_{xc} , the only unknown part of the Kohn-Sham (KS) equations.

$$v_s(r) = v_{ext}(r) + v_H(r) + v_{xc}(r) \quad (2.11)$$

The Kohn-Sham orbitals $\phi_i(r)$ experience the effective field, v_s , which is a functional of the electron density. The exact electronic charge density of the system is not known but can be calculated from the sum of the squares of the Kohn-Sham orbitals multiplied by their occupation numbers, n_i

$$\rho(r) = \sum_i^{occ} n_i |\phi_i(r)|^2 \quad (2.12)$$

The effective potential and the electronic charge density are interdependent, thus the KS-equations are solved in a Self-Consistent Field (SCF) scheme, which involves iteratively adjusting the density until the difference between the successive values of density and energy are within the defined threshold.

An approximation for the exchange correlation potential is required to solve the KS-equations, the simplest approximation being the Local Density Approximation (LDA). The Generalized Gradient Approximations go beyond just the density to take into account the gradient of the density, thus allowing for a much improved accuracy in the results for energies and geometries. Many other approximations based directly on the KS-orbitals are available.

2.3 Time-dependent Density Functional Theory

Ordinary DFT is restricted to ground-state problems, however excitation energy calculations within the ground-state DFT are possible through the so-called ∇SCF techniques [60, 61, 62, 63]. The latter technique has a less solid theoretical basis than the time-dependent density functional theory (TDDFT). Furthermore, molecular properties such as frequency-dependent polarizabilities, hyper-polarizabilities and their derivatives with respect to the vibrational modes of the molecule as well as the Van der Waals dispersion coefficients are either not easily accessible or not accessible at all using ∇SCF .

TDDFT is an extension of the ordinary DFT method, it starts from the time-dependent Kohn-sham (TDKS) equations, derived for first time by Runge and Gross [64]

$$i\frac{\partial}{\partial t}\phi_i(r,t) = \left[-\frac{\nabla^2}{2} + v_s(r,t) \right] \phi_i(r,t) \equiv F_s\phi_i(r,t) \quad (2.13)$$

where $v_s(r,t)$ is similar to its static counterpart, but for the fact that it is time dependent.

$$v_s(r,t) = v_{xc}(r,t) + v_H(r,t) + v_{ext}(r,t) \quad (2.14)$$

The Hartree potential $v_H(r,t)$ is explicitly defined as

$$v_H(r,t) = \int \frac{\rho(r_2,t)}{|r_1 - r_2|}. \quad (2.15)$$

The time-dependent exchange potential $v_{xc}[\rho](r,t)$ is an unknown functional of the time-dependent density, now defined as

$$\rho(r,t) = \sum_i^{occ} n_i |\phi_i(r,t)|^2. \quad (2.16)$$

Solving the TDKS equations iteratively, optimized Kohn-Sham (KS) orbitals are then used to compute and update the density. Solutions to the TDKS equation can be obtained perturbatively and non-perturbatively. The perturbative approach allows

for solutions of large systems and is the solution of interest. Considering the external potential $v_{ext}^{lm}(r, \omega)$, of general multi-pole form, and expanding the KS-equation to first order, the frequency dependent first-order correction to the density is derived. The coupling matrix $K_{ij\sigma,kl\tau}$ from the first order change in density matrix can be broken down into two components namely, a Coulomb $K_{ij\sigma,kl\tau}^{coul}$ and exchange and correlation $K_{ij\sigma,kl\tau}^{xc}$.

$$K_{ij\sigma,kl\tau} = K_{ij\sigma,kl\tau}^{coul} + K_{ij\sigma,kl\tau}^{xc} \quad (2.17)$$

The functional derivative of $v_{xc}^\sigma(r, t)$ with respect to $\rho_\tau(r', t')$, is defined as

$$f_{xc}^{\sigma\tau}(r, r', t - t') = \frac{\partial v_{xc}^\sigma(r, t)}{\partial \rho_\tau(r', t')} \quad (2.18)$$

if Eq. 2.18 is non zero only for $t = t'$, we have an adiabatic approximation, otherwise, it is a non-adiabatic approximation.

Choosing an appropriate exchange correlation functional, the real part of the response of the density to the external field is obtained as follows:

$$[\Delta - 2K](Re\partial P) = \partial v_{ext} \quad (2.19)$$

where Δ is a diagonal matrix. The real part of the first order correction to the density matrix P, gives access to the frequency-dependent polarizabilities [66, 64, 67]. For an excitation, the finite external perturbation ∂v_{ext} leads to an infinite change in density matrix such that $\Delta - 2K$ possesses zero eigenvalue at the excitation energy. After a unitary transformation, the eigenvalue equation from which the excitation energies and oscillator strengths are obtained [65]

$$\Omega F_i = \omega_i^2 F_i \quad (2.20)$$

where ω_i are the excitation energies and the oscillator strengths are obtained from the eigenvectors F_i . The Ω -matrix is split into singlet and triplet parts for spin restricted calculations.

2.4 Multi-configuration Self-consistent Field

Multi-configuration self-consistent field (MCSCF) is a type of configuration interaction (CI) method in which both the coefficients and the molecular orbitals (MOs) used in constructing the determinants are optimized. MCSCF calculations are smaller in size (with respect to the number of electrons) than the CI calculation, for the same system. MCSCF is generally used for calculations not treated well by HF such as for systems with multiple electronic configurations. Thus MCSCF is an extension of the single Hartree-Fock (HF) wave function that gives a qualitatively correct description of the electronic structure.

The major difficulty with MCSCF, is the selection of the necessary configuration to include for the property of interest. Many approaches have been proposed and the most popular among them is the complete active space self-consistent field method (CASSCF). The selection of the MOs to include in the active space is done manually, taking in to account the property to be determined and the computational cost. The MOs selected are usually some of the highest occupied MOs and the lowest unoccupied MOs from the RHF calculation. Within the active MOs a full CI is performed and all proper symmetry adapted configurations are included in the MCSCF optimization. MCSCF calculations therefore will need an initial guess, which is usually a RHF calculation or another MCSCF calculation.

2.5 Numerical Environment

Ab initio methods derive information by solving the Schrödinger's equation ideally without fitting experimental data. When necessary approximations are made,

including experimental data or simply a reformulation of Schrödinger’s equation. One of such approximation is the use of known functions to represent the unknown MOs. An infinite number of functions (known as basis functions) must be used for a complete representation of the MOs. Theoretical Chemistry, uses a numerical environment made up of complete and incomplete basis sets.

2.5.1 Basis Sets

There are two types of basis functions, commonly used in electronic structure calculations, namely: the Slater-type orbital (STO) [68] and the Gaussian-type orbital (GTO) [69]. The STOs have the functional form

$$\chi_{\zeta,n,l,m}(r, \theta, \varphi) = NY_{lm}(\theta, \varphi)r^{n-l}e^{-\zeta r} \quad (2.21)$$

N is the normalization constant, Y_{lm} are the spherical harmonic functions, r is the distance from the nucleus to the electron. The GTO on the other hand are represented with Gaussians or cartesian coordinates.

$$\begin{aligned} \chi_{\zeta,n,l,m}(r, \theta, \varphi) &= NY_{lm}(\theta, \varphi)r^{2n-2-l}e^{-\zeta r^2} \\ \chi_{\zeta,l_x,l_y,l_z}(X, Y, Z) &= NX^{l_x}Y^{l_y}Z^{l_z}e^{-\zeta r^2} \end{aligned} \quad (2.22)$$

The most important factor in MOs approximation is the number of functions to be used. The smallest number of functions possible is the minimal basis in which each occupied atomic orbital is represented by a single appropriate basis function. A better description of the electron distribution is done by changing the number of basis functions. This goes from doubling, tripling, quadrupling to quintupling the minimal basis. Other specialized functions are added for the purpose of including polarization, accounting for diffuse charge and electron correlation (functions with higher angular momentum). There are definitely many varieties of basis sets but our choice(s) should be guided by the nature of the calculations and the computational

cost. A new generation of basis sets is coming of age where the approximate existing basis sets are used as initial guess, after which they are projected onto a numerical basis set, themselves effectively complete. The Multi-resolution Adaptive Numerical Environment for Scientific Simulations (MADNESS) uses numerical-complete basis sets in its numerical framework.

2.5.2 Multi-resolution Multi-wavelet Fundamentals

MADNESS [70] is a general purpose package that provides a high-level environment for solving differential and integral equations in many dimensions using adaptive fast algorithm with guaranteed precision based on multi-resolution analysis and novel separated representation. MADNESS is designed in levels: at the lowest level is a petascale parallel programming environment that provides programmers productivity and code scalability while maintaining a backward compatibility with programming environments such as MPI and Global Arrays. Built upon the parallel programming environment, is a general framework for solving numerical problems in as much as six dimensions. The highest levels combines the parallel programming and the numerical environment to design applications for chemistry and other types of scientific simulations.

Adaptive refinement in a multi-wavelet basis is the central technique of the numerical environment in MADNESS. The numerical domain $[0,1]$ is repeatedly subdivided by factors of two such that at the n th-level of refinement there exist 2^n boxes each of size 2^{-n} , and the orthonormal basis in each box is the first k Legendre polynomials (termed scaling functions) appropriately scaled and shifted

$$\phi_i(x) = \begin{cases} \sqrt{2i+1}P_i(2x-1), & x \in [0, 1] \\ 0, & \text{otherwise} \end{cases}$$

with the i^{th} function in box l being $\phi_{il}^n(x) = 2^{\frac{n}{2}}\phi_i(2^n x - l)$. Adaptive refinement occurs locally only if the local error is above a truncation threshold (δ).

Wavelets arise as the natural basis to describe the difference in the basis between successive levels of refinement. I.e., the multi-wavelet subspace W_n is complementary to the scaling function space V_n , with $W_n = V_{n+1} - V_n$. The scaling functions and multi-wavelets are related through two-scale relations that in turn make possible controlled adaptive refinement.

A user-defined function $f(x)$ is projected into the basis using orthonormal projection and can be represented in real space as a sum over adaptively refined scaling functions (or, equivalently, values at the Gauss-Legendre quadrature points), or in wavelet space as a sum over scaling functions at the coarsest level and wavelets at finer length-scales.

$$\begin{aligned}
 f^n(x) &= \sum_{l=0}^{2^n} \sum_{i=0}^{k-1} s_{il}^n \phi_{il}^n(x) \\
 &= \sum_{i=0}^{k-1} s_{i0}^0 \phi_{i0}^0(x) + \sum_{m=0}^{n-1} \sum_{l=0}^{2^{m-1}-1} \sum_{i=0}^{k-1} d_{il}^m \psi_{il}^m(x)
 \end{aligned}
 \tag{2.23}$$

The coefficients s_{il}^n and d_{il}^m are respectively referred to as the scaling-function (or sum) and wavelet (or difference) coefficients. Truncation of negligible coefficients enables adaptive refinement and is done in the present application according to the local condition

$$\|d_l^n\|_2 \leq 2^{\frac{-n}{2}} \delta
 \tag{2.24}$$

For the present work, an enabling feature of MADNESS is the efficient and accurate application of many integral convolution operators

$$(T * f)(x) = \int dy K(x-y) f(y)
 \tag{2.25}$$

using the non-standard form [71] and efficient separated representations [72].

Chapter 3

Polarizable Continuum

Electrostatic Solvation Models

Using the dielectric constant to describe the solvent as a polarizable continuum, a description of two solvation models is made. The two models are surface-volume polarizable electrostatics (SVPE), and iso-density solvation models. In both models, a good description of the molecular cavity is essential: the SVPE model builds the molecular cavity as a system of interlocking spheres while the iso-density model uses the molecular electronic charge density to construct iso-density contours. In the paragraphs that follow, the SVPE and the iso-density solvation models will be presented. New results include formulation of both models in a form appropriate for implementation in MADNESS, a new mesh function with much improved numerical behavior, refined approach to computing the molecular surface area and volume.

3.1 Molecular Volume and Surface

To illustrate the use of interlocking spheres in the design of molecular cavities, a geometric approach is used to construct the volume and surface of hard spheres. We limit the volume and surface to that of two spheres; the values obtained thereafter,

are the exact values of the volume, V_e , and the surface S_e . Two intersecting spheres, of radius r_1 and r_2 with a distance d between their two centers, has an overlap region, O_e . Knowing the volume and surface area of the overlap region, the total volume and surface area of the intersecting spheres are computed analytically with the following equations:

$$O_e = \frac{\pi (r_1 + r_2 - d)^2 (d^2 + 2dr_2 - 3r_2^2 + 2dr_1 + 6r_1r_2 - 3r_1^2)}{12d} \quad (3.1)$$

$$V_e = \frac{4\pi}{3} (r_1^3 + r_2^3) - O_e \quad (3.2)$$

$$S_e = \frac{\pi (2dr_1^2 + 2dr_2^2 + r_1^3 + r_1d^2 - r_1r_2^2 + r_2d^2 - r_1^2r_2 + r_2^3)}{d} \quad (3.3)$$

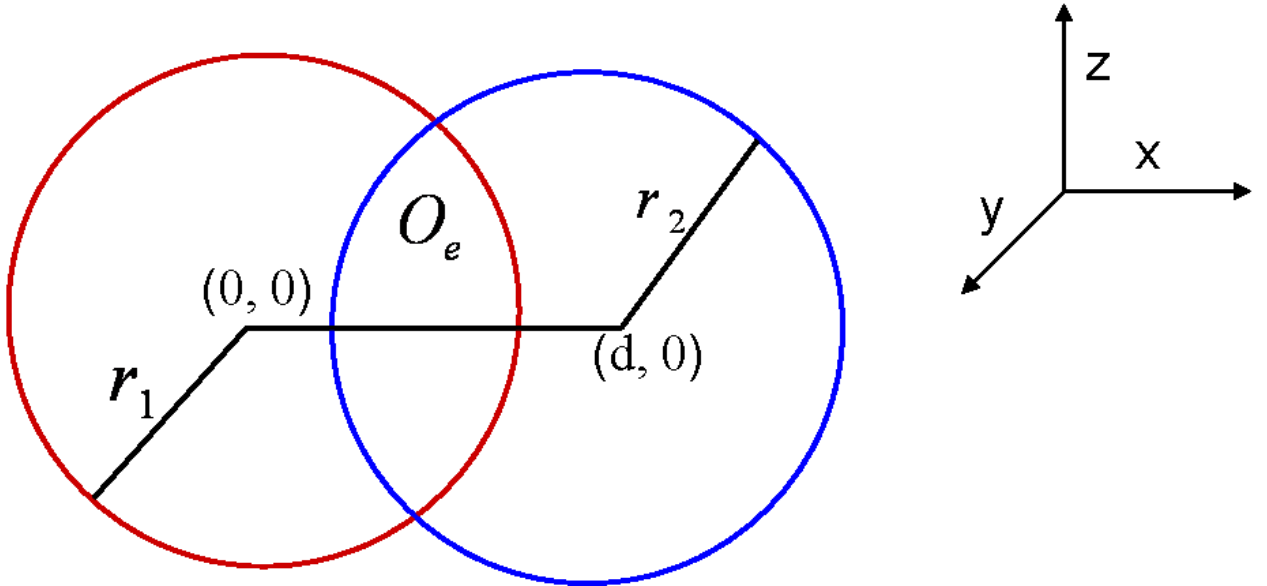


Figure 3.1: Two interlocking spheres

The analytical expression for two intersecting spheres is complicated. If one were to extend this analytical approach into computing the volume and surface area of N -intersecting spheres, then it will be very cumbersome. This increase in complexity, is enough for us to consider a simple and easy to implement approach consisting of constructing a geometric-domain mask as allowed by the effective radii of the intersecting spheres involved.

3.1.1 Computed Volume and Surface

We designed an efficient way of numerically computing the surface and volume of a molecule made up of N atoms; each atom defined by a three dimensional coordinate position r_i and a radius, R_i . The construction of the surface begins with the definition of a regular spherical domain C centered around the three dimensional coordinate of the center of the sphere and extended within the range of its radius. Each atom within the molecule has an effective radius R_i , solvent size is included in the radius of the atom, such that for each atom i with coordinate r_i , the signed normal distance function of an arbitrary point r from the surface of atom is constructed as follows:

$$s(r, i) = |r - r_i| - R_i \quad (3.4)$$

The characteristic function for the sphere surrounding the i th atom is obtained.

$$C(r, i) = 1 - \Theta(s(r, i)) = \Theta(-s(r, i)) \quad (3.5)$$

Θ is the Heaviside step function: its value is zero inside the atom, a half on the surface of the atom, and one outside the atom.

$$\Theta(s(r, i)) = \begin{cases} 0, & \text{if } s < 0 \\ \frac{1}{2}, & \text{if } s = 0 \\ 1, & \text{if } s > 0 \end{cases} \quad (3.6)$$

There are many smooth analytic approximation to the Heaviside step function which we list a few examples.

$$\Theta(s) = \begin{cases} \lim_{\sigma \rightarrow 0} \left[\frac{1}{2} + \frac{1}{\pi} \arctan \left(\frac{s}{\sigma} \right) \right] \\ \lim_{\sigma \rightarrow 0} \frac{1}{2} \left(1 + \operatorname{erf} \left(\frac{s}{\sigma} \right) \right) \\ \lim_{\sigma \rightarrow 0} \frac{1}{2} \left(1 + \tanh \left(\frac{s}{\sigma} \right) \right) \end{cases} \quad (3.7)$$

Hence, the characteristic function for the entire molecule is

$$C(r) = 1 - \prod_{i=1}^N (1 - C(r, i)) = 1 - \prod_{i=1}^N \Theta(s(r, i)) \quad (3.8)$$

Integrating this function will yield the molecular volume. The iso-surface with value one half defines the molecular surface and integrating that will yield the molecular surface area. A more convenient way to define the molecular surface is to note that the derivative of the characteristic function normal to the surface is a delta function positioned at the surface. This is discussed in more detail in section [3.1.2](#)

3.1.2 Molecular Volume and Surface from Soft Spheres

Instead of using the step function we introduce a function that smoothly switches between 0 and 1 over a controllable distance σ

$$\frac{1}{2} \left(1 + \operatorname{erf} \left(\frac{s}{\sigma} \right) \right) \quad (3.9)$$

The second of the three expressions in [3.7](#) is modified to form the smooth Heaviside-like step function which will be used as a switch between the inside and the outside of the atom thereby enabling a better handling of the boundary conditions (discontinuity). The expression as well as its derivative are easier to handle numerically than the other Heaviside-like expressions. As the value of σ becomes smaller we approach the description of a step function as shown in [Fig. 3.2](#). We

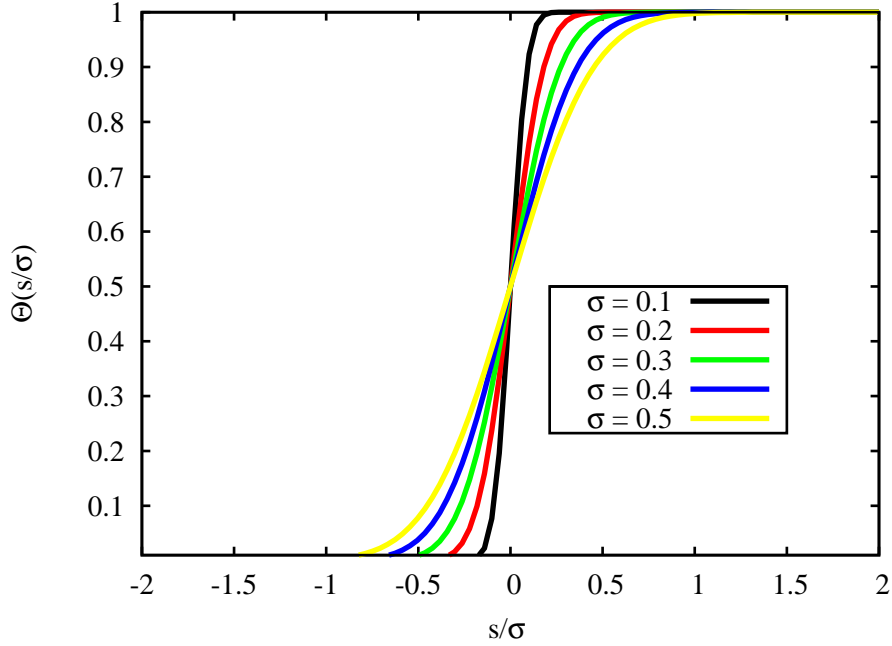


Figure 3.2: The plots illustrates how $\Theta(\frac{s}{\sigma}) = \frac{1}{2} \left(1 + \text{erf} \left(\frac{s}{\sigma} \right) \right)$ gets closer to a step function as $\sigma \rightarrow 0$

now have soft spheres that are much easier to compute with, and are actually a lot more like real atoms. To define the surface, we define a mathematical expression that behaves like the outward normal to the surface times a delta function at the surface .

$$\mathbf{n}(\mathbf{r}) = -\nabla C(\mathbf{r}) \quad (3.10)$$

The gradient is automatically oriented normal to the surface and the negative sign makes it point outward. The surface itself is a spherical shell defined by

$$S(r) = |\mathbf{n}(\mathbf{r})| \quad (3.11)$$

For a single atom, we obtain the gradient as follows:

$$\begin{aligned}
\nabla C(r, i) &= -\frac{\partial}{\partial s(r, i)} \Theta(s(r, i), \sigma) \nabla s(r, i) \\
\nabla s(r, i) &= \frac{r - r_i}{|r - r_i|} \\
|\nabla s(r, i)| &= 1 \\
\frac{\partial}{\partial s} \Theta(s, \sigma) &= \frac{1}{\sigma\sqrt{\pi}} \exp\left(-\frac{s^2}{\sigma^2}\right) \\
|n(r)| &= \frac{1}{\sigma\sqrt{\pi}} \exp\left(-\frac{s^2}{\sigma^2}\right)
\end{aligned} \tag{3.12}$$

For molecules, many atoms intersect and we have to compute the different components of the derivatives. The denominator of the derivative (i.e $(1 - C(r))$) needs to be handle with care especially for very small values

$$\nabla C(r) = \left(\prod_{i=1}^N (1 - C(r, i)) \right) \left(\sum_{i=1}^N \frac{\nabla C(r, i)}{1 - C(r, i)} \right) \tag{3.13}$$

3.2 The Iso-density Cavity

Contrary to the cavity of the interlocking sphere described above, the dielectric function is a functional of the electronic density of the molecular system $\epsilon[\rho(r)]$. Just as in the interlocking sphere model where the switching function is used to switch smoothly between the inside and outside of the molecular cavity, a similar parameter exist here to allow for a smooth decay of the dielectric function in the proximity of the solute-solvent boundary. In the implementation, the dielectric function is described using two parameters ρ_0 and β :

$$\epsilon[\rho(r)] = 1 + \frac{\epsilon - 1}{2} \left(1 + \frac{1 - (\rho(r)/\rho_0)^{2\beta}}{1 + (\rho(r)/\rho_0)^{2\beta}} \right) \tag{3.14}$$

The parameter ρ_0 is the density threshold determining the cavity size and β modulates the smoothness of the transition from ϵ to one. Eq. 3.14 asymptotically approaches the value of the dielectric constant ϵ (the permittivity of the bulk solvent) in the tailing region of the electronic charge density. It reaches a maximum value of one in regions

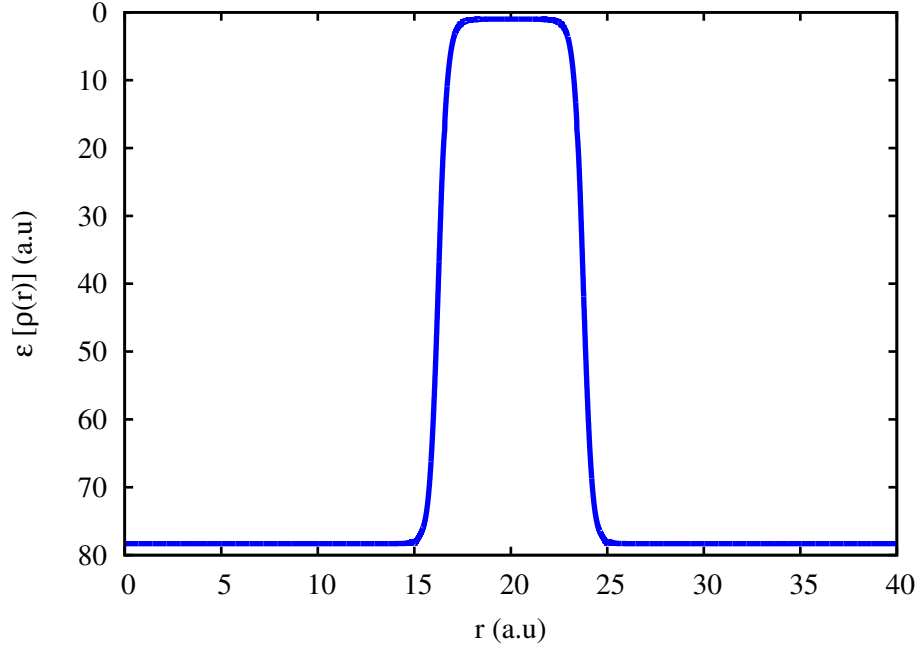


Figure 3.3: Two dimensional plot of the dielectric function $\epsilon[\rho(r)]$ along the x-component of the simulation cube

where the electronic density is high. This functional is accurately computed and represented without having to augment the electronic density with some Gaussian function as is the case in [97]. The nature of the functional suggest numerical difficulties in its computation, which we overcome by setting a cutoff value of 10^{-12} of the electronic charge density such that any value of the functional, at given point, that is less than the cutoff-value is systematically set to zero. The programming environment contributes to the handling of the roundoff errors, by computing the functional point-wise, contrary to a step-by-step method which is suggested on a first view by the functional.

3.3 Solving The Poisson's Equation

Two cavity models, to mark the solute-solvent interface, have been presented above. The cavities will be used to find solutions to the Poisson's equation. The reference solution is the vacuo potential which is obtained as a solution to the Poisson's equation in the vacuum.

$$\nabla^2\phi = -4\pi\rho \tag{3.15}$$

What follows from here is a description of how to solve the Poisson's equation for a system in a solvent described implicitly by its dielectric property.

3.3.1 Interlocking Spheres

We have developed a function (the molecular mask) that enables us to represent an irregular domain such as a molecular cavity that we will employ to solve the Poisson's equation for an electronic distribution of charge in a solvent. The solvent is represented implicitly as a dielectric continuum with its dielectric constant ϵ . There exist two media separated by the boundary of the irregular domain namely, the inside of the domain which is a vacuum with a unitary dielectric constant and the outside of the domain which is the solvent. Defining Ω as our irregular domain, we associate the dielectric constants to the molecular mask $C(r)$ such that we can switch between the inside and outside of Ω . Thus, for this work we define our position dependent dielectric function as follows:

$$\epsilon(r) = \epsilon_0 C(r) + \epsilon(1 - C(r)) \tag{3.16}$$

The Heaviside-like function of Eq. 3.9 enables the switching between the inside and the outside of the domain. The value of $C(r)$ determines whether we are in the

presence of a solvent or a vacuum.

$$C(r) = \begin{cases} 1 & \text{inside } \Omega \\ 0 & \text{outside } \Omega \end{cases} \quad (3.17)$$

ϵ_0 and ϵ are the dielectric constants of the vacuum ($\epsilon_0 = 1.0$) and the solvent respectively. We now set up the Poisson's equation for an electronic distribution of charge within a dielectric medium.

$$\nabla \cdot (\epsilon(r) \nabla U(r)) = -4\pi\rho(r) \quad (3.18)$$

Finally, we obtain an expression that projects the surface induced charge and the electrostatic potential inside and outside the molecular volume.

$$\nabla^2 U(r) = -\frac{4\pi\rho(r)}{\epsilon(r)} - \frac{\nabla\epsilon(r) \cdot \nabla U(r)}{\epsilon(r)} \quad (3.19)$$

The reference potential as earlier defined is the in-vacuo potential, the potential in the absence of the solvent. We can extract (from Eq. 3.19) the effective volume charge distribution ρ_{eff} and the surface charge distribution σ .

$$\rho_{eff} = \frac{1}{\epsilon}\rho \quad (3.20)$$

$$\sigma = \frac{1}{4\pi\epsilon} \nabla\epsilon \cdot \nabla U$$

We proceed to solving Eq. 3.19 by inverting the Laplacian through the convolution of the volume and the surface distribution of charges with the free-space Green function.

$$G(r, r') = \frac{1}{|r - r'|} \quad (3.21)$$

The electrostatic potential in vacuo U_v and the total electrostatic potential U_t are computed from Eq. 3.22, and Eq. 3.23.

$$U_t = G \cdot (\rho_{eff} + \sigma) \quad (3.22)$$

$$U_v = G \cdot \rho \quad (3.23)$$

Setting $\epsilon_0 = 1.0$ we can compute the reaction potential, the electrostatic effects of the solvent on a molecule dissolved in it, by subtracting the vacuo potential from the total potential.

$$\begin{aligned} U_r &= U_t - U_v \\ U_r &= G \cdot (\sigma + \rho_{eff} - \rho) \\ U_r &= G \cdot \left(\sigma - \frac{(\epsilon-1)}{\epsilon} \rho \right) \end{aligned} \quad (3.24)$$

If the charge distribution is localized entirely within the cavity, then the reaction potential is due to the surface-induced charge distribution. This is not always the case for the electronic charge distribution. Only the nuclear charge distribution is entirely localized within the molecular cavity.

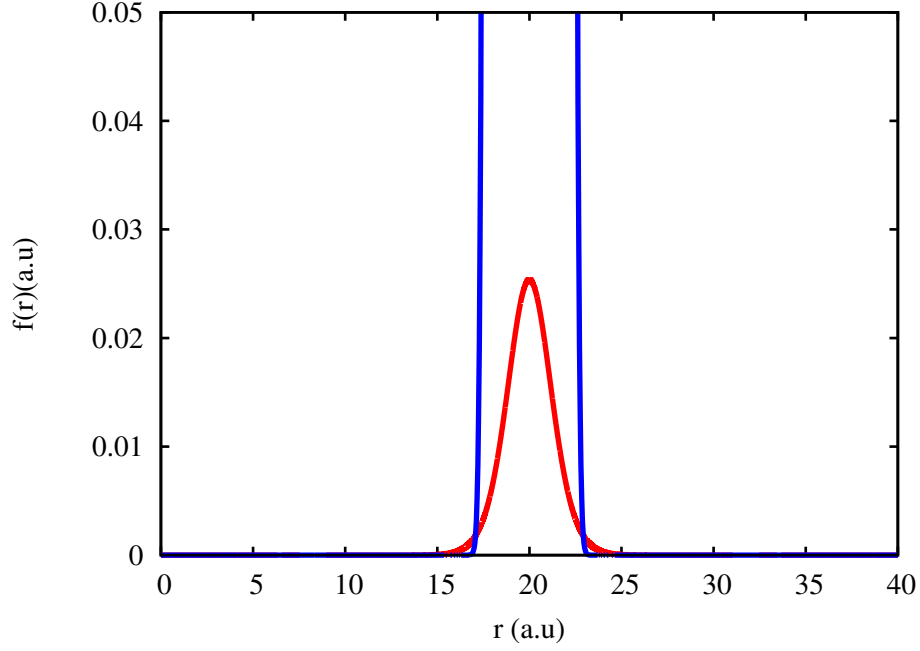


Figure 3.4: Two dimensional plot of the electronic charge distribution (in red) and the interlocking spheres cavity function (in blue) of the benzene molecule. The plot is along the x-component of the electronic charge distribution. A fraction of the electronic charge density is outside the molecular cavity.

The total electrostatic potential could equally be computed directly from the surface charge distribution, which we obtain by applying the operator \hat{S} on Eq. 3.22.

$$\hat{S} = \frac{1}{4\pi\epsilon(r)} \nabla\epsilon(r) \cdot \nabla \quad (3.25)$$

The operations then follows:

$$\begin{aligned} \hat{S}U_t &= \sigma \\ \sigma &= \sigma_0 + \overline{G} \cdot \sigma \\ \sigma_0 &= \overline{G} \cdot \rho_{eff} \\ \overline{G} &= \frac{1}{4\pi\epsilon(r)} \nabla\epsilon(r) \cdot \nabla G \end{aligned} \quad (3.26)$$

For a perfect conductor, the exterior potential is zero, the molecule in the cavity is completely screened such that it only “sees” the field inside the cavity. The switching function cannot be used to represent the screening exactly. A new dielectric function expression is derived using the log-derivative as shown in the equations below.

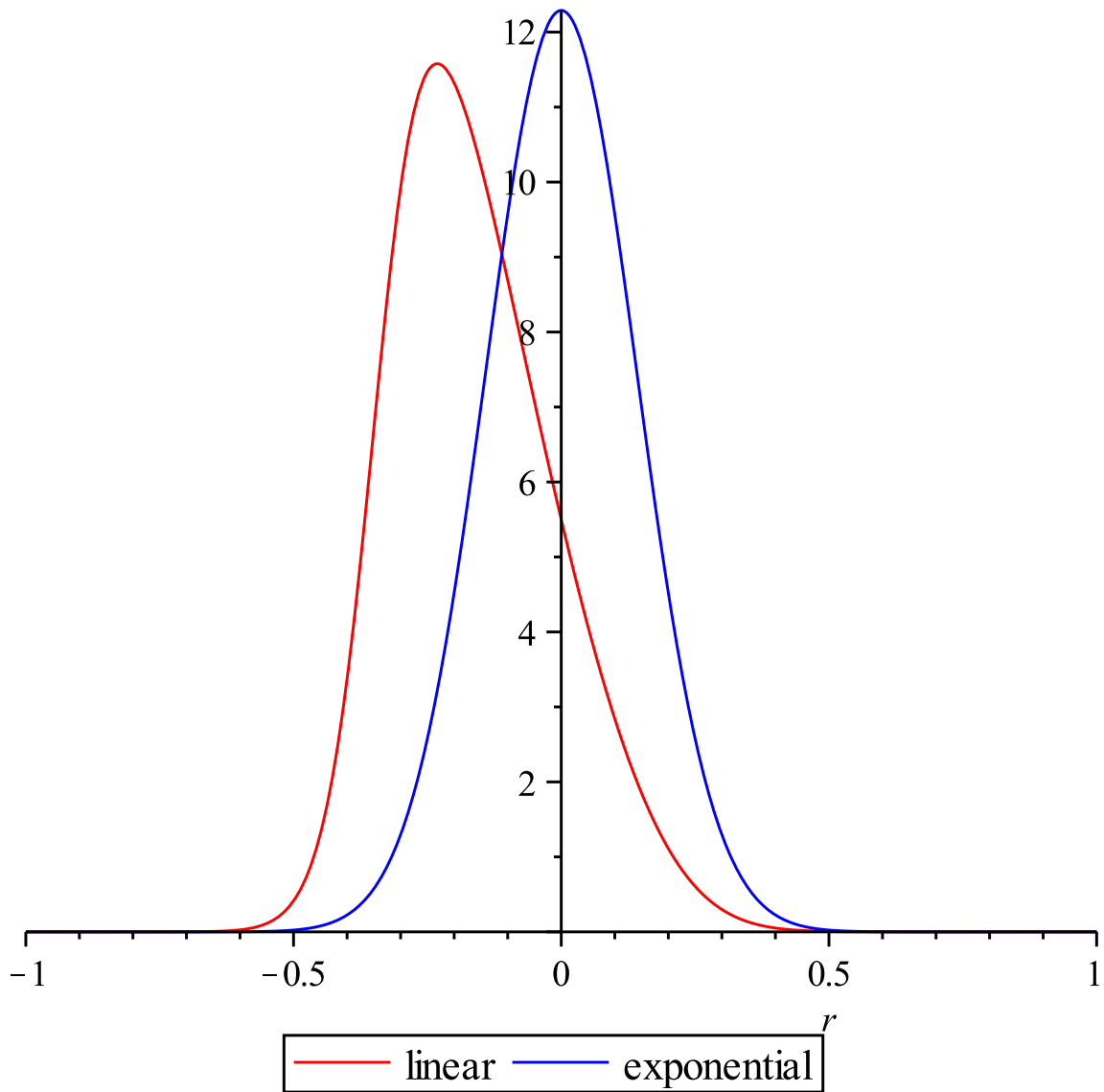


Figure 3.5: Comparison of the norm of the log-derivative of the dielectric function for the two forms of the switching function (linear (3.16) and exponential (4.39)) for $\sigma = 0.2$ and $\epsilon_\infty = 78$.

$$\begin{aligned}
\epsilon(r) &= \epsilon_0 \exp\left(\log \frac{\epsilon_1}{\epsilon_0}(1 - C(r))\right) \\
\epsilon(r)^{-1} &= \epsilon_0^{-1} \exp\left(\log \frac{\epsilon_0}{\epsilon_1}(1 - C(r))\right) \\
\nabla \log \epsilon(r) &= \frac{\nabla \epsilon(r)}{\epsilon(r)} = \log \frac{\epsilon_0}{\epsilon_1} \nabla C(r)
\end{aligned}
\tag{3.27}$$

With this form of discontinuous dielectric function, the charge distribution is always localized exactly on the surface of the molecular cavity, and this leads to a much improved numerical behavior and more rapid convergence to the limit $\sigma = 0$ and σ is reduced.

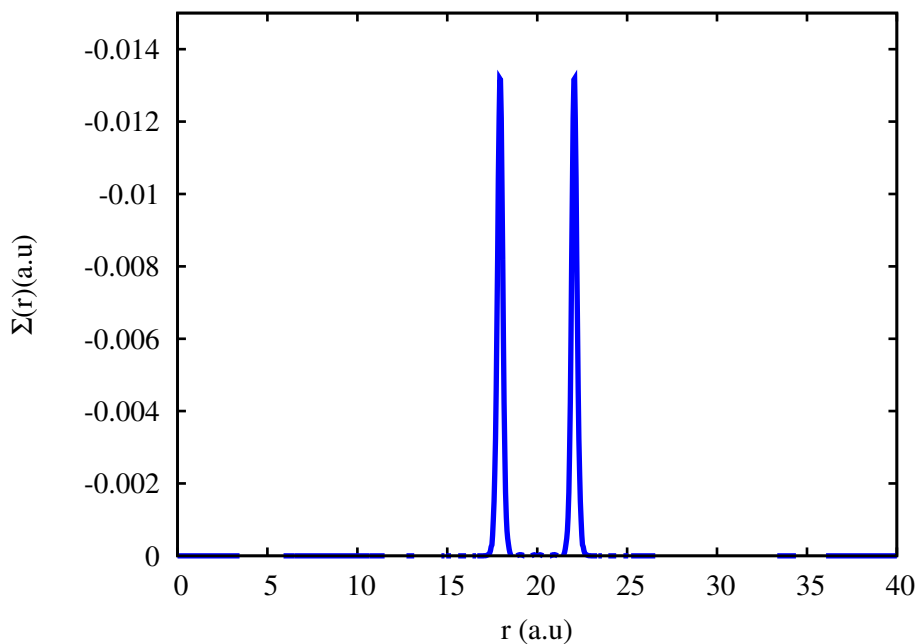


Figure 3.6: Two dimensional plot of the surface charge distribution $\Sigma(r)$ on the interlocking spheres cavity for the benzene molecule. The charge distribution is zero everywhere except on the molecular cavity surface. The plot is along the x-component of the electronic charge distribution

3.3.2 Iso-density Cavity

The solution to the Poisson's equation described in this section is very similar to that of the interlocking sphere cavity but for the fact that the dielectric function is a functional of the electronic charge density:

$$\nabla \cdot (\epsilon[\rho(r)] \nabla \phi(r)) = -4\pi\rho(r) \quad (3.28)$$

Eq. 3.28 is expanded and simplified as was the case in Eq. 3.18:

$$\nabla^2 \phi(r) = -4\pi\rho/\epsilon[\rho(r)] - \frac{\nabla\epsilon[\rho(r)]}{\epsilon[\rho(r)]} \nabla\phi(r) \quad (3.29)$$

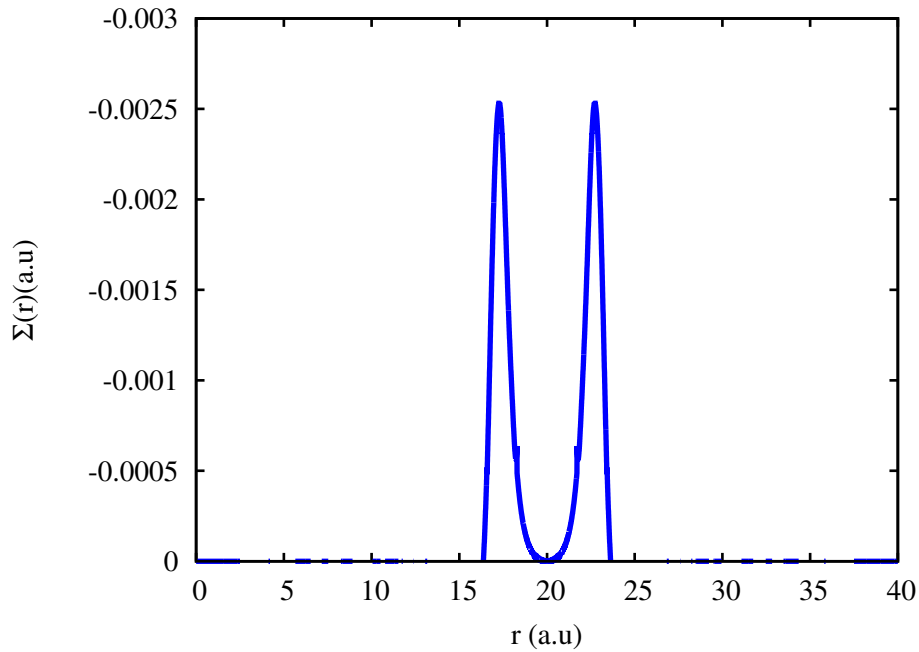


Figure 3.7: Two dimensional plot of the surface charge distribution $\Sigma(r)$ of the benzene molecule for the iso-density method. The surface charge distribution is an outcome of polarization and is represented by the second term on the RHS of Eq. 3.29. The plot is along the x-component of the electronic charge density.

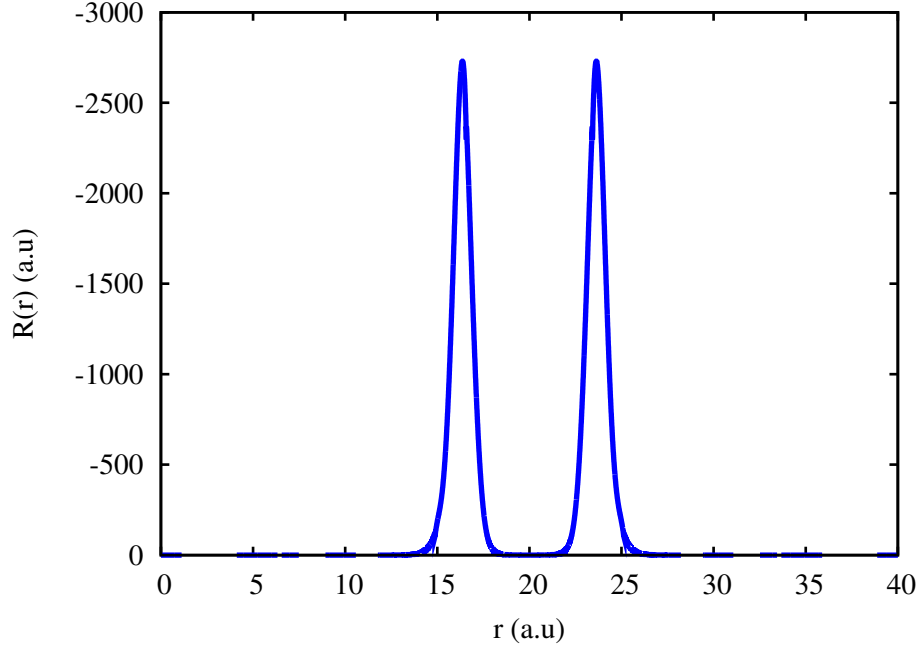


Figure 3.8: Two dimensional plot of the quotient of the functional derivative of $\epsilon[\rho(r)]$ with respect to ρ by $\epsilon[\rho(r)]$. Computation is carried out point-wise to control numerical noise.

The right hand side (RHS) of Eq. 3.29 is computed point-wise before convolution with the free-space Green's function. The second term is computed with care, by setting a cutoff value (10^{-12}) to the electronic charge density (values of $\rho(r)$ less than the cutoff-value is set to 0). The chain rule is applied on $\nabla\epsilon[\rho(r)]$ and the partial derivative of $\epsilon[\rho(r)]$ with respect to ρ is combined and simplified before multiplying with $\nabla\phi$ and $\nabla\rho$. The programming environment favors the computation of the second term, point-wise, so as to avoid errors from machine roundoff.

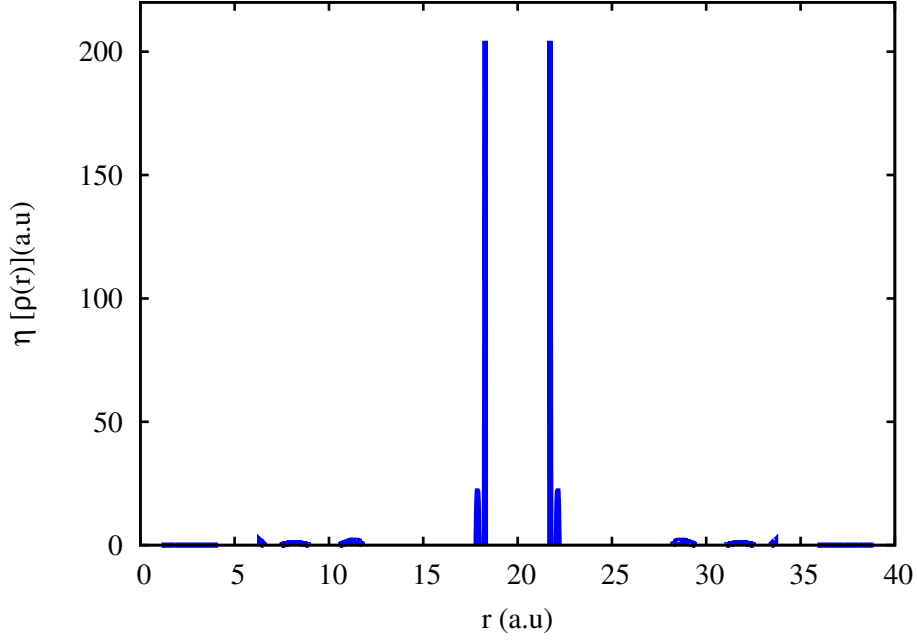


Figure 3.9: Two dimensional plot of the functional derivative of $\epsilon[\rho(r)]$ with respect to ρ . The use of cutoff value on electronic density is not enough to eliminate numerical noise.

$$\begin{aligned}\nabla\epsilon[\rho(r)] &= \left(\frac{\partial\epsilon[\rho(r)]}{\partial\rho}\right)_r \nabla\rho \\ \frac{\partial\epsilon}{\partial\rho}(r) &= \frac{1-\epsilon}{\rho_0} \frac{2\beta(\rho(r)/\rho_0)^{2\beta-1}}{(1+(\rho(r)/\rho_0)^{2\beta})^2}\end{aligned}\tag{3.30}$$

putting together Eq. 3.14 and 3.30, we obtain the following

$$\frac{\nabla\epsilon[\rho(r)]}{\epsilon[\rho(r)]} = \frac{2\beta(1-\epsilon)}{\rho_0} \frac{(\rho(r)/\rho_0)^{2\beta-1}}{(1+(\rho(r)/\rho_0)^{2\beta})(\epsilon+(\rho(r)/\rho_0)^{2\beta})} \cdot \nabla\rho(r)\tag{3.31}$$

3.3.3 Electrostatic Potential

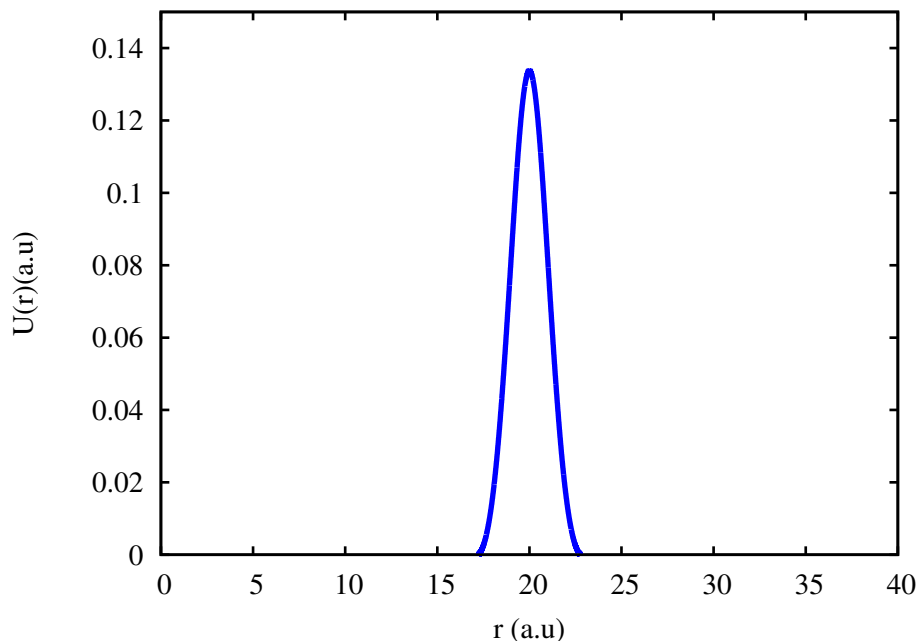


Figure 3.10: Two dimensional plot of the total electrostatic potential of the benzene molecule for the iso-density method. The plot is done along the z-axis

Eq. 3.19 and Eq. 3.29 are all linear second order Poisson's equation and the electrostatic potential for which we solve, appears on both sides of the equation, thus we solve these equations self-consistently. First, we invert the second order differential operator through convolution with the free space Greens function that is already implemented in MADNESS. The self-consistent routine for solving the linear and nonlinear equations implemented in MADNESS is the Krylov subspace accelerated inexact Newton method (KAIN) [54]. The interface to the KAIN routine consist of the vacuo and the initial guess potentials. The vacuo and the initial potentials are used to compute the residuals with which the KAIN routine is started. The total electrostatic potential for a solute in a solvent is obtained when the convergence criteria are met (convergence occurs when the 2-norm of the residuals is less than $10.0 * tol$ where $tol = \max(10^{-4}, threshold)$ threshold is the accuracy on the MADNESS function)

3.4 Solute-solvent Reaction

The reference potential is the gas phase potential which is obtained by convolving the total charge density ρ_{tot} , electronic and nuclear charge densities, with the free-space Green’s function. The electronic $\rho(r)$ and nuclear $\gamma^N(r)$ charge densities are computed separately. The electronic charge density is computed from an initial guess of atomic orbital vectors, c_μ (obtain from NWchem [102]). The initial guess of the electronic charge density is made in a small Gaussian basis and converted into a MADNESS function. The delta function $\delta(R_i - r)$ of the nuclear charge density is made of very small (by width) Gaussian functions computed with very fine mesh. The order (k) of the numerical basis is chosen such that the nuclei coordinates coincide with dyadic points (i.e., an integer multiple of some power of two division of the domain) – this will give the most accurate representation.

$$\begin{aligned}\gamma(r) &= \gamma^N(r) + \rho(r) \\ \gamma^N(r) &= \sum_{i=1}^N Z_i \delta(R_i - r) \\ \rho(r) &= \sum_i \sum_{\mu}^{occ \ AO} \chi_\mu c_{\mu i}\end{aligned}\tag{3.32}$$

The solute-solvent reaction for both the interlocking sphere and the iso-density models are very similar in principle and only differ in the steps taken to compute them. The steps taken to compute the solute-solvent reaction potential and energy for the interlocking spheres and iso-density approaches are described in the following two paragraphs.

3.4.1 The Solute-solvent Reaction Potential

The solute-solvent reaction potential energy E_{rp} is the product of the total charge distribution and the solute-solvent reaction potential which we can expand explicitly to show the different components. The solute-solvent reaction potential is decomposed

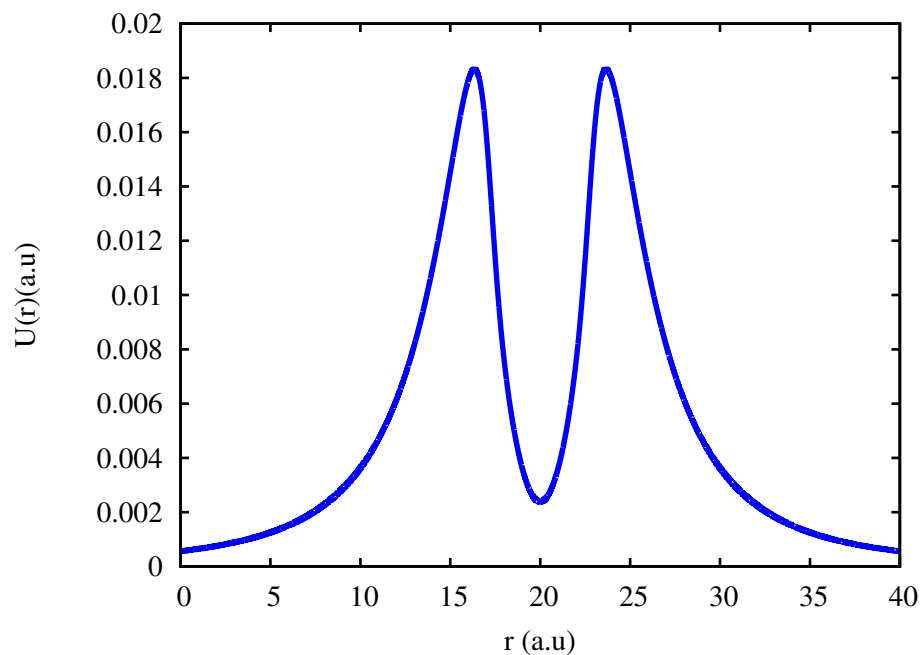


Figure 3.11: Two dimensional plot of the solute-solvent electrostatic reaction potential of the benzene molecule for the iso-density method. The plot is along the x-axis of the simulation cube.

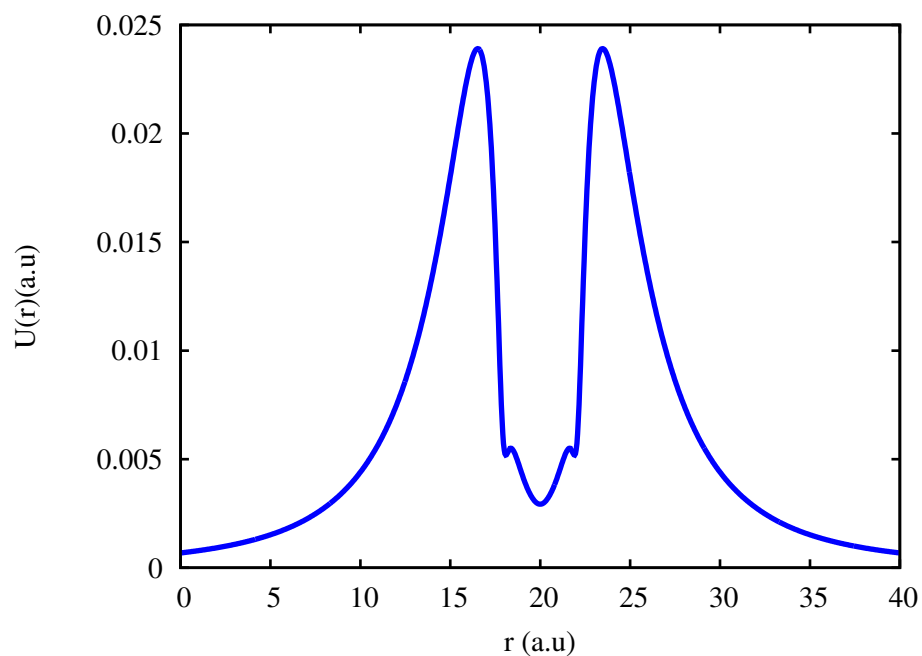


Figure 3.12: Two dimensional plot of the solute-solvent electrostatic reaction potential of the benzene molecule for the SVPE method. The plot is along the x-axis of the simulation cube.

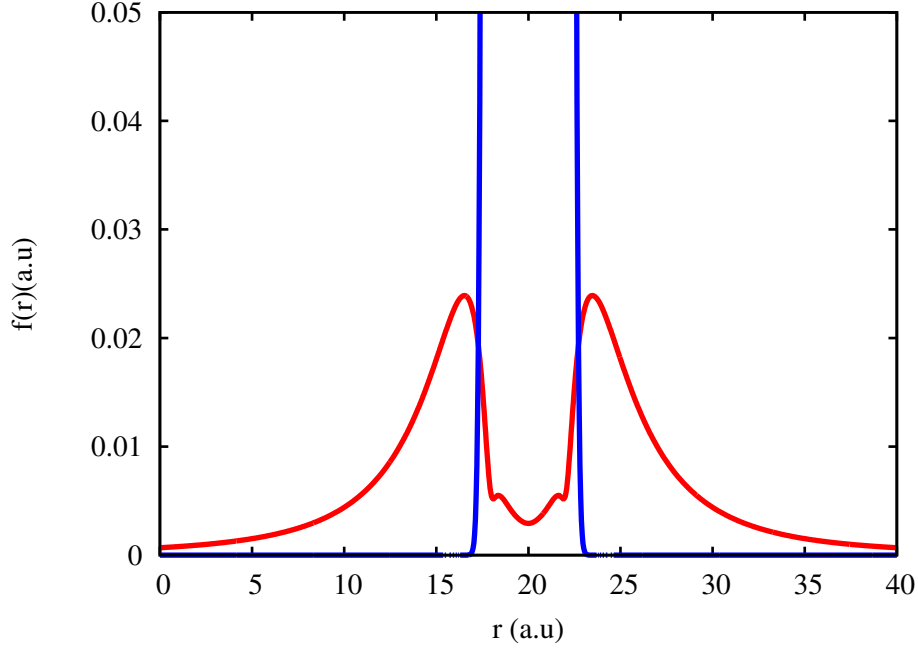


Figure 3.13: Two dimensional plot of the solute-solvent electrostatic reaction potential (in red) and the interlocking sphere cavity function of the benzene molecule (in blue).The surface and volume electrostatic potentials are accounted for and are indistinguishable. The plot is along the x-component of the simulation reference.

into the nuclear U_{rn} and electronic U_{re} components with each of the components being the convolution of the free-space Green's function with the nuclear and electronic charge distributions respectively.

$$\begin{aligned}
 U_r(r) &= U_{rn}(r) + U_{re}(r) \\
 U_{rn}(r) &= G \cdot \gamma^N(r) \\
 U_{re}(r) &= G \cdot \rho(r)
 \end{aligned}
 \tag{3.33}$$

The solute-solvent reaction potential energy then follows as:

$$\begin{aligned}
 E_{rp} &= (\rho(r) + \gamma^N(r)) (U_{rn}(r) + U_{re}(r)) \\
 E_{rp} &= \rho(r)U_{rn}(r) + \rho(r)U_{re} + \gamma^N(r)U_{rn} + \gamma^N(r)U_{re}
 \end{aligned}
 \tag{3.34}$$

The electrostatic solute-solvent reaction potential explicitly fragmented into four terms, namely the electron-nuclear E_{en} , the electron-electron E_{ee} , the nuclear-nuclear E_{nn} and the nuclear-electron E_{ne} electrostatic reaction potential energies. The E_{en} and E_{ne} terms should be equal in magnitude.

$$E_{rp} = E_{en} + E_{ee} + E_{nn} + E_{ne} \quad (3.35)$$

Though the iso-density cavity computation is as proposed by Fattbert and Gygi [97], the solute-solvent potential is the solution of Eq. 3.29 with a fixed cavity. This is similar to the interlocking sphere approach but for the fact that the iso-density cavity is a functional of the density and requires the inclusion of the response of the electronic charge density to the change in cavity. The electrostatic solute-solvent reaction energy E_{es} is computed from the total charge density and the solute-solvent reaction potential $U_r(r)$.

$$\int \rho_{tot}(r)U_r(r)dr \quad (3.36)$$

E_{es} is an augmentation to the Kohn-Sham energy functional for a system of ions and electrons

$$E[\rho] = T[\rho] + \int v(r)\rho(r)dr + E_{xc} + \frac{1}{2} \int \rho(r)\phi[\rho]dr + \frac{1}{2} \int \rho_{tot}(r)U[\rho]dr \quad (3.37)$$

The terms on the right hand side of Eq. 3.37 correspond to the kinetic energy of the electron, the interaction energy of the electrons and the ions, the exchange-correlation energy, the electrostatic energy and the solute-solvent reaction energy. Inserting ρ_{tot} from Eq. 3.29, with fixed cavity, and integrating by parts, the solute-solvent reaction energy is rewritten as follows:

$$E_r = \frac{1}{4\pi} \int \epsilon[\rho] (\nabla U[\rho])^2 dr \quad (3.38)$$

The functional derivative of Eq. 3.38 with respect to ρ yields U_r and an extra term, U_ϵ originating from the fact that the dielectric function is a functional of the electronic charge density.

$$\frac{\partial E_r}{\partial \rho}(r) = U_r + U_\epsilon \quad (3.39)$$

$$U_\epsilon = -\frac{1}{4\pi} (\nabla U(r))^2 \frac{\partial \epsilon}{\partial \rho}(r) \quad (3.40)$$

The self-consistent Kohn-Sham potential is constructed summing U_ϵ and the vacuum corrected solute-solvent reaction potential U_r to which contributions from local and nonlocal potentials are added. The U_ϵ term is very unstable, due mainly to the $(\nabla U(r))^2$ term which is very small everywhere except on the surface where the value of the function is not zero but yet just slightly bigger than the threshold. High precision is needed to compute this function. The unstable term can be forgone if the iso-density cavity is kept fixed by using a converged gas phase electronic charge density to compute the dielectric functional. In this case, the iso-density is kept fixed and U_ϵ cease to be important. J. Dziedzic *et al* [55] have shown that this modification greatly improves the methodology and makes the method very efficient.

3.4.2 Electrostatic Free Energy of Solvation

Self-consistent solution of the Kohn-Sham equations for the Hamiltonian of an isolated solute provides the gas phase internal energy E_g as well as the electronic charge density to be added to the nuclear charge, to obtain the total charge distribution used in solving the Poisson equation. The effective Kohn-Sham Hamiltonian is constructed by adding the solute-solvent reaction potential to the isolated solute Hamiltonian. The new Kohn-Sham equations are then solved and a new solute charge density that differs from the gas phase counterpart is obtained. Since the charge density changes, the final solute internal energy E_s changes as well. The solute-solvent reaction energy is defined as follows:

$$E_r = \int d^3r' \rho_{tot}(r') U_r(r') \quad (3.41)$$

Using the Ben-Naim convention [98] that the solute maintains a fixed position as it transferred from gas to solvent. The electrostatic free energy of solvation is then defined by

$$\Delta G = E_s - E_g + \frac{1}{2}E_r \quad (3.42)$$

Note that only half of the solute-solvent reaction energy is available as free energy, the remaining half is used as work to reversibly charge the solute in the presence of the solvent.

3.4.3 Cavitation Energy

Cavitation energy ΔG represents the effect of the solute-solvent interaction on the solvent, in fact, cavitation energy is defined as the work done on the solvent to create an appropriate cavity inside the solvent for the solute in the absence of the solute-solvent interaction [73]. As of now, there are no experimental data for the cavitation energy and different approaches have been introduced for its calculation. The scaled particle theory [74, 75], originally proposed by Pierotti and further developed in different studies [76, 77, 78, 79, 80] wherein parameterization is still needed to represent the radius of the solvent and those of the spheres centered on the solute atom, although the approaches rely on a rigorous application of statistical mechanics. The Pierotti-Clavierie formulation [81] is the most used approximations for non-spherical cavities. For a system of N interlocking spheres centered on the atoms, the cavitation free energy is computed as follows:

$$\Delta G_{cav} = \sum_{k=1}^N \frac{A_k}{4\pi R_k^2} G_{cav}(R_k) \quad (3.43)$$

where A_k is the area of atom k in contact with the solvent, R_k is the Van der Waals radius, and $G_{cav}(R_k)$ is the cavitation free energy associated with the creation of a spherical cavity of radius R_k around the k th atom.

The macroscopic surface tension of the solvent Γ , as suggested by Uhlig [82, 83, 84] is used to describe the ΔG_{cav} . This consists of expressing the work involved in producing the cavity as the product of Γ by the area of the spherical cavity $\Delta = 4\pi R^2\Gamma$. This approach has been extended to include the curvature of the solute-solvent interface as explained by the Tolman theory for the surface tension of droplet [85] as simplified in the following expression.

$$\Delta G_{cav} = PV + 4\pi R^2\bar{\Gamma} \left(1 - \frac{2\delta}{R}\right) \quad (3.44)$$

$\bar{\Gamma}$ is the effective surface tension for the interface, R is the radius of the cavity, δ is the proportionality coefficient accounting for the interface curvature and σ is the Lennard-Jones radius. Floris *et al.* [87] and Huang *et al.* [86] through their simulations, have assigned to δ a value of 0.0 in TIP4P water, and of the order of -0.5σ for different Lennard-Jones fluid. This suggest that the curvature correction can be ignored for cavities with radii above a few Angstroms. Thus we can, as have done Scherlis *et al.* [97], compute the cavitation as the product of the surface tension by the area of the cavity.

$$\Delta G_{cav} = \Gamma S \quad (3.45)$$

S is the area of either the iso-density or the interlocking spheres cavity described herein. The area of the iso-density cavity is computed using its characteristic function (equation 3.46) together with the idea originally proposed by Cococcioni *et al.* [88]

$$\theta[\rho(r)] = \frac{1}{2} \left[\frac{(\rho(r)/\rho_0)^{2\beta} - 1}{(\rho(r)/\rho_0)^{2\beta} + 1} + 1 \right] \quad (3.46)$$

The volume V_q of the iso-density cavity can now be computed as an integral sum of the characteristic function of the iso-density cavity over space.

$$V_q = \int dr^3 \theta(\rho(r) - \rho_0) \quad (3.47)$$

The area of the iso-density cavity is computed as the 2-norm of the gradient of the characteristic function i.e

$$S_q = |\nabla\theta(\rho(r) - \rho_0)|. \quad (3.48)$$

Eq. 3.48 can be further simplified with the aid of the chain rule for functional derivative, an approach adapted for MADNESS, that is different from the finite-difference approach (that consist of determining the difference between two adjacent iso-surfaces around the iso-density threshold ρ_0). This is simply a finite difference with a central difference over the entire space. The MADNESS approach is summed up in the following equation

$$\begin{aligned} S_q &= \left| \left(\frac{\partial\theta(\rho(r) - \rho_0)}{\partial\rho} \right)_r \cdot \nabla\rho(r) \right| \\ &= \left| 2\beta \frac{(\rho(r) - \rho_0)^{2\beta}}{(1 + (\rho(r) - \rho_0)^{2\beta})^2} \cdot \nabla\rho(r) \right| \end{aligned} \quad (3.49)$$

3.5 Results and Discussion

The SVPE and the iso-density solvation models have been implemented in MADNESS. Molecular systems comprising cations, anions and neutral molecules of different symmetries as well as different charge distributions have been tested. The implementation of the two solvation models were carried out at both Hartree-Fock and DFT/PBE0 levels of theory. We compare our SVPE and the iso-density solvation models to other existing SVPE model. Likewise we compare the iso-density solvation model to experiment and similar models in the literature.

3.5.1 Molecular Surface and Volume Results

Using the SVPE model, we compute the molecular volume and molecular surface of selected molecules and compare them to some well known methods. The molecular geometries are optimized at the RHF/6-31G* level in NWchem. The molecular face

model [89] uses the fact that the potential generated by an electron in a molecule and felt by other electrons and nuclei is equal to the negative of the ionization potential of that electron. A molecular intrinsic characteristic contour, a unique representation of the molecular shape is then defined and the molecular face surface area (MFSA) as well as the molecular face volume (MFV) are computed. The molecular iso-density contour approach[90] to computing the molecular iso-density surface area (MIDSA) and the molecular iso-density volume (MIDV) is also considered. Some hard sphere models with the solvent excluded surface area [91] (SESA), solvent excluded volume (SEV), the Van der Waal surface area [92] (VdWSA),and the Van der Waal volume (VdWV) are equally considered.

Finally, we assess the performance of our method with other methods as well as with experimental results by using Eq. 3.50, The Pearson’s correlation coefficient, to compute the correlation coefficients. The atomic radii used in the SVPE calculations are Van der Waals radii. The molecules in general have Carbon, Oxygen, Nitrogen, Hydrogen, and Chlorine atoms in their composition with atomic radii of 1.70, 1.52, 1.55, 1.20, 1.75 angstrom respectively.

$$R_{XY} = \frac{\sum XY - \frac{(\sum X)(\sum Y)}{n}}{\sqrt{\left(\sum X^2 - \frac{(\sum X)^2}{n_X}\right) \left(\sum Y^2 - \frac{(\sum Y)^2}{n_Y}\right)}} \quad (3.50)$$

R_{XY} is the correlation coefficient, n_X is the number of X-values, n_Y is the number of Y-values, n is the number of pairs of X and Y values, and X and Y are the data for which the correlation coefficients are being computed.

Table 3.1: Molecular surface area of some selected molecules compared to the molecular surface areas computed using hard spheres and iso-density methods. The SVPE surface areas are computed with a surface width of 0.3 and areas are reported in atomic units, squared

Molecules	MFSA	VdWSA	SESA	MIDSA	SVPE
CH_3COCH_3	97.53	90.86	98.29	95.23	70.44
CH_2CH_2	45.89	55.65	62.82	56.43	59.05
C_6H_{12}	128.23	128.2	125.98	129.83	130.86
CH_3CONH_2	86.08	78.78	84.57	81.69	82.25
H_2O	28.08	33.45	32.81	36.68	36.56
R_{XY}	0.922	0.956	0.929	0.947	1.0

The molecular surface areas and volumes computed using the interlocking sphere models (SVPE) generally match the results from other methods. Looking at Table 3.1, the MFSA and the SESA correlate with the SVPE surface areas at 0.922 and 0.929 respectively. This is a significant level of correlation given that these two methods use a parameterization (MFSA) and a locus of points (SESA) completely different from that of the SVPE. On the other hand, the VdWSA and the MIDSA surface areas have better correlation coefficients (0.956 and 0.947) with the SVPE model. The VdWSA is computed analytically with the same Van der Waal radii for the interlocking spheres as with the SVPE model while the MIDSA surface areas are computed from iso-density contours. The observations from Table 3.2 follow those from the surface areas calculation. Globally, the different methods agree with the SVPE volume with the VdWV and MIDV having the same correlation coefficients with the SVPE models (0.960, 0.960) and at the same time better than the level of correlation between, the MFV, the SEV and the SVPE (0.913 and 0.929).

Table 3.2: Molecular volume of some selected molecules compared to the molecular volumes computed using hard spheres and iso-density methods. The SVPE volumes are computed with a surface width of 0.3 and volumes are reported in atomic units cubed

Molecules	MFV	VdWV	SEV	MIDV	SVPE
CH_3COCH_3	77.47	63.56	78.41	73.13	51.64
CH_2CH_2	26.49	36.43	44.25	38.28	37.59
C_6H_{12}	110.26	100.61	118.02	115.71	126.07
CH_3CONH_2	63.42	51.62	65.06	60.46	58.4
H_2O	13.55	16.92	17.5	20.65	20.05
R_{XY}	0.913	0.960	0.929	0.960	1.0

3.5.2 SVPE and Iso-density Results

Solution of the Schrödinger equation for the Hamiltonian of an isolated solute provides the gas phase internal energy E_g as well as the electronic charge density used in solving the Poisson’s equation. The effective Kohn-Sham and Fock Hamiltonians are constructed by adding the reaction potential to the isolated solute Hamiltonians. The new Kohn-Sham and Fock equations are then solved and a new solute charge density which differs from the gas phase counterpart is obtained in each case. Since the charge density changes, the final solute internal energy E_s changes as well. The reaction field energy due to the solute-solvent interaction is defined as follows:

$$E_r = \int_v d^3r' \rho_{tot}(r') U_r(r') \quad (3.51)$$

Using the Ben-Naim convention [98] which states that the solute maintains a fixed position as it is transferred from gas to solvent, the electrostatic free energy of solvation (ΔG_s) is given by

$$\Delta G_s = E_s - E_g + \frac{1}{2}E_r \quad (3.52)$$

Note that only half of the solute-solvent interaction energy is available as free energy, because half of it is used as work to reversibly charge the solute in the presence of the solvent. The total free energy of solvation (ΔG_{sol}), is computed by adding together, the electrostatic free energy (ΔG_{elec}) of solvation, and the cavitation free energy (ΔG_{cav}) $\Delta G_{sol} = \Delta G_{cav} + \Delta G_{elec}$.

Table 3.3: SVPE solvation free energy (at the RHF with a threshold of 10^{-4} and $\sigma = 0.3$). The total solvation free energy (ΔG_{sol}) is the sum of the electrostatic free energy (ΔG_{elec}) of solvation, and the cavitation free energy (ΔG_{cav}). The free energies are in kcal/mol and a dielectric constant of 78.304 for water is used throughout. Our results are compared to the experimental values (ΔG_{expt}) [100, 101] and the literature (electrostatic free energy) values (ΔG_{lit}) [99]

Molecules	ΔG_{expt}	ΔG_{sol}	ΔG_{cav}	ΔG_{elec}	ΔG_{lit}
H_2O	-6.10	-4.57	3.92	-8.49	-8.59
CH_3CONH_2	-9.7	-10.59	11.86	-22.45	-10.86
CN^-	-67.0	-73.42	6.73	-80.15	-67.40
NO^+	–	-103.78	4.35	-108.14	-89.48
CH_4	2.0	4.82	5.69	-0.86	–
C_6H_6	-0.87	6.96	16.77	-9.81	–

We have chosen five solutes for illustration and comparison with other svpe methods (Table 3.3). The most symmetric of these is C_6H_6 and the simplest and roughly symmetric is H_2O . none-symmetric, and neutral CH_3CONH_2 are also reported. To highlight volume polarization effects, we consider two ionic solutes namely the cation NO^+ and the anion CN^- . The van der Waals (vdw) radii of the atoms were $r_H = 1.20\text{\AA}$, $r_C = 1.70\text{\AA}$, $r_N = 1.55\text{\AA}$, $r_O = 1.52\text{\AA}$, $r_{Cl} = 1.75\text{\AA}$, for the SVPE model, and all employ a dielectric constant value of $\epsilon = 78.304$. In Fig. 3.14, we explore for the water molecule with interlocking spheres, the dependence of the surface area (computed as the volume integral of the normal derivative of the characteristic function) on the surface width (σ). Results are reported for the augmented restricted Hartree-Fock (RHF) equation. Converged SVPE results for the selected systems are presented in Table 3.3. Free energies (kcal/mol) are computed at the δ and σ values of $(10^{-4}, 0.3)$. The total free energies of solvation agree satisfactorily with the experimental [100]. The electrostatic solvation free energy in most cases is different from the literature values [99]. The latter employs a different cavity definition and a discontinuous switch between interior and exterior, and hence exact agreement is not expected.

The iso-density solvation model is similar to the model developed by Chipman (both methods use iso-density contours to construct the molecular cavity). The results reported by Chipman [99], uses an iso-density value of $0.001e/a_0^3$ for a fixed molecular cavity. We use a threshold density $\rho_0 = 0.001$ and a β value of 1.3 to compute the solvation free energies at the RHF level of theory with a threshold of 10^{-4} . Results of the computation are reported in Table 3.4. The experimental values agree satisfactorily with the total solvation free energies. The electrostatic free energies differ from the literature values. For both the methane and the benzene molecule, the dispersion-repulsion contribution is not fully captured by the parameterization in both the SVPE and iso-density models; this can be explained by the fact that the solvation process includes contributions from three main sources [81]: electrostatic, dispersion-repulsion, and cavitation (thermal and $P\Delta V$ contributions are negligible and usually

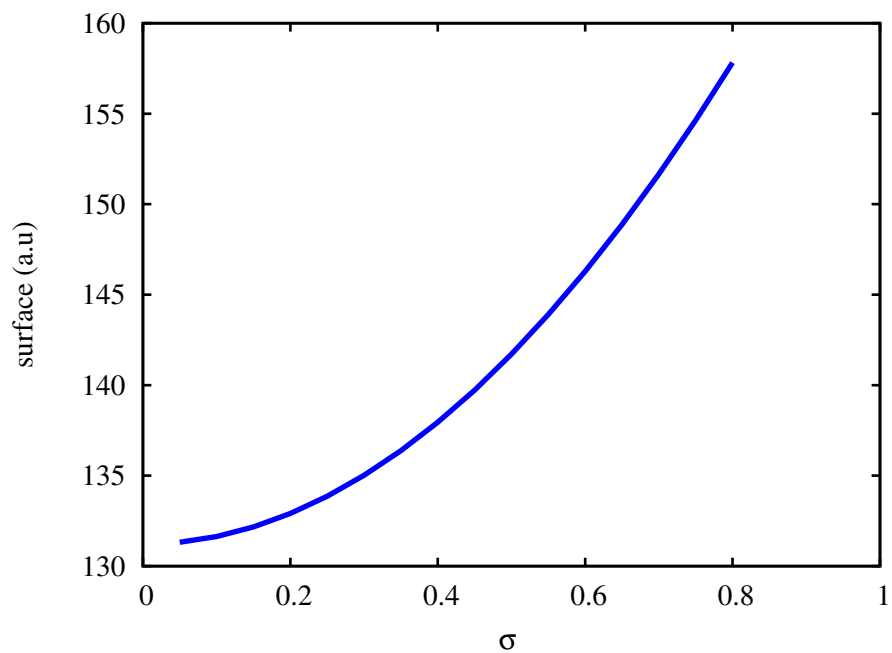


Figure 3.14: Parameterizing the molecular cavity of H_2O molecule. σ is the surface width. The surface area decreases with the surface width

not considered in continuum models). The dispersion-repulsion contribution may be important in hydrophobic and aromatic species, which is not fully captured.

Table 3.4: Iso-density solvation free energy (at the RHF with a threshold of 10^{-4} , $\beta = 1.3$ and $\rho_0 = 0.001a.u/a_0^3$). The total solvation free energy (ΔG_{sol}) is the sum of the electrostatic free energy (ΔG_{elec}) of solvation, and the cavitation free energy (ΔG_{cav}). The free energies are in kcal/mol and a dielectric constant of 78.304 for water is used throughout. Our results are compared to the experimental values (ΔG_{expt}) [100, 101] and the literature (electrostatic free energy) values (ΔG_{lit}) [99]

Molecules	ΔG_{expt}	ΔG_{sol}	ΔG_{cav}	ΔG_{elec}	ΔG_{lit}
H_2O	-6.10	-5.24	4.65	-9.9	-8.59
CH_3CONH_2	-9.7	-7.35	10.03	-17.38	-10.86
CN^-	-67.0	-64.04	5.20	-69.24	-67.40
NO^+	–	-107.92	5.68	-113.59	-89.48
CH_4	2.0	5.45	6.27	-0.81	–
C_6H_6	-0.87	1.67	12.38	-10.77	–

Furthermore, comparison of the iso-density with experiment and the model developed by Fattebert and Gygi [97] is made. For this comparison, we consider thirteen molecular systems, neutral and ionic, and determine the correlation between theory and experiment as well as between literature values and results from this work. The calculations are carried out at the DFT/PBE0 level of theory, a threshold of 10^{-4} , threshold density of $\rho_0 = 0.00088$, and a switching parameter $\beta = 1.3$. The results in [97] are reported at the DFT/PBE with a 6-311G(d,p) basis set, ρ_0 and β values of 0.0078 and 1.3 respectively.

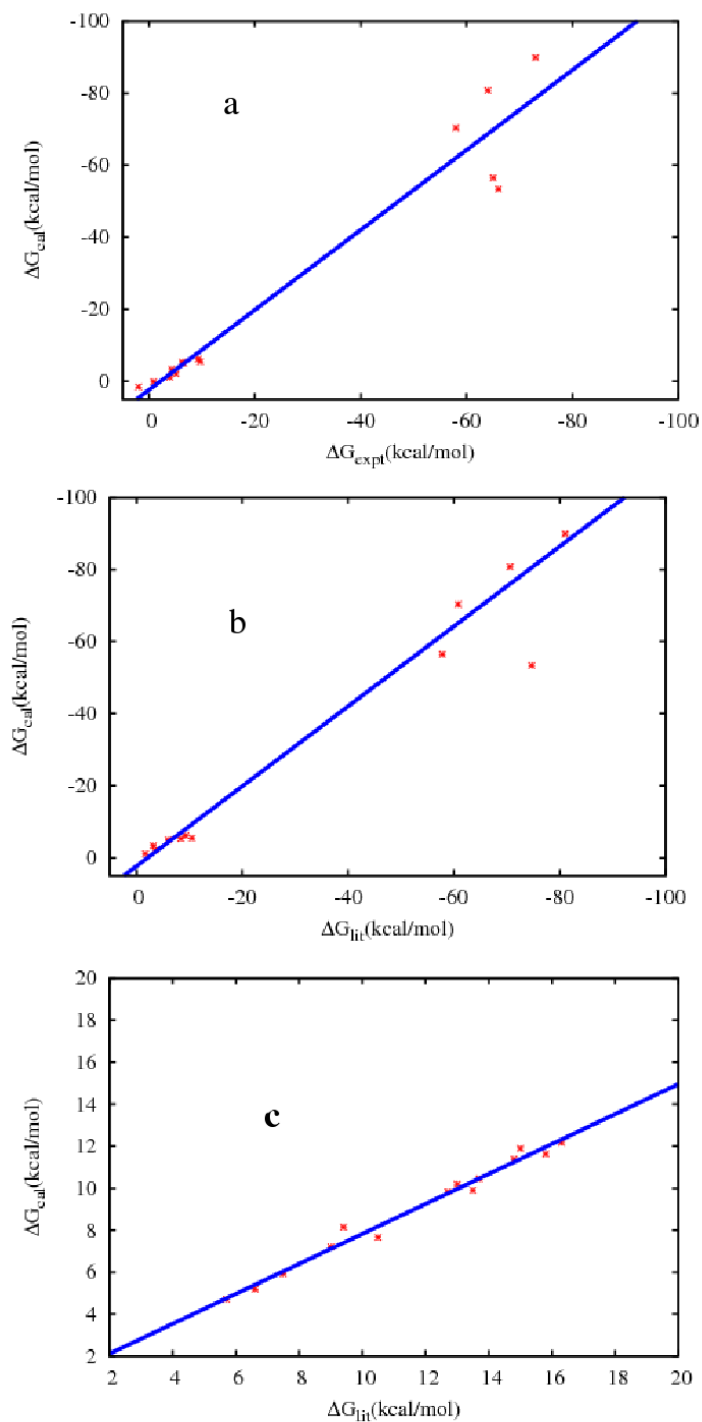


Figure 3.15: Regression analysis of the iso-density solvation model. (a) shows the correlation between calculated (ΔG_{cal}) and the experimental (ΔG_{expt}) solvation free energies, (b) shows the correlation between calculated (ΔG_{cal}) and the literature values of (ΔG_{lit}) solvation free energies, and (c) shows the correlation between calculated (ΔG_{cal}) and the literature values of the cavitation free energy

The free energy of solvation of the neutral molecules, correlates very well with experiment while the solvation free energy of the ionic systems deviates from the experimental values. Fig. 3.15(a) shows the correlation between the calculated and the experimental solvation free energies. The points in the range between 0 and -20 kcal/mol correspond to the correlation between the free energies of neutral molecules while those beyond the -20 kcal/mol value, correspond to the correlation between the free energies of ionic molecules.

Our calculated free energies correlate ($R = 0.67$) relatively with the literature values. The correlation trend follows that observed between the calculated and the experimental free energies of solvation. The iso-density model over-estimates the solvation free energies of cations and under-estimates those of anions. In Fig. 3.15(b) the point at (-74.7, -53.3) is very far off the linear regression line and correspond to the solvation free energy of the dichloro acetate ($CHCl_2COO^-$) that has an experimental value of -66.0 kcal/mol.

The cavitation free energy is a theoretical concept and has no experimental results with which to compare. Thus we compare our results to those obtained by Fattebert and Gygi [97]. Our results correlate ($R = 0.96$) Fig. 3.15(c) very well with those of Fattebert and Gygi. We do not expect a one-to-one correspondence, because our molecular cavity is kept fixed when solving the self-consistent equation whereas Fattebert and Gygi molecular cavity changes with the changing molecular charge density.

3.6 Conclusion

The SVPE and the iso-density solvation models have been presented. The results of the use of multi-resolution multi-wavelet basis functions in the modeling of solvation effects is encouraging. Surface and volume polarization effects are efficiently captured. Very good agreement is achieved between the calculated and the experimental values. A complete implementation will in the near future include the dispersion-repulsion energy and periodic boundary conditions for an extension to periodic systems. The approach is naturally and readily extended to the linear and non-linear Poisson-Boltzmann equations and hence to many different physical applications.

Chapter 4

Gauging Environmental Effects with Static Properties

The system of interest here is a single molecule, which has a static charge distribution. The system's interaction with the external electric field is first treated classically after which the resultant Hamiltonian (interaction) is cast as an operator in the quantum mechanical treatment of the interaction. A general treatment of the static properties are burdensome with complicated formulations [93].

The problem is generally solved in two stages: in the first stage, the assumption is that the charge is defined in terms of the electric dipole alone with the neglect of the higher electric multipoles. The electric field is assumed constant over the charge distribution such that the electric field gradient is zero. In the second stage a more general treatment is carried out with the electric field not being constant over the charge distribution. The gradient of the electric field is not zero. As a consequence, the interaction energy of the distribution of charge will include, the mono-pole, the dipole, the quadrupole, and higher order of moments of the molecule. In our implementation the first assumption is considered.

A finite difference (central difference) method based on energy and dipole moment expansion is used to determine the main static properties. The implementation of

the derived expressions in MADNESS is such that the values and components of the dipole moment (μ), the polarizability (α), the first hyper-polarizability (β) and the second hyper-polarizability (γ) are calculated. The implementation is followed by some applications in comparison to experiment and existing calculations. A further validation of the implementation is followed with examples of some complex molecular systems.

4.1 Molecule in Uniform Static Electric Field

Considering point charges e_i located at positions r_i placed in an external static electric field. The point charge “feels” an electrostatic potential ϕ_i . The energy of interaction U of the external electrostatic potential with the distribution of charges is given by the following equation:

$$U = \sum_i e_i \phi_i \quad (4.1)$$

Application of Taylor’s series expansion at the origin to the scalar potential, leads to the following expressions :

$$U = \sum_i e_i \left[\phi_0 + \left\{ \left(\frac{\partial \phi}{\partial x_j} \right)_0 (x_i - x_0) + \left(\frac{\partial \phi}{\partial y_j} \right)_0 (y_i - y_0) + \left(\frac{\partial \phi}{\partial z_j} \right)_0 (z_i - z_0) \right\} \right] \quad (4.2)$$

Eq. 4.2 is further simplified as follows:

$$U = \sum_i e_i \left[\phi_0 + \left(\frac{\partial \phi}{\partial r_{j\rho}} \right) r_{i\rho} + 0(r_{i\rho}^2) \right] \quad (4.3)$$

where ϕ_0 is the potential at the origin and the subscript ρ denoting cartesian coordinates component such that $r_{i\rho}$ could be $x_i - x_0$, $y_i - y_0$, or $z_i - z_0$. The derivatives are evaluated at the origin. By defining $\left(\frac{\partial \phi}{\partial r_\rho} \right)_0 = -(E_\rho)_0$, the interaction

energy reduces to the following expression:

$$U = Q\phi_0 - p_\rho (E_\rho)_0 \quad (4.4)$$

where Q is the total charge on the molecule, $(E_\rho)_0$ is the ρ component of the electric field at the origin and p_ρ is the ρ component of the electric dipole moment. For a neutral molecule U is written as $-p_\rho(E_\rho)_0$ and in vector form as follows:

$$U = -\mathbf{p} \cdot (\mathbf{E})_0 \quad (4.5)$$

Alternatively, Eq. 4.5 is written as $U = -p(E)_0 \cos\theta$ where θ is the angle between the dipole moment vector and the electric field vector. Minimum interaction between the electric dipole moment vector and the electric field vector occurs when both vectors lie parallel to each other, that is when $\theta = 0$. Up to this point the treatment has been classical. The quantum mechanical interaction is given by Eq. 4.6

$$\hat{H} = -\hat{\mathbf{r}} \cdot (\mathbf{E})_0 \quad (4.6)$$

In MADNESS, the Fock operator and the Kohn-Sham equation are augmented by $-\hat{\mathbf{r}} \cdot (\mathbf{E})_0$ this then accounts for the interaction of the electronic charge density with the external electric field. The molecular dipole is computed in MADNESS as follows:

$$\mu = \int \mathbf{r} \rho d\tau \quad (4.7)$$

$\hat{\mathbf{r}}$ is the position operator with cartesian components $\hat{X} \vec{i} + \hat{Y} \vec{j} + \hat{Z} \vec{k}$ and the electric field is decomposed as follows: $E_{0x} \vec{i} + E_{0y} \vec{j} + E_{0z} \vec{k}$ from which we compute the different components of the dipole moment.

4.2 Permanent and Induced Molecular Dipole in a Uniform Static Electric Field

The electric dipole of Eq. 4.7 has a permanent and a component induced by the external field. For a neutral nonpolar molecule, the dominant dipole is the induced electric dipole. By assuming a weak interaction between the molecule and the electric field, the mathematical formulation of the permanent and induced components of the electric dipole moment are established by expanding the interaction energy U in a Taylor series expansion about the energy in the absence of the field.

$$\begin{aligned}
 U[(E)_0] &= (U)_0 + (E_\rho)_0 \left[\frac{\partial U}{\partial (E_\rho)_0} \right]_{E_0} \\
 &+ \frac{1}{2!} (E_\rho)_0 (E_\sigma)_0 \left[\frac{\partial^2 U}{\partial (E_\rho)_0 \partial (E_\sigma)_0} \right]_{E_0} \\
 &+ \frac{1}{3!} (E_\rho)_0 (E_\sigma)_0 (E_\tau)_0 \left[\frac{\partial^3 U}{\partial (E_\rho)_0 \partial (E_\sigma)_0 \partial (E_\tau)_0} \right]_{E_0} \\
 &+ \frac{1}{4!} (E_\rho)_0 (E_\sigma)_0 (E_\tau)_0 (E_\nu)_0 \left[\frac{\partial^4 U}{\partial (E_\rho)_0 \partial (E_\sigma)_0 \partial (E_\tau)_0 \partial (E_\nu)_0} \right]_{E_0} + \dots
 \end{aligned} \tag{4.8}$$

$(U)_0$ is the energy of the molecule in the absence of the field. Defining the ρ component of the electric dipole moment of the molecule as $p_\rho = -\frac{\partial U[(E)_0]}{\partial (E_\rho)_0}$, an expression for p_ρ is obtained by the partial differentiation of Eq. 4.8 with respect to $(E_\rho)_0$ as follows:

$$p_\rho = p_\rho^{per} - \alpha_{\rho\sigma} (E_\sigma)_0 + \frac{1}{2} \beta_{\rho\sigma\tau} (E_\sigma)_0 (E_\tau)_0 + \frac{1}{6} \gamma_{\rho\sigma\tau\nu} (E_\sigma)_0 (E_\tau)_0 (E_\nu)_0 + \dots \tag{4.9}$$

where

$$p_\rho^{per} = - \left[\frac{\partial U}{\partial (E_\rho)_0} \right]_{E_0} \quad (4.10)$$

$$\alpha_{\rho\sigma} = - \left[\frac{\partial^2 U}{\partial (E_\rho)_0 \partial (E_\sigma)_0} \right]_{E_0} \quad (4.11)$$

$$\beta_{\rho\sigma\tau} = - \left[\frac{\partial^3 U}{\partial (E_\rho)_0 \partial (E_\sigma)_0 \partial (E_\tau)_0} \right]_{E_0} \quad (4.12)$$

$$\gamma_{\rho\sigma\tau\nu} = - \left[\frac{\partial^4 U}{\partial (E_\rho)_0 \partial (E_\sigma)_0 \partial (E_\tau)_0 \partial (E_\nu)_0} \right]_{E_0} \quad (4.13)$$

The electric dipole moment and the energy of a molecule interacting with the electric field can be written in a more general form as follows:

$$\mu_\rho = \mu_\rho^0 - \alpha_{\rho\sigma} (E_\sigma)_0 + \frac{1}{2} \beta_{\rho\sigma\tau} (E_\sigma)_0 (E_\tau)_0 + \frac{1}{6} \gamma_{\rho\sigma\tau\nu} (E_\sigma)_0 (E_\tau)_0 (E_\nu)_0 + \dots \quad (4.14)$$

$$\begin{aligned} U((E)_0) &= U_0 - \mu_\rho (E_\rho)_0 - \frac{1}{2} \alpha_{\rho\sigma} (E_\rho)_0 (E_\sigma)_0 - \frac{1}{6} \beta_{\rho\sigma\tau} (E_\rho)_0 (E_\sigma)_0 (E_\tau)_0 \\ &\quad - \frac{1}{24} \gamma_{\rho\sigma\tau\nu} (E_\rho)_0 (E_\sigma)_0 (E_\tau)_0 (E_\nu)_0 + \dots \end{aligned} \quad (4.15)$$

From Eq. 4.14 permanent p^{per} and induced p^{ind} components of the electric dipole moments can be obtained, with the induced component further splitted into linear (L) and none-linear (NL).

$$p^{ind} = \alpha \cdot \mathbf{E} + \frac{1}{2} \beta \cdot \mathbf{E} \cdot \mathbf{E} + \frac{1}{6} \gamma \cdot \mathbf{E} \cdot \mathbf{E} \cdot \mathbf{E} + \dots \quad (4.16)$$

$$p^{per} = \mu^0 \quad (4.17)$$

$$p^L = \alpha \cdot \mathbf{E} \quad (4.18)$$

$$p^{NL} = \frac{1}{2} \beta \cdot \mathbf{E} \cdot \mathbf{E} + \frac{1}{6} \gamma \cdot \mathbf{E} \cdot \mathbf{E} \cdot \mathbf{E} + \dots \quad (4.19)$$

4.2.1 Calculating the Electric Polarizability

The molecule is considered to be in a uniform electric field aligned along one of the axis of the system (e.g $[E_x, 0.0, 0.0]$. The values of the static properties (μ_ρ , $\alpha_{\rho\rho}$, $\beta_{\rho\rho\rho}$, and $\gamma_{\rho\rho\rho\rho}$) along the axis under consideration can be obtained. The energy expression Eq. 4.15 reduces to

$$U((E)_0) = U_0 - \mu_\rho(E_\rho)_0 - \frac{1}{2}\alpha_{\rho\rho}(E_\rho)_0^2 - \frac{1}{6}\beta_{\rho\rho\rho}(E_\rho)_0^3 - \frac{1}{24}\gamma_{\rho\rho\rho\rho}(E_\rho)_0^4 + \dots \quad (4.20)$$

cutting off Eq. 4.20 at the fourth power of the electric field, and evaluating the energy at four different electric field values $[\pm E_\rho, \pm 2E_\rho]$ leads to four equations with four unknowns which are solved explicitly with the following results:

$$\begin{aligned} \mu_\rho E_\rho &= -\frac{2}{3} [U(E_\rho) - U(-E_\rho)] + \frac{1}{12} [U(2E_\rho) - U(-2E_\rho)] \\ \alpha_{\rho\rho} E_\rho^2 &= \frac{5}{2} U_0 - \frac{4}{3} [U(E_\rho) + U(-E_\rho)] + \frac{1}{12} [U(2E_\rho) - U(-2E_\rho)] \\ \beta_{\rho\rho\rho} E_\rho^3 &= [U(E_\rho) - U(-E_\rho)] - \frac{1}{2} [U(2E_\rho) - U(-2E_\rho)] \\ \gamma_{\rho\rho\rho\rho} E_\rho^4 &= 4 [U(E_\rho) + U(-E_\rho)] - 6U_0 - U(2E_\rho) - U(-2E_\rho) \end{aligned} \quad (4.21)$$

The off-diagonal components of the polarizability, first hyper-polarizability and second hyper-polarizability are computed in a similar way as the diagonal components. Thus, for any combination of two non-zero cartesian component of the external electric field, a new expression for the energy is described as follows:

$$\begin{aligned}
U(E_\rho, E_\sigma) = & U_0 - \mu_\rho E_\rho - \mu_\sigma E_\sigma - \frac{1}{2}\alpha_{\rho\rho}E_\rho^2 - \alpha_{\rho\sigma}E_\rho E_\sigma \\
& - \frac{1}{2}\alpha_{\sigma\sigma}E_\sigma^2 - \frac{1}{6}\beta_{\rho\rho\rho}E_\rho^3 - \frac{1}{6}\beta_{\sigma\sigma\sigma}E_\sigma^3 \\
& - \frac{1}{2}\beta_{\rho\rho\sigma}E_\rho^2 E_\sigma - \frac{1}{2}\beta_{\rho\sigma\sigma}E_\rho E_\sigma^2 \\
& - \frac{1}{24}\gamma_{\rho\rho\rho\rho}E_\rho^4 - \frac{1}{24}\gamma_{\sigma\sigma\sigma\sigma}E_\sigma^4 \\
& - \frac{1}{6}\gamma_{\rho\rho\rho\sigma}E_\rho^3 E_\sigma - \frac{1}{6}\gamma_{\rho\sigma\sigma\sigma}E_\rho E_\sigma^3 \\
& - \frac{1}{4}\gamma_{\rho\rho\sigma\sigma}E_\rho^2 E_\sigma^2 + \dots
\end{aligned} \tag{4.22}$$

Using the energy expressions from Eq. 4.22 defined at the field positions, $[E_\rho, E_\sigma]$, $[E_\rho, -E_\sigma]$, $[-E_\rho, E_\sigma]$, $[-E_\rho, -E_\sigma]$, the off-diagonal energy expressions are obtained. Solving for the unknowns from the derived off-diagonal energy expressions, the expressions for the off-diagonal polarizability, first hyper-polarizability and second hyper-polarizability are obtained as follows:

$$\begin{aligned}
\alpha_{\rho\sigma}E_\rho E_\sigma = & \frac{1}{48}[U(2E_\rho, 2E_\sigma) - U(2E_\rho, -2E_\sigma) \\
& - U(-2E_\rho, 2E_\sigma) + U(-2E_\rho, -2E_\sigma)] \\
& - \frac{1}{3}[U(E_\rho, E_\sigma) - U(E_\rho, -E_\sigma) \\
& - U(-E_\rho, E_\sigma) - U(-E_\rho, -E_\sigma)]
\end{aligned} \tag{4.23}$$

$$\begin{aligned}
\beta_{\rho\sigma\sigma}E_\rho E_\sigma^2 = & \frac{1}{2}[U(-E_\rho, -E_\sigma) - U(E_\rho, E_\sigma) \\
& + U(-E_\rho, E_\sigma) - U(E_\rho, -E_\sigma)] + U(E_\rho) - U(-E_\rho)
\end{aligned} \tag{4.24}$$

$$\begin{aligned}
\gamma_{\rho\rho\sigma\sigma}E_\rho^2E_\sigma^2 &= -4U_0 - [U(E_\rho, E_\sigma) + U(-E_\rho, -E_\sigma)] \\
&\quad + U(-E_\rho, E_\sigma) + U(E_\rho, -E_\sigma)] \\
&\quad + 2[U(E_\rho) + U(-E_\rho)] + 2[U(E_\sigma) + U(-E_\sigma)]
\end{aligned} \tag{4.25}$$

An alternate method consist of using the induced dipole moment following a similar procedure as for the energy expressions. Evaluating the dipole moment at various field strengths, the following equations are derived:

$$\mu_\rho = \frac{2}{3}[\mu_\rho(E_\rho) + \mu_\rho(-E_\rho)] - \frac{1}{6}[\mu_\rho(2E_\rho) + \mu_\rho(-2E_\rho)] \tag{4.26}$$

$$\alpha_{\rho\rho}E_\rho = \frac{2}{3}[\mu_\rho(E_\rho) - \mu_\rho(-E_\rho)] - \frac{1}{12}[\mu_\rho(2E_\rho) - \mu_\rho(-2E_\rho)] \tag{4.27}$$

$$\alpha_{\rho\sigma}E_\sigma = \frac{2}{3}[\mu_\rho(E_\sigma) - \mu_\rho(-E_\sigma)] - \frac{1}{12}[\mu_\rho(2E_\sigma) - \mu_\rho(-2E_\sigma)] \tag{4.28}$$

$$\beta_{\rho\rho\rho}E_\rho^2 = \frac{1}{3}[\mu_\rho(2E_\rho) + \mu_\rho(-2E_\rho) - \mu_\rho(E_\rho) - \mu_\rho(-E_\rho)] \tag{4.29}$$

$$\beta_{\rho\sigma\sigma}E_\sigma^2 = \frac{1}{3}[\mu_\rho(2E_\sigma) + \mu_\rho(-2E_\sigma) - \mu_\rho(E_\sigma) - \mu_\rho(-E_\sigma)] \tag{4.30}$$

$$\gamma_{\rho\rho\rho}E_\rho^3 = \frac{1}{2}[\mu_\rho(2E_\rho) - \mu_\rho(-2E_\rho)] - [\mu_\rho(E_\rho) - \mu_\rho(-E_\rho)] \tag{4.31}$$

$$\gamma_{\rho\rho\sigma\sigma}E_\rho E_\sigma^2 = \frac{1}{2}[\mu_\rho(E_\rho, E_\sigma) - \mu_\rho(-E_\rho, E_\sigma) + \mu_\rho(E_\rho, -E_\sigma) \tag{4.32}$$

$$- \mu_\rho(-E_\rho, -E_\sigma)] - [\mu_\rho(E_\rho) - \mu_\rho(-E_\rho)] \tag{4.33}$$

Once all the necessary components have been determined, expressions for computing the experimentally relevant quantities are described. For the polarizability, the quantity of interest is the mean polarizability $\langle\alpha\rangle$. This is because the gross selection rule of Raman spectroscopy is that, the polarizability of the molecule should change as it vibrates. Polarizability is a measure of the extent of distortion of a molecule in an electric field, as such, its magnitude not only will depend on the symmetry, but will also depend on the orientation of the molecule with respect to the external electric field. In solution or in the gas phase, the experimental observable is

the mean polarizability.

$$\langle \alpha \rangle = \frac{1}{3} (\alpha_{xx} + \alpha_{yy} + \alpha_{zz}) \quad (4.34)$$

For first hyper-polarizability β , an important quantity to be computed is the scalar projection of the first hyper-polarizability along the dipole moment.

$$\beta_{\mu} = \frac{3}{5} \sum_i \frac{\beta_i \mu_i}{\|\mu\|}, \quad i = x, y, z \quad (4.35)$$

with

$$\beta_i = \sum_j \beta_{ijj}, \quad j = x, y, z \quad (4.36)$$

Finally the mean value of the second hyper-polarizability is computed as follows:

$$\gamma = \frac{1}{5} [\gamma_{xxxx} + \gamma_{yyyy} + \gamma_{zzzz} + 2[\gamma_{xxyy} + \gamma_{xxzz} + \gamma_{yyzz}]] \quad (4.37)$$

4.3 Molecule Physisorbed on a Polarizable Continuum Colloid

The ultimate objective here, is the development of a theoretical method to model surface interaction with a physisorbed molecule. The molecular system will be modeled in detail using quantum mechanics, while surface and the environment will be modeled as a polarizable continuum. A static uniform electric field is applied to the molecule and the static properties of the molecule with the environmental effects are determined as a measure of the reaction of the molecule to the presence of the environmental factors. Various parameters such as the size of the polarizable continuum colloid (PCC), the separation between the PCC and the physisorbed molecule and the solvation effects on the static properties of the molecule will be investigated.

4.3.1 Polarizable Continuum Colloid

The designed and implementation of the polarizable continuum colloid model mirrors the surface volume polarizable electrostatic (SVPE) model developed in Chapter 3, but for the fact that changes have been made to accommodate the features specific to the PCC. The PCC is constructed first as a sphere but could also be an irregular sphere comprising six interlocking (Fig. 4.1) spheres such that its radius is about the diameter of one of the spheres. This design is meant to mimic the silver colloids commonly use in SERS experiments. Just as in SVPE model, a characteristic C function is constructed around the PCC spheres

$$C(r, i) = 1 - \Theta(s(r, i)) = \Theta(-s(r, i)) \quad (4.38)$$

The characteristic function (the PCC mask) enables us to represent a regular as well as an irregular domain such as a PCC cavity that we will employ to solve the Poisson's equation for an electronic distribution of charge near the PCC. The

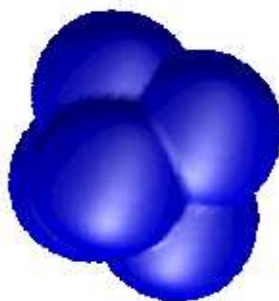


Figure 4.1: Polarizable continuum colloid. The colloid-like particle is made up of six interlocking spheres

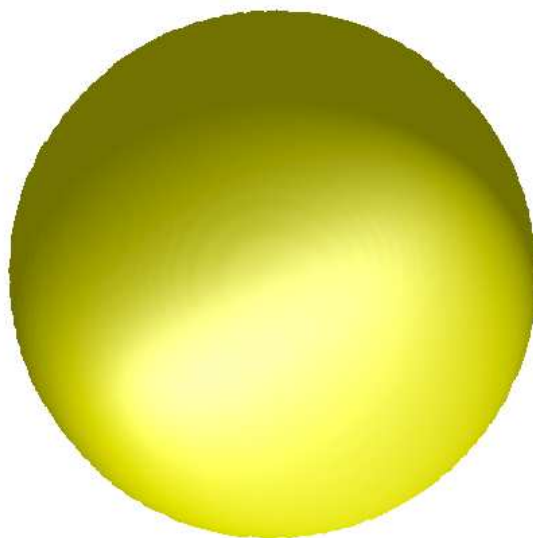


Figure 4.2: Polarizable continuum colloid. The colloid-like particle is single sphere of radius 10.0\AA

colloid is represented implicitly as a dielectric continuum with its dielectric constant ϵ_c . There exist two media separated by the boundary of the irregular domain namely, the inside of the domain which is a metal with an infinite dielectric constant and the outside of the domain which could be a solvent or a vacuum with dielectric constant ϵ_{env} . Defining Ω as our irregular domain, we associate the dielectric constants to the molecular mask $C(r)$ such that we can switch between the inside and outside of Ω . Thus, for this work we define our position dependent dielectric function as follows:

$$\begin{aligned}\epsilon(r) &= \epsilon_0 \exp\left(\log \frac{\epsilon_1}{\epsilon_0}(1 - C(r))\right) \\ \epsilon(r)^{-1} &= \epsilon_0^{-1} \exp\left(\log \frac{\epsilon_0}{\epsilon_1}(1 - C(r))\right) \\ \nabla \log \epsilon(r) &= \frac{\nabla \epsilon(r)}{\epsilon(r)} = \log \frac{\epsilon_0}{\epsilon_1} \nabla C(r)\end{aligned}\tag{4.39}$$

The dielectric constant of a metal is frequency dependent and has a finite value at a given frequency. This finiteness of the dielectric constant at a given frequency is accounted for in the ground state by choosing the dielectric constant that minimizes the total internal energy Fig. 4.3. This approximation is only valid for the static case.

4.3.2 Physisorption Model

The molecule is placed near the PCC with the assumption that no chemical reaction is taking place. Thus, the PCC and the molecule, keep their identities. The PCC-molecule system is subjected to different interactions as defined in the following equation.

$$E_{rxn} = E_{coul} + E_{pol} + E_{disp} + E_{rep}\tag{4.40}$$

E_{rxn} is the total reaction energy; E_{coul} is the Coulombic interaction between the PCC and the molecule, thought of as being isolated from each other; the polarization term E_{pol} represents the mutual polarization between the PCC and the molecule; E_{disp} is the non-classical, quantum mechanical interaction that depends

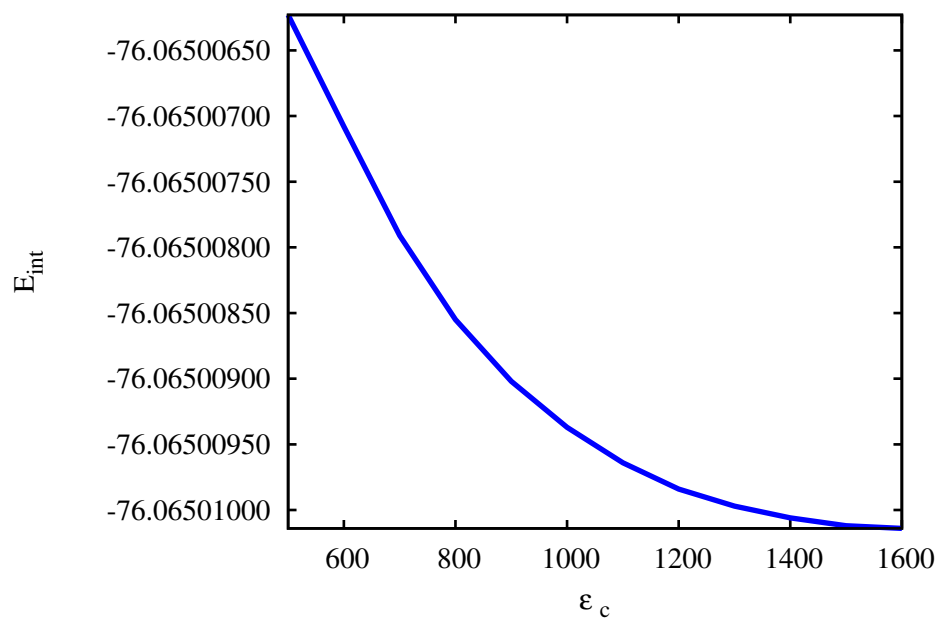


Figure 4.3: Convergence study of the total internal energy (E_{int} in a.u.) of water molecule physisorbed on spherical dielectric particle of radius 18.89a.u. The variation of the internal energy is small for a dielectric constant value between 500 and 1600 ($\Delta E_{int} \approx 10^{-4} kcal/mol$).

on the dynamic polarization of the PCC and the the molecule; E_{rep} depends on the “juxtaposition” of the PCC and the molecule’s electronic charge density. Given the physisorption assumption, only E_{coul} and E_{pol} would be treated. An evaluation of E_{rep} necessitates the knowledge of the electronic structure of both the PCC and the molecule, which is not possible for our physisorption model. Hence, the molecule should not penetrate the PCC. Quantum mechanically, the tail of the wave function will always extend into the PCC in a similar way as in the implicit solvation. The fact that, there is a spillover of the electronic charge density of the molecule does not imply the molecular charge density is less the spillover charge density. All of the electronic charge density of the molecule is taken into account because the PCC and the molecule keep their identities. E_{disp} , though important in the solute-solvent interaction energy [81], it is not of significant importance in the polarizability of the physisorbed molecule. The Coulombic term is identically zero if the PCC has no permanent dipole moment, else the Coulombic and the polarization terms are jointly treated.

4.4 Solving Poisson’s and Laplace’s Equations

At the interface of two dielectrics, the discontinuity leads to surface induced charge. For a spherical conductor in a uniform electric field, the surface induced charge is the reaction of the conductor to the uniform electric field Fig. 4.5. This is the same type of reaction, a spherical PCC will exhibit in the presence of a uniform electric field. The exact electrostatic potential near the sphere, is a solution of Laplace’s equation and is given by the following equations:

$$V(r) = \begin{cases} -E_0 r \cos(\theta) \left(\frac{3\epsilon_0}{\epsilon_1 + 2\epsilon_0} \right), & \text{if } r < R \\ -E_0 r \cos(\theta) + \left(\frac{\epsilon_1 - \epsilon_0}{\epsilon_1 + 2\epsilon_0} \right) E_0 \left(\frac{R}{r} \right)^3 r \cos(\theta), & \text{if } r > R \end{cases} \quad (4.41)$$

where R is the radius of the sphere, r is the distance from the origin of the sphere to

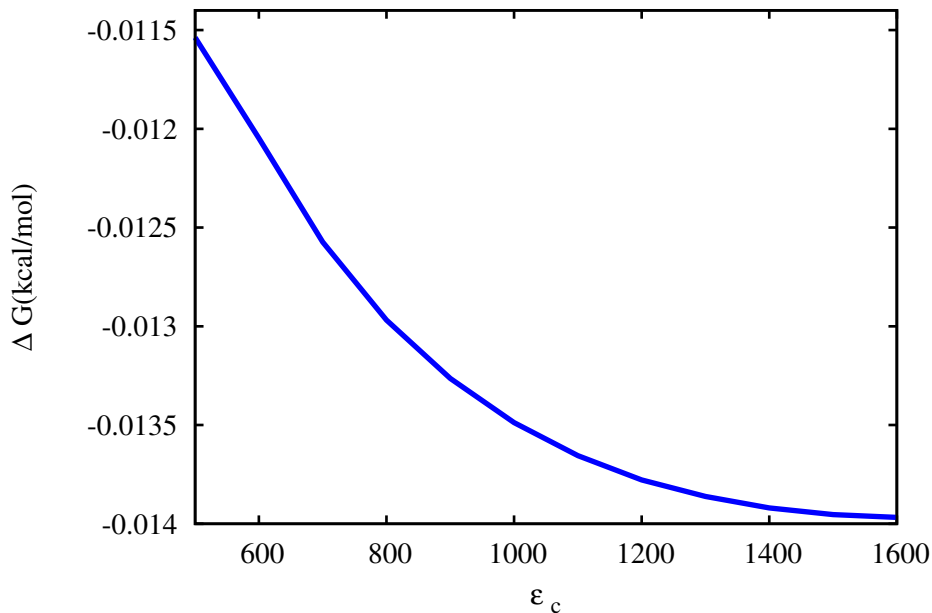


Figure 4.4: Convergence study of the physisorption free energy of water molecule physisorbed on spherical dielectric particle of radius 18.89a.u. The distance from the center of nuclear charge of the water molecule to the sphere’s surface is 3.778a.u.

where the potential is being computed, E_0 is the magnitude of the uniform electric field, and ϵ_0 and ϵ_1 are the dielectric constants exterior and interior to the sphere respectively. For a complicated system such as the interlocking sphere PCC, the calculation of its reaction to an external uniform electric field is not straight forward but can be computed efficiently with our solver.

The default Coulomb Green’s function (free space) in MADNESS has the Dirichlet boundary condition ($U(r \rightarrow \infty) = 0$) imposed on it, while the PCC reaction potential requires Neumann’s boundary condition ($-\partial U/\partial z(r \rightarrow \infty) = E$) to be imposed. The solution to the PCC reaction is the sum of an asymptotic solution ($U = -Ez$) and a component that goes to zero at infinity ($v(r)$). Thus the potential to be inserted into the Laplace equation is of the form: $U(r) = -Ez + v(r)$, where E is the external electric field along the reference axis (z). The Laplace’s equation for a complex PCC is defined by.

$$\nabla(\epsilon(r)\nabla U(r)) = 0 \tag{4.42}$$

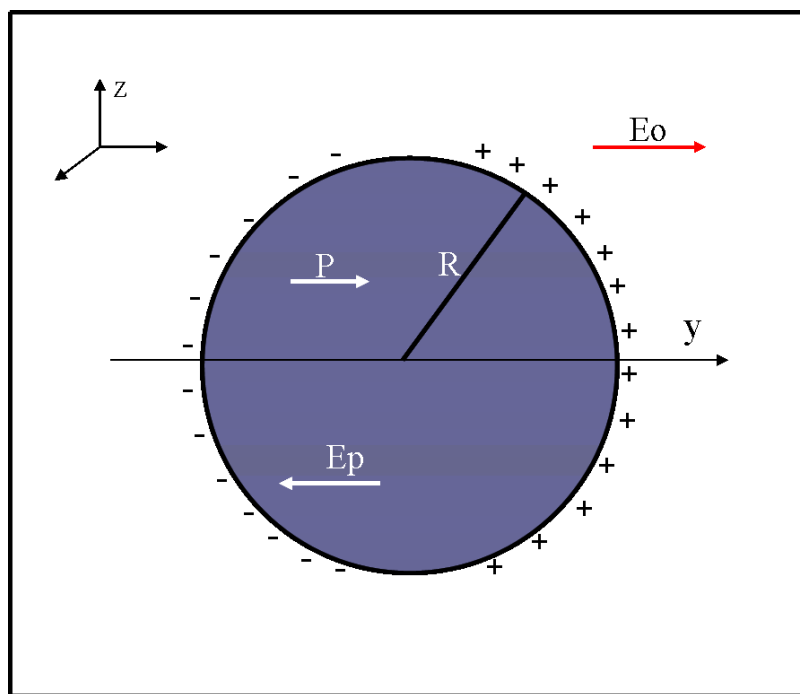


Figure 4.5: Schematic representation of the spherical polarizable continuum colloid. The sphere is polarized by an external electric E_0 . Positive and negative charges are induced on the sphere such that the total surface induced charge is zero.

which can be rearranged to

$$U(r) = \nabla^{-2} \left(-\frac{\nabla \epsilon(r)}{\epsilon(r)} \nabla U(r) \right) \quad (4.43)$$

Eq. 4.43 is solved self-consistently (before the HF and DFT self-consistent fields) for the potential near the colloid with $v(r) = 0$ as the initial guess.

In the limit of $\epsilon_1 \rightarrow \infty$, $V_{in} = 0$ and $V_{ext} = E_0 r \cos(\theta) \left(\left(\frac{R}{r} \right)^3 - 1 \right)$. The effective dielectric coefficient, $\left(\frac{\epsilon_1 - \epsilon_0}{\epsilon_1 + 2\epsilon_0} \right) = 1$. A quantitative relationship is established by applying series expansion on the denominator of the effective dielectric coefficient as follows:

$$\begin{aligned} \left(1 - \frac{\epsilon_0}{\epsilon_1} \right) \left(1 + 2\frac{\epsilon_0}{\epsilon_1} \right)^{-1} &= \left(1 - \frac{\epsilon_0}{\epsilon_1} \right) \left(1 - 2\frac{\epsilon_0}{\epsilon_1} \right) + O \left(\left(\frac{\epsilon_0}{\epsilon_1} \right)^2 \right) \\ &= \left(1 - 3\frac{\epsilon_0}{\epsilon_1} \right) + O \left(\left(\frac{\epsilon_0}{\epsilon_1} \right)^2 \right) \end{aligned} \quad (4.44)$$

Thus, using the first term of the resulting series expansion, for a two digits of accuracy the following relationship is established:

$$3\frac{\epsilon_0}{\epsilon_1} \leq 0.01 \quad (4.45)$$

this leads to $\epsilon_1 \geq 300\epsilon_0$, confirming the convergence studies of Fig. 4.3 The reaction potential of the PCC-molecule system is computed by solving the Poisson's equation. The reaction potential from the interaction of the external electric field with the PCC is reduced by about 28.6% when the PCC is solvated (compare the peaks and the bottoms of the exact and computed potentials from Fig 4.6 and Fig. 4.7.)

$$\nabla (\epsilon(r) \nabla U(r)) = -4\pi \rho_{tot}(r) \quad (4.46)$$

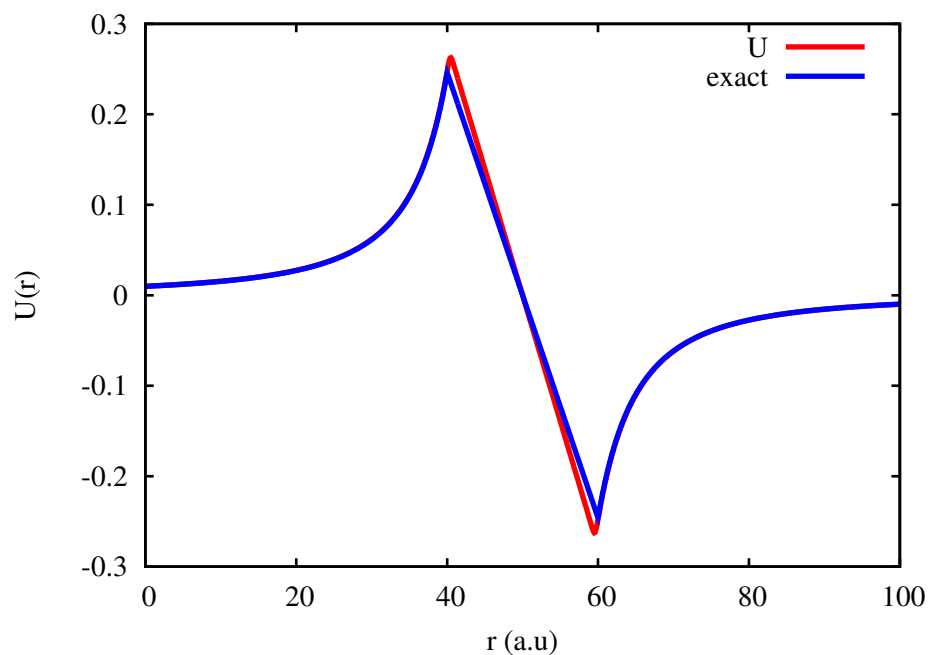


Figure 4.6: Exact and computed reaction potential near the PCC (from Laplace's equation) due to the external electric field.

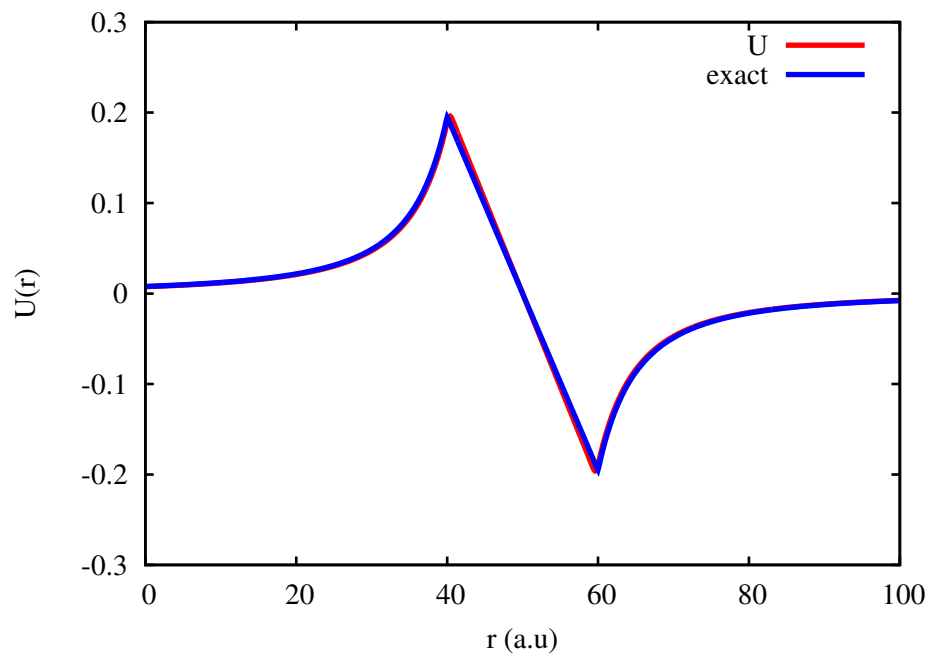


Figure 4.7: Exact and computed reaction potential near the solvated PCC (from Laplace's equation) due to the external electric field.

$\rho_{tot}(r)$ is the sum of the nuclear and electronic charge densities. For a physisorbed molecule in a uniform electric field, the total electrostatic potential U_{tot} near the PCC is the sum of the electrostatic potentials from solving the Laplace's and Poisson's equations. The reference potential is the free space potential U_{vac} (electrostatic potential of the molecule in the absence of the PCC and the uniform electric field). The potential near the PCC is therefore the difference between these two.

$$U_{eff} = U_{tot} - U_{vac} \quad (4.47)$$

In the absence of the uniform electric field, only the Poisson's equation is solved for the total electrostatic potential near the PCC. Our physisorption model makes it possible for the inclusion of other environmental effects such as solvation. Our assumptions are such that the PCC and the molecule keep their identities. Hence, two different implicit models are used and for which the inclusion of the effects of solvation is straight forward: through the SVPE implicit model, solvation effects are included to the PCC and to the molecule through the iso-density model. The SVPE model could still have been used, but this will mean more parameters.

The same procedure is followed (as in the reaction of the PCC to the external electric field) to include the effects of solvation. The surface induced charge from environmental effects, is the reaction of the PCC and is calculated as follows

$$\sigma(r) = \nabla^{-2} \left(-\frac{\nabla\epsilon(r)}{\epsilon(r)} \nabla U_{eff}(r) \right) \quad (4.48)$$

The surface induced charge gives rise to a surface potential that in turns, polarizes the molecule

$$U_{pol}(r) = \nabla^{-2} (\sigma(r)) \quad (4.49)$$

$U_{pol}(r)$ is used to augment the Shrödinger's equation (Hartree-Fock and Density Functional Theory). The molecular charge density reaction to the presence of the PCC. Thus, the change in internal energy of the molecule ΔE_{int} is computed as

the difference between the internal energy of the molecule in its gas phase and the internal energy of the physisorbed molecule.

$$\Delta E_{int} = E_{phys}(\rho_M) - E_{vac}(\rho_M^0) \quad (4.50)$$

$E_{phys}(\rho_M)$ is the internal energy of the polarized molecule and $E_{vac}(\rho_M^0)$ is the internal energy of the molecule in vacuo. An updated molecular charge density is computed as the Hamiltonian is updated. The electrostatic interaction energy also changes as the molecule comes closer to the PCC. The electrostatic potential energy between the PCC and the molecule is evaluated by making use of the updated total molecular charge density and surface induced charge of the PCC.

$$E_{elec} = \frac{1}{2} \int dr U(\sigma(r)) \rho_{tot}(r) \quad (4.51)$$

In cases where solvation and uniform static electric field are included, ρ_M accounts for all these reaction fields. The electrostatic free energy of interaction G_{rxn} is then given by the following equation

$$G_{rxn} = \frac{1}{2} \int dr U(\sigma(r)) \rho_{tot}(r) + \Delta E_{int} (\rho_M^0 \rightarrow \rho_M) \quad (4.52)$$

4.5 Static Properties of Physisorbed Molecule

The static properties of physisorbed molecule are similar to those of a molecule in a vacuum. The Kohn-Sham's or Hartree-Fock's equations are augmented with the reaction potential from PCC-molecule interaction. The Hamiltonians described below are added to the vacuo Hamiltonian for a full description of the system.

- In a uniform static electric field, the in-vacuo Hamiltonian is augmented by

$$- \hat{\mathbf{r}} \cdot (\mathbf{E})_0 \quad (4.53)$$

- In a solvent, the in-vacuo Hamiltonian is augmented as follows:

$$\hat{U}_{rxn}(r) \tag{4.54}$$

- For a physisorbed molecule the augmentation of the in-vacuo Hamiltonian, includes the polarization potential $U_{pol}(r)$

$$\hat{U}_{pol}(r) \tag{4.55}$$

- physisorbed-solvated molecule, has an in-vacuo Hamiltonian that includes the reaction potential $U_{rxn}(r)$ of the solvent as well as the polarization potential of the PCC.

$$\hat{U}_{rxn}(r) + \hat{U}_{pol}(r) \tag{4.56}$$

- A physisorbed molecule in a uniform static electric field, has its in-vacuo Hamiltonian augmented by

$$\hat{U}_{pol}(r) - \hat{\mathbf{r}} \cdot (\mathbf{E})_0 \tag{4.57}$$

- A solvated molecule in a uniform static electric field, has its in-vacuo Hamiltonian augmented by

$$\hat{U}_{rxn}(r) - \hat{\mathbf{r}} \cdot (\mathbf{E})_0 \tag{4.58}$$

- Finally, a solvated-physisorbed molecule in a uniform static electric field, has its in-vacuo Hamiltonian augmented by

$$\hat{U}_{pol}(r) + \hat{U}_{rxn}(r) - \hat{\mathbf{r}} \cdot (\mathbf{E})_0 \tag{4.59}$$

The total Hamiltonian of the entire system changes as well as the density of the molecule in reaction to the presence of the environmental effects.

The inclusion of the environmental effects leads to a consideration of the effective static properties of the physisorbed molecule. These properties are computed, by taking into account the static properties of the molecule in vacuum to which reaction fields due to environmental changes have been included. The effective linear static properties are computed from the induced dipole. The effective dipole (this definition is same as in [112, 113]) from which the effective polarizability is computed is defined as follows:

$$\mu_{eff} = \langle \alpha \rangle (E_0 + \langle E \rangle) \quad (4.60)$$

The effective polarizability then follows:

$$\alpha_{eff} = \frac{\mu_{eff}}{E_0} \quad (4.61)$$

$\langle E \rangle$ is the average reaction field, from the environmental effects. It is computed from the surface reaction potential and the molecular mask $C(r)$ (the boundary around the molecule). The cartesian component of the surface reaction field E_i is computed as the negative gradient of the surface electrostatic potential $U(\sigma(r))$, $i \in \{x, y \text{ or } z\}$.

$$E_i = -\frac{1}{4\pi} \frac{\partial U(\sigma(r))}{\partial r_i} \quad (4.62)$$

$\sigma(r)$ is the surface induced charge at a point r on the surface. The average reaction field, experienced by the molecule, in the x , y and z directions are computed as follows:

$$\langle E_i \rangle = \frac{\int E_i C(r) d\tau}{\int C(r) d\tau} \quad (4.63)$$

The average reaction field, experienced by the molecule, is finally computed as

$$\langle E \rangle = \sqrt{\sum_i \langle E_i \rangle^2} \quad (4.64)$$

4.6 Results and Discussion

Systems of different symmetries and charge distribution were tested and their results compared to other models. The tested systems include, water, acetamide, benzene and Hydrogen fluoride. The Hydrogen fluoride system was used to carry out a convergence test for both the energy and dipole expansions.

Table 4.1: Components of the dipole moment and the polarizability of Hydrogen Fluoride at different magnitudes of the static electric field. The components are computed with the dipole method at a threshold of 10^{-6} .

Components	0.001	0.002	0.003	0.004	0.005	0.01
μ_x	0.0000	0.0000	0.0000	0.0000	0.0000	0.0000
μ_y	0.0000	0.0000	0.0000	0.0000	0.0000	0.0000
μ_z	0.7515	0.7515	0.7515	0.7515	0.7514	0.7515
α_{xx}	4.4800	4.4797	4.4799	4.4798	4.4797	4.4798
α_{yy}	4.4792	4.4799	4.4798	4.4796	4.4796	4.4794
α_{zz}	5.6825	5.7028	5.6880	5.6887	5.6927	5.6900
α_m	4.8806	4.8875	4.8826	4.8827	4.8839	4.8831
α_{xy}	0.0000	-0.0001	-0.0002	-0.0001	0.0000	0.0000
α_{yx}	-0.0002	0.0004	-0.0001	0.0000	0.0000	-0.0001
α_{xz}	0.0005	-0.0001	0.0002	-0.0001	0.0000	0.0000
α_{yz}	-0.0007	0.0000	-0.0002	-0.0001	0.0000	0.0000
α_{zx}	-0.0006	-0.0153	-0.0075	-0.0072	-0.0059	-0.0028
α_{zy}	-0.0043	-0.0156	0.0108	0.0089	0.0075	0.0011

Components of the dipole and the polarizability in table 4.1 show that sufficient numerical accuracy is obtained with a field $E_0 = 0.01$. Tables 4.3 , and 4.2 demonstrate insufficient numerical precision to compute higher moments while Table 4.4 shows that numerical differentiation of the energy does not provide results with numerical accuracy.

Table 4.2: Components of the second hyper-polarizability of Hydrogen Fluoride at different magnitude of the static electric field. The components are computed with the dipole representation at a threshold of 10^{-6} .

Components	0.001	0.002	0.003	0.004	0.005	0.01
γ_{xxxx}	-165.0000	340.6250	254.2593	293.5156	336.4800	328.1900
γ_{yyyy}	1180.0000	238.7500	272.7778	352.5000	314.2400	328.0850
γ_{zzzz}	25359.999	-5069.3750	612.9629	205.2344	144.9600	303.7700
γ_{xxzz}	-55.0000	21.2500	139.4444	96.7969	129.1600	93.0050
γ_{yyxx}	595.0000	56.2500	105.5556	105.3125	120.8400	109.3450
γ_{yyzz}	480.0000	-8.7500	132.9629	116.2500	121.8400	105.1400
γ_{zzxx}	285.0000	-1433.7500	282.2222	152.0312	153.3600	90.8650
γ_{zzyy}	6304.9999	-3032.4999	197.4074	282.5000	97.7200	98.4600
γ_m	5541.0000	-1466.5000	401.7037	314.6563	186.5600	310.652

Table 4.3: Components of the first hyper-polarizability of Hydrogen Fluoride at different magnitude of the static electric field. The components are computed with the dipole method at a threshold of 10^{-6} .

Components	0.001	0.002	0.003	0.004	0.005	0.01
β_{xxx}	0.0400	0.0617	-0.0529	-0.0021	0.0937	-0.0959
β_{yyy}	0.6300	0.0217	0.0270	-0.1392	0.0484	-0.0176
β_{zzz}	24.083	7.8208	9.5555	8.2721	7.5824	7.8656
β_{xyy}	-0.0390	0.0267	-0.0441	-0.0317	-0.0139	-0.0063
β_{yxx}	0.2167	0.0358	-0.0415	-0.0096	-0.0104	-0.0006
β_{xzz}	-0.3333	-0.0833	0.0037	0.0298	0.0031	0.0034
β_{yzz}	0.4900	-0.0275	0.0296	-0.0158	0.0089	-0.0044
β_{zxx}	12.1167	0.3633	-0.6400	-0.7133	-0.1859	-0.4312
β_{zyy}	13.7867	-0.5933	0.5070	0.1246	0.1457	-0.4897
β_x	-0.6833	0.0700	-0.0933	-0.0231	0.0829	-0.0989
β_y	1.3367	0.0300	0.01518	-0.1646	-0.0471	-0.0225
β_z	49.9867	7.5908	9.4225	7.6833	7.5432	6.9447
β	-29.9920	-4.5545	-5.6536	-4.6100	-4.5259	-4.1668

Table 4.4: Components of the dipole moment and the polarizability of Hydrogen Fluoride at different magnitudes of the static electric field. The components are computed with the energy method at a threshold of 10^{-6} .

Components	0.001	0.002	0.003	0.004	0.005
μ_x	0.0000	0.0000	0.0000	0.0000	0.0000
μ_y	0.0000	0.0000	0.0000	0.0000	0.0000
μ_z	0.0000	0.0000	0.0000	0.0000	0.0000
α_{xx}	-5.2267	-4.6837	-4.5231	-4.5170	-4.4853
α_{yy}	-5.0233	-4.6658	-4.5006	-4.5049	-4.4942
α_{zz}	-6.2333	-5.9062	-5.7643	-5.7280	-5.7202
α_m	-5.4944	-5.0853	-4.9293	-4.9166	-4.8999
α_{xy}	-0.0017	-0.0033	-0.0022	0.0000	-0.0016
α_{yx}	-0.0017	-0.0033	-0.0022	0.0000	-0.0016
α_{xz}	0.0575	0.0081	0.0127	-0.0022	0.0033
α_{yz}	0.0000	-0.0047	-0.0034	-0.0011	-0.0008
α_{zx}	0.0575	0.0081	0.0127	-0.0022	0.0033
α_{zy}	0.0000	-0.0047	-0.0034	-0.0011	-0.0008

In table 4.5 , some components of the static properties of Hydrogen Fluoride (FH) from this work’s implementation is compared to similar components from literature. It can be observed that our SCF results are in agreement with those of Hideo Sekino [94]. Besides FH, we have equally compared results from other molecular systems, especially the mean values. Our computed mean polarizabilities of 8.78a.u and 65.04a.u for water and benzene molecules are in agreement with 8.54a.u (at the SCF/t-aug-cc-pVQZ [96]) for water and with 62.72a.u [95] for benzene obtained using the *ab initio* computation together with finite field method. The hyperpolarizabilities of smaller molecules agree with literatures values while those of bigger molecules show some discrepancies.

Table 4.5: The dipole moment, and selected components of polarizability of Hydrogen Fluoride compared to other methods [94]. The components are computed with an electric field magnitude $E_0 = 0.001$ a.u.

Components	SCF (this work)	SCF	TDHF(static)	Experiment
μ_z	0.75	0.76	–	0.707
α_{zz}	5.68	5.76	5.76	6.40
α_{xx}	4.48	4.47	4.47	5.08

4.6.1 Physisorbed Molecules

The static and response properties of the molecules have been computed in-vacuo with noticeable agreement with experimental and other literature values. In the paragraphs that follow, environmental effects on a molecule will be gauged with the polarizability of the targeted system. For these calculations, we have chosen two systems: pyridine (a polar molecule), and methane(a non-polar molecule).

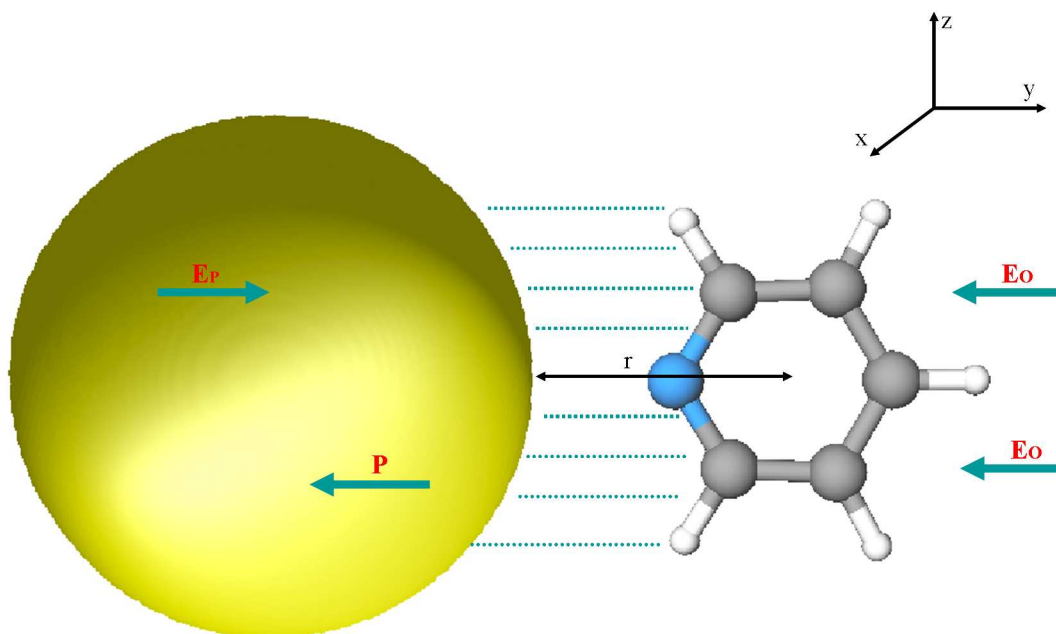


Figure 4.8: Schematic representation of a pyridine molecule physisorbed on spherical polarizable continuum colloid. The molecule and the sphere are in a uniform external electric field (E_0). pyridine and the PCC are held close to each other by the coulombic interactions (here represented as dotted lines)

The gas phase mean value of the polarizability of pyridine, is computed to be $61.3 a_0^3$. This is about 4.4% smaller than the experimental value of $64.1 a_0^3$ [110]. To gauge the physisorption effects of a the spherical PCC on pyridine molecule, we vary the separation r , between the center of charge of the pyridine molecule and the surface of the spherical PCC (results reported in table 4.6).

Table 4.6: Static properties of physisorbed pyridine. Effective polarizability α_{eff} , the mean polarizability α_m , the components of polarizability α_{ii} ($i \in \{x, y, z\}$), the enhancement I , the average reaction electric field, F_{cf} , from the polarization of the spherical PCC (with radius of 10.0 \AA) by the external field ($E_0 = 0.001 \text{ a.u.}$), and the average reaction electric, F_{cm} , from the interaction of the molecule with the spherical PCC. pyridine is described at the restricted Hartee-Fock level of theory with a threshold of 10^{-4} . These values are computed at different PCC-pyridine separation, r (in \AA).

$r(\text{\AA})$	F_{cf}	F_{cm}	I	α_{eff}	α_m	α_{xx}	α_{yy}	α_{zz}
2.0	0.0041	0.1725	$2.17 \cdot 10^4$	$9.02 \cdot 10^3$	50.78	42.68	29.00	80.66
2.5	0.0038	0.0736	$4.78 \cdot 10^3$	$4.24 \cdot 10^3$	54.51	45.51	33.30	83.40
3.0	0.0032	0.0172	$4.50 \cdot 10^2$	$1.30 \cdot 10^3$	60.65	50.16	45.27	86.53
3.5	0.0033	0.0011	26.20	$3.14 \cdot 10^2$	58.17	49.59	40.24	84.67
4.0	0.0030	0.0011	21.60	$2.85 \cdot 10^2$	55.88	48.81	34.96	83.86
4.5	0.0028	0.0009	17.60	$2.57 \cdot 10^2$	54.67	44.24	37.16	82.62
5.0	0.0026	0.0002	12.90	$2.20 \cdot 10^2$	57.83	43.88	48.80	80.81
5.5	0.0024	0.0002	10.40	$1.98 \cdot 10^2$	54.89	42.86	41.39	80.42
6.0	0.0024	0.0001	9.71	$1.91 \cdot 10^2$	54.67	42.38	42.07	79.55

The effective polarizability (α_{eff}) of the physisorbed pyridine is very high for a separation, r , between 2.0\AA and 3.0\AA . This is explained by strong interaction between the external field and the spherical PCC, as well as with the molecule and the PCC. The magnitude of the average reaction electric field from the reaction of the spherical PCC with the external electric field and the molecule is proof of the strength of these interactions (Table 4.6). The magnitude of, α_{eff} , falls as $r \geq 3.0\text{\AA}$ and are within the range of the mean polarizability of pyridine adsorbed on seven clustered atoms of coinage metals ($\alpha_{Au_7} = 380a_0^3$, $\alpha_{Ag_7} = 412a_0^3$, and $\alpha_{Cu_7} = 343a_0^3$) [111]. Another important observation from Table 4.6 is the smaller value of the mean polarizability of the physisorbed molecule when compared to the gas phase value.

The non polar molecule ,methane, is physisorbed on a spherical PCC colloid with a radius of 10.0\AA and an external electric field of 0.01 a.u is applied to the system. The linear (polarizability) and non-linear (first and second hyper-polarizabilities) static properties are then computed at different PCC-methane separation. Table 4.7 shows the values of linear and non-linear static properties of physisorbed methane. The average reaction electric fields due to the reaction of the spherical PCC with the external electric field F_{cf} and due to the PCC-methane interaction F_{cm} .

Table 4.7: Static properties of physisorbed methane. Effective polarizability α_{eff} , the mean polarizability α_m , the enhancement I , the average reaction electric field, F_{cf} , from the polarization of the spherical PCC (with radius of 10.0 Å) by the external field ($E_0 = 0.01$ a.u), the average reaction electric field, F_{cm} , from the interaction of the molecule with the spherical PCC. The methane molecule is described at the restricted Hartee-Fock level of theory with a threshold of 10^{-6} . These values are computed at different PCC-methane separation, r (in Å).

$r(\text{Å})$	F_{cf}	F_{cm}	I	α_{eff}	α_m
2.0	0.0412	0.0060	5.7500	91.2300	15.9500
2.5	0.0377	0.0003	4.8082	76.1680	15.8684
3.0	0.0347	0.0002	4.4990	71.2760	15.8745
3.5	0.0320	0.0001	4.2193	66.8390	15.8763
4.0	0.0300	0.0001	4.0100	63.5380	15.8450
4.5	0.0281	0.0000	3.8075	60.3160	15.8309
5.0	0.0264	0.0000	3.4774	55.0870	15.8295
5.5	0.0248	0.0000	3.4769	55.0780	15.8269
6.0	0.0235	0.0000	3.3442	52.9770	15.8139

The relative large external electric field value of 0.01 a.u used to compute the values in Table 4.7 is to limit the amplification of numerical noise. The magnitude of the effective polarizability decrease as the PCC-methane separation is increased (Fig. 4.9). Close to the spherical PCC, the mean polarizability is larger than the polarizability of methane in the gas phase ($15.8412a.u^3$), this is in contrast to the behavior of the polarizability of pyridine (polar) near the spherical PCC. Depolarization of methane is noticed after a PCC-methane separation of 4.5Å.

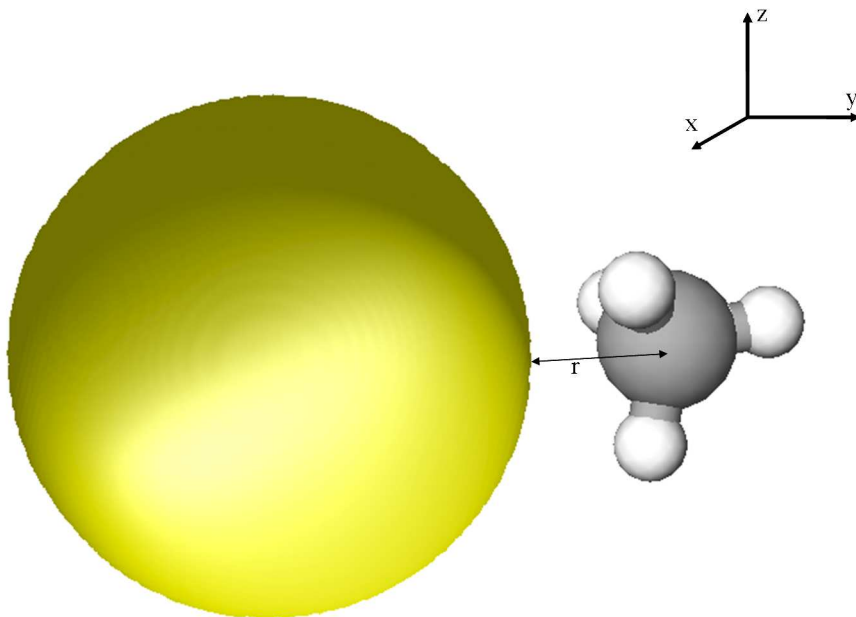


Figure 4.9: Schematic representation of a methane molecule physisorbed on spherical polarizable continuum colloid.

4.6.2 Solvated and Solvated-Physisorbed Molecule

To study the effects of solvation on a physisorbed molecule, we start by computing the mean and effective polarizabilities of a solvated pyridine molecule. The following values of polarizabilities were obtained: $\alpha_{xx} = 30.72a.u^3$, $\alpha_{yy} = 56.17a.u^3$, $\alpha_{zz} = 53.86a.u^3$, for a mean value of $\alpha_m = 46.92a.u^3$. These values are computed for an external electric field of 0.001 a.u that interacts with the dielectric solvent, resulting in a very small average reaction electric field of $4.2 \cdot 10^{-7}a.u$, experienced by the pyridine molecule. An average reaction electric field of 0.0075 a.u also results from the interaction of the pyridine molecule with the dielectric continuum solvent. The polarizability of solvated pyridine confirms the trend observed with the polarizability of the physisorbed molecule. The average reaction field experienced by pyridine, due to interaction between the external electric field and the PCC, is greater than that due to the external electric field interaction with the dielectric solvent; this is simply due to the fact that the PCC is more polarizable than the dielectric continuum solvent.

The molecule is depolarized in all the directions: a depolarization factor of 1.30 for the mean polarizability, 1.34 for the x-component, 1.31 for the y-component and 1.28 for the z-component. the depolarization factor is the ratio of the polarizability in vacuo with that with environmental effects. Though depolarized, an effective polarizability of $398.805 a.u^3$ for the solvated pyridine is obtained.

Likewise, the polarizability of the solvated methane in a uniform external electric field ($E_0 = 0.001$ a.u) is computed: $\alpha_{xx} = 12.59a.u^3$, $\alpha_{yy} = 12.56a.u^3$, $\alpha_{zz} = 12.65a.u^3$, for a mean value of $\alpha_m = 12.60a.u^3$. An average depolarization of 1.26 is achieved. The interaction of methane with solvent gives rise to an average reaction electric field of 0.0045 a.u. Similarly, the solvent interaction with the uniform electric field, leads to an average reaction electric field of $7.2 \cdot 10^{-5}a.u$. The effective polarizability of the solvated methane is then computed as $69.3a.u^3$.

The environmental effects of solvation on the physisorbed molecule is gauged and the results reported in Table 4.8 and Table 4.9. The different components as well as the mean and effective polarizabilities are computed and compared to the polarizability in the gas phase. The molecule is placed in a molecular cavity and the spherical PCC is also encapsulated by the solvent.

Table 4.8: Static properties of solvated-physisorbed pyridine. Effective polarizability α_{eff} , the mean polarizability α_m , the components of polarizability α_{ii} ($i \in \{x, y, z\}$), the enhancement I , the average reaction electric field, F_{cf} , from the polarization of the spherical PCC (with radius of 10.0 Å) by the external field ($E_0 = 0.001$ a.u), the average reaction electric, F_{cm} , from the interaction of pyridine with the spherical PCC, and the average reaction electric, F_{sm} , from the interaction of pyridine with the solvent. The pyridine molecule is described at the restricted Hartee-Fock level of theory with a threshold of 10^{-4} . These values are computed at different PCC-pyridine separation, r (in Å).

(Å)	F_{cf}	F_{cm}	F_{sm}	I	α_{eff}	α_m	α_{xx}	α_{yy}	α_{zz}
2.0	0.0036	0.0006	0.0075	94.115	594.690	46.826	30.588	56.132	53.760
2.5	0.0033	0.0006	0.0075	89.752	580.742	46.834	30.684	56.116	53.703
3.0	0.0030	0.0001	0.0075	80.041	548.426	46.874	30.641	56.149	53.831
3.5	0.0028	0.0000	0.0075	74.774	530.072	46.909	30.713	56.163	53.850
4.0	0.0026	0.0000	0.0075	72.122	520.590	46.900	30.641	56.164	53.895
4.5	0.0024	0.0000	0.0075	69.609	511.439	46.921	30.718	56.188	53.859
5.0	0.0023	0.0000	0.0075	68.271	506.498	46.898	30.640	56.158	53.895
5.5	0.0021	0.0000	0.0075	65.816	497.310	46.916	30.718	56.171	53.860
6.0	0.0020	0.0000	0.0075	64.547	492.492	46.904	30.643	56.171	53.897

The solvated-physisorbed molecules show similar depolarization trend as for the physisorbed and solvated molecules. However, the calculated polarizabilities are constant with the change in PCC-molecule separation, they are of the same magnitudes as those of the solvated molecules. The mean polarizability of the solvated pyridine and solvated methane are respectively $46.92a.u^3$ and $12.60a.u^3$, and are equal in magnitude to the polarizabilities of the solvated-physisorbed pyridine or

methane at any given PCC-molecule separation (Table 4.8 and Table 4.9). Despite, the depolarization, the values of the effective polarizability are still greater than the mean polarizability in the gas phase, due to the strong interactions between the targeted systems and the solvent as well as the interaction between the spherical PCC and the external electric field, giving rise to strong reaction electric fields.

Table 4.9: Static properties of solvated-physisorbed methane. Effective polarizability α_{eff} , the mean polarizability α_m , the components of polarizability α_{ii} ($i \in \{x, y, z\}$), the enhancement I , the average reaction electric field, F_{cf} , from the polarization of the spherical PCC (with radius of 10.0 Å) by the external field ($E_0 = 0.001$ a.u), the average reaction electric, F_{cm} , from the interaction of methane with the spherical PCC, and the average reaction electric field, F_{sm} , from the interaction of methane with the solvent. The methane molecule is described at the restricted Hartee-Fock level of theory with a threshold of 10^{-4} . These values are computed at different PCC-solvated methane separation, r (in Å).

(Å)	F_{cf}	F_{cm}	F_{sm}	I	α_{eff}	α_m	α_{xx}	α_{yy}	α_{zz}
2.0	0.0036	0.0000	0.0045	52.56	114.85	12.621	12.609	12.657	12.598
2.5	0.0033	0.0000	0.0045	49.06	110.96	12.612	12.610	12.657	12.572
3.0	0.0030	0.0000	0.0045	45.80	107.21	12.613	12.610	12.656	12.574
3.5	0.0028	0.0000	0.0045	43.67	104.69	12.614	12.612	12.658	12.571
4.0	0.0026	0.0000	0.0045	41.60	102.17	12.614	12.613	12.656	12.573
4.5	0.0024	0.0000	0.0045	39.56	99.64	12.613	12.611	12.656	12.574
5.0	0.0023	0.0000	0.0045	38.58	98.40	12.615	12.613	12.660	12.573
5.5	0.0021	0.0000	0.0045	36.62	95.86	12.613	12.611	12.656	12.574
6.0	0.0020	0.0000	0.0045	35.66	94.60	12.613	12.611	12.656	12.573

4.6.3 Environmental Effects

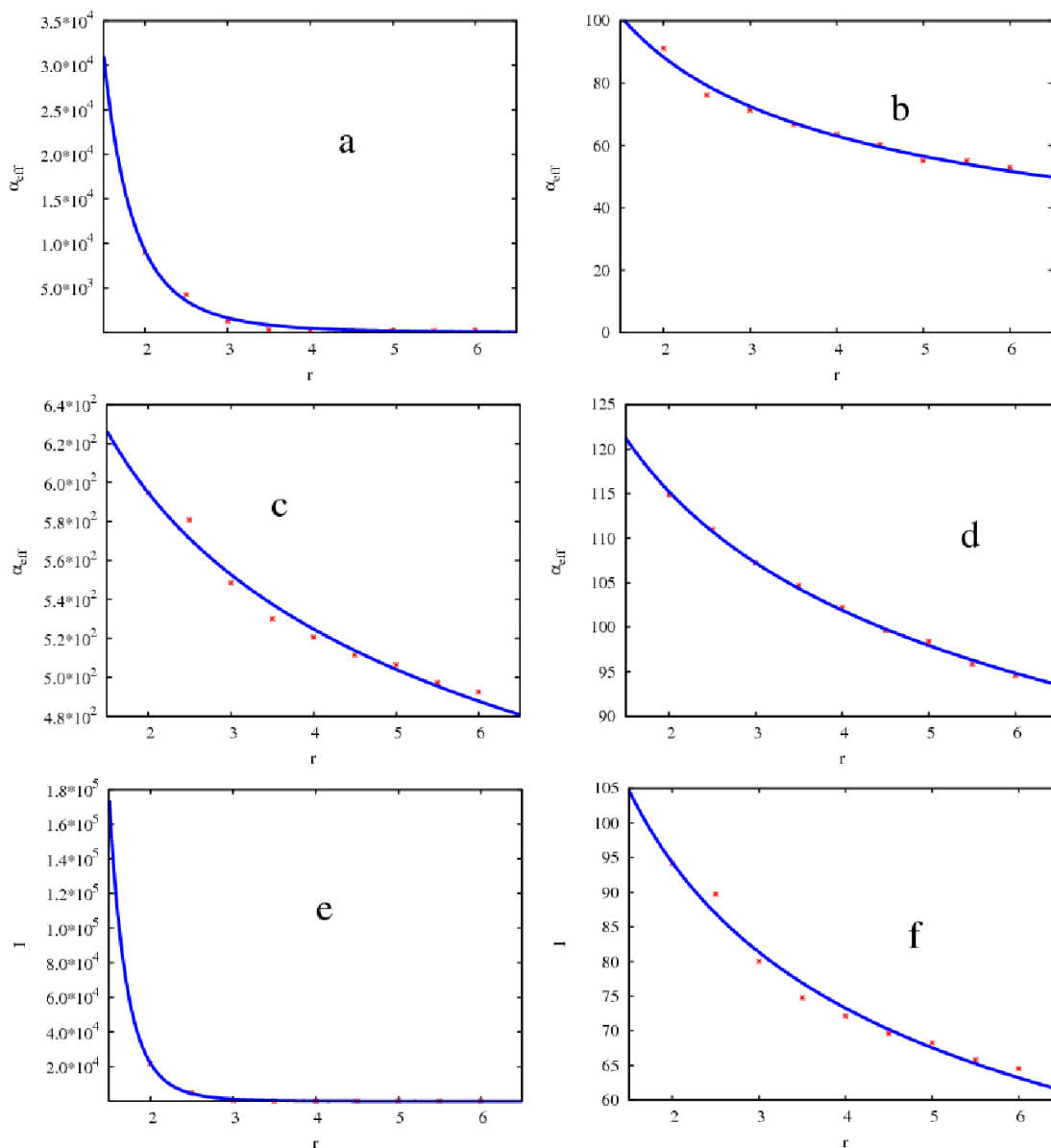


Figure 4.10: Environmental effects on the polarizability of pyridine and methane. (a) and (b) are the effective polarizability (α_{eff}) of the pyridine and methane molecules physisorbed on a spherical PCC. (c) and (d) are the effective polarizability of the solvated pyridine and solvated methane molecules physisorbed on a spherical PCC. (d) is the enhancement of the polarizability of the physisorbed pyridine molecule and (e) is the enhancement of the polarizability of the physisorbed solvated pyridine molecule on a spherical PCC. r (in \AA) is the separation between the molecule and the spherical PCC while I is the enhancement

Through the computed static polarizability of the targeted systems, we gauge the environmental effects on the static properties of molecules. In the tables in section 4.6.1 and section 4.6.2, the static properties of molecules change with changes to their environment.

The effective polarizability of the physisorbed molecules is greater than the polarizability of the free molecule. It increases as the molecules move away from the spherical PCC. The environmental effect is even more important when the molecule is polar: the effective polarizability of physisorbed pyridine Fig. 4.10(a) is by far greater than that of methane Fig. 4.10(b), whatever the separation between the molecules and the spherical PCC.

The effect of solvation and physisorption on the polarizability are all enhancing when compared to the polarizability of the free molecule in a vacuum (Fig. 4.10(a, b, c, d)). The enhancement is very important for the physisorbed molecule in the gas phase: the enhancement of the polarizability of physisorbed pyridine in the gas phase is in the order of 10^5 Fig. 4.10(e) while the enhancement of the solvated physisorbed pyridine is of the order of 10^2 Fig. 4.10(f). Solvated molecules are shielded from the external electric field. Thus, the molecules are not effectively exposed to the external electric field. The effective polarizability of solvated physisorbed pyridine Fig. 4.10(c) is greater (whatever the separation, r) than the effective polarizability of the of solvated physisorbed methane Fig. 4.10(d).

4.7 Conclusion

The static properties of molecules have been used to investigate environmental effects on them. Physisorbed Molecules in vacuum are more effectively polarized than the free molecule. Solvated molecules are more effectively polarized than the free molecule but less than the physisorbed molecule in vacuum. Polarization of molecules in a given environment (physisorbed, solvated and solvated-physisorbed) is driven by the electrostatic interaction.

Chapter 5

Tunability of the Singlet-Triplet Equilibrium in Organic Biradical Compounds

The work described in this Chapter complements the experimental work carried out (still ongoing at the time of writing) by Professor Musfeldt's research group in the Chemistry Department at the University of Tennessee. The experimental investigation consisted of using magnetic and optical spectroscopy to investigate the tunability of the singlet-triplet equilibrium population in organic biradical compounds [34]. The use of high magnetic field to populate the triplet state is a departure from the traditional electron paramagnetic resonance-based (EPR) Curie law methods for determining the spin gap of a reactive biradical. This new approach provides a more efficient way of determining the spin gap in open shell systems. First principle calculations provides an insight to the experimentally observed features, elucidating the structure property relationship.

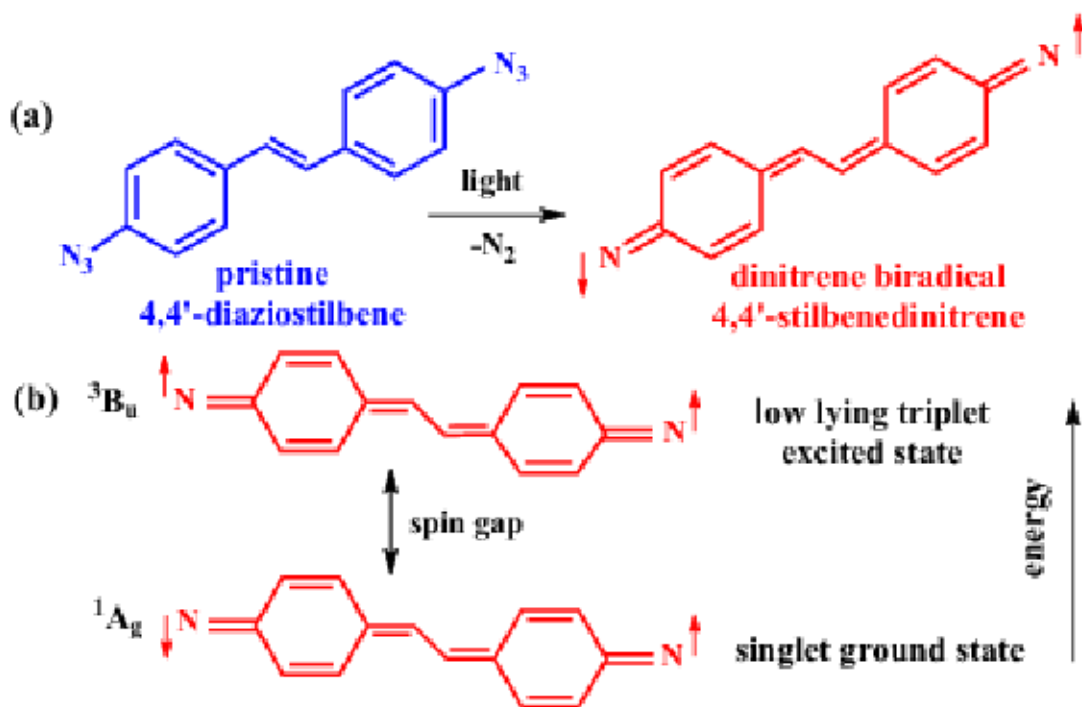


Figure 5.1: (a) Chemical structure of the pristine organic precursor 4,4-diazidostilbene (blue) and the dinitrene biradical 4,4'-stilbenedinitrene (red) after the photochemical reaction. (b) Energy level scheme showing the ¹A_g singlet ground state and the low lying ³B_u triplet excited state of the dinitrene biradical [103]. The triplet state can be accessed with temperature and magnetic field.

5.1 Chemical Systems

The chemical systems investigated here are commonly referred to as quinonoidal diiminediyls, generated from their diazide precursors. The resulting biradicals are stabilized, and trapped in their spin states via low temperature photolysis. In this work, our focus is on two systems, namely: 1,4-phenylenedinitrene and 4,4'-stilbenedinitrene. 1,4-diazidobenzene undergoes a photochemical reaction to yield 1,4-phenylenedinitrene, Fig. 5.2 which is persistent in a rigid matrix at $T \leq 90K$. Its zero-field splitting is estimated by EPR to be about 288K [103]. Likewise, 4,4'-stilbenedinitrene is a chemical-photolytic product of 4,4-diazidostilbene precursor Fig. 5.1. Its EPR spin splitting is estimated at 235K [103]

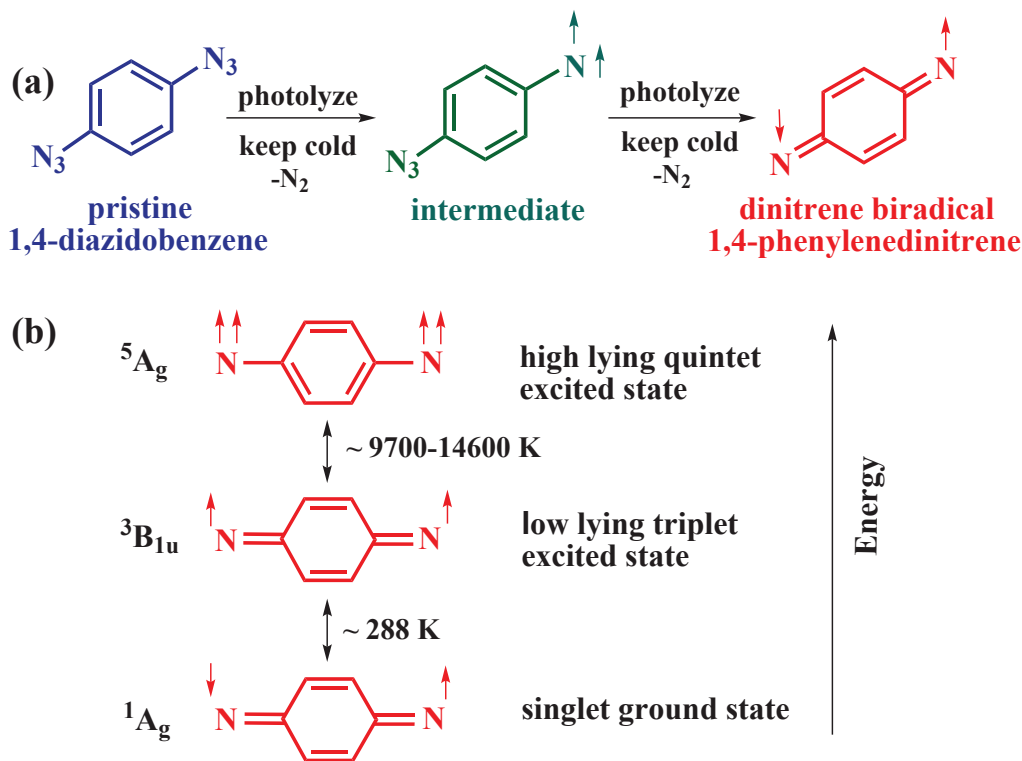


Figure 5.2: (a) Chemical structure of the 1,4-diazidobenzene precursor (blue), the intermediate after partial photolysis (green), and the dinitrene biradical 1,4-phenylenedinitrene (red) after full photochemical reaction. (b) Energy level scheme showing the singlet ground state, low lying triplet, and the high lying quintet excited states of the biradical [103]

5.2 Computational Method

Our choice of theory and methodology is guided by the nature of the electronic structure of our systems. 1,4-phenylenedinitrene and 4,4'-stilbenedinitrene both have two degenerate (or near degenerate) singly occupied molecular orbitals. For clarity, the singly occupied molecular orbitals (MOs) are labelled a and b. Filling these two MOs with the two electrons, we arrived at four different wave-functions, notably, one singlet state and three degenerate triplet states (Fig. 5.3). which we write as follows:

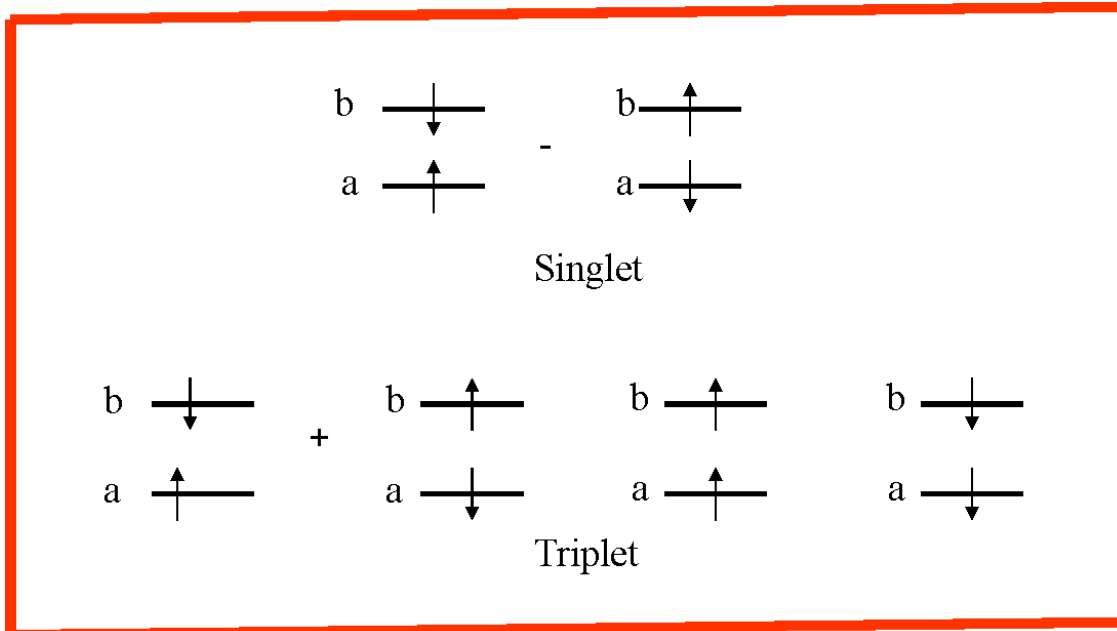


Figure 5.3: Spin configuration for a two electrons and two states scheme. The singlet state is a linear combination of two single reference Slater determinants. The triplet states (lower in energy with respect to the singlet) has one linear combination of two single reference Slater determinant and two single reference Slater determinants

$$\psi_0^1 = 1/\sqrt{2} (|a(\uparrow)b(\downarrow)| - |a(\downarrow)b(\uparrow)|) \quad (5.1)$$

$$\psi_0^3 = 1/\sqrt{2} (|a(\uparrow)b(\downarrow)| + |a(\downarrow)b(\uparrow)|) \quad (5.2)$$

$$\psi_1^3 = |a(\uparrow)b(\uparrow)| \quad (5.3)$$

$$\psi_{-1}^3 = |a(\downarrow)b(\downarrow)| \quad (5.4)$$

ψ_1^3 and ψ_{-1}^3 are single Slater determinants and are straightforward to model in DFT. The singlet (there are two other singlet states, higher in energy, not shown) wavefunction (ψ_0^1) is a linear combination of single Slater determinants and is not readily modeled with DFT. This very simple scheme of spin combination is indicative of the possibility of using the density functional theory and wave function methodologies together in a way as to complement each other. 1,4-phenylene is relatively small in size and can be modeled with the wave-function methodology while 4,4'-stilbenedinitrene is a relatively big molecule as far as using wave-function methodology is concerned.

In the light of this size constraint, both methodologies will be used in a way to reduce the computational cost and at the same time achieve quantitatively and qualitatively acceptable results. The wave-function methodology of choice here is the multi-configuration self-consistency field method (MCSCF) where as the DFT/B3LYP method is the density functional method of choice. The computational procedure consist of using DFT/B3LYP to determine the geometry that minimizes the triplet electronic state energy. The triplet state geometry is then used to carry out single point calculations with MCSCF to determine the electronic state energies of the singlet and the triplet.

In oder to test the validity of the procedure, geometry optimization of 1,4-phenylenedinitrene at the DFT/B3LYP and at the MCSCF with complete active space self-consistent field, in an active space of n electrons in m orbitals(CASSCF[n , m]) was carried out. The 6-311G* basis function was used in both cases. The DFT and the CASSCF[10,10] optimized geometries are then used to carry out single point MCSCF calculations at various CASSCF[n , m] to determine the singlet and triplet electronic state energy from which the spin gap is obtained.

Comparing the DFT and CASSCF[n , m] geometries as well as the spin gap of 1,4-phenylenedinitrene the computational procedure is validated. Having validated the procedure, the triplet state of 4,4'-stilbenedinitrene is optimized at the DFT/B3LYP and MCSCF/CASSCF[6, 6] respectively using the 6-31G* basis function. The single point calculations are then carried out at the MCSCF level with the [6, 6], [8, 8], [10, 10] and [12, 12] CASSCF configurations with the 6-31G* basis set.

Vertical electronic excitations were carried out on the relaxed structures of the targeted materials. 1,4-phenylenedinitrene was studied using time-dependent density functional theory (TDDFT, B3LYP functional, 6-311+g* basis), and also with configuration interaction (CI) energy-selected with a threshold of $0.0001E_h$ [109](eight frozen core orbitals, 6-31g* basis using orbitals from complete active space self-consistent field with an active space of ten electrons in ten orbitals). For both methods, the lowest 40 states were computed. Although it provides the preferred

single determinant triplet wave-function, the TDDFT is not expected to yield a good description of the biradical singlet spectrum since it does not treat near-degeneracy of the b_{1g} and b_{3u} orbitals (Fig. 5.4).

Similarly, 4,4'-stilbenedinitrene was studied using time-dependent density functional theory (TDDFT, B3LYP functional, 6-311++g** basis, frozen atomic orbitals). For this method, the lowest 40 states were computed. Although it provides the preferred single determinant triplet wave-function, again, the TDDFT is not expected to yield a good description of the biradical singlet spectrum since it does not treat near-degeneracy of the a_g and b_u orbitals (Fig. 5.5).

5.3 Results and Discussion

We discuss the results of the calculations in comparison with some experimental data. The active spaces of the targeted systems are described in a way to capture the chemistry of the biradical. Vertical electronic excitation spectra are displayed with distinguished features assigned. Using a simple two state wave-function scheme coupled with a more complete wave-function scheme that includes singly-occupied, doubly-occupied and virtual-frontier MOs, simple Hartree-Fock and Configuration interaction analytical expressions are used to explore spin exchange and their effects on the electronic spectra of the targeted systems. The spin gap, the vertical excitations and other molecular properties are used to establish a structure property relationship.

5.3.1 Active Spaces

MCSCF calculations necessitate an understanding of the Chemistry of the system under investigation such that the the CASSCF active space is reflective of the chemistry of the system. Normally we will love to include all the electrons in our wave-function but we are limited by the computing power, thus we limit

ourself to the valence electrons. The active spaces for our targeted systems comprise the pi-electrons, the two unpaired electrons and all the associated orbitals. For clarity, the active spaces are divided into three subspaces: the doubly-occupied (DOMO), the singly-occupied (SOMO) and virtual (VMO) molecular orbitals. Fig. 5.4 and Fig. 5.5 are the CASSCF active spaces of 1,4-phenylenedinitrene and 4,4'-stilbenedinitrene

For the ${}^3B_{2u}$ and 1A_g electronic states of 1,4-phenylenedinitrene, the reference state for CASSCF[10, 10] computations was $2b_{1u}^2 1b_{3g}^2 1b_{2g}^2 1b_{1g}^1 1b_{3u}^1 2b_{3g}^0 1a_u^0 1b_{1u}^0$. The 3B_u and the 1A_g electronic states of 4,4'-stilbenedinitrene, has $2a_u^2 3b_g^2 1b_u^1 1a_g^1 3a_u^0 2b_g^0$ as reference state for CASSCF[12, 12] computations; a subset of the CASSCF[18, 18] with reference state $4a_u^2 4b_g^2 1b_u^1 1a_g^1 4a_u^0 4b_g^0$. All of the active space orbitals are predominantly π and π^* in character but for the singly-occupied MOs that are predominantly p_x or p_y in character. The SOMOs are localized on the Nitrogen atoms.

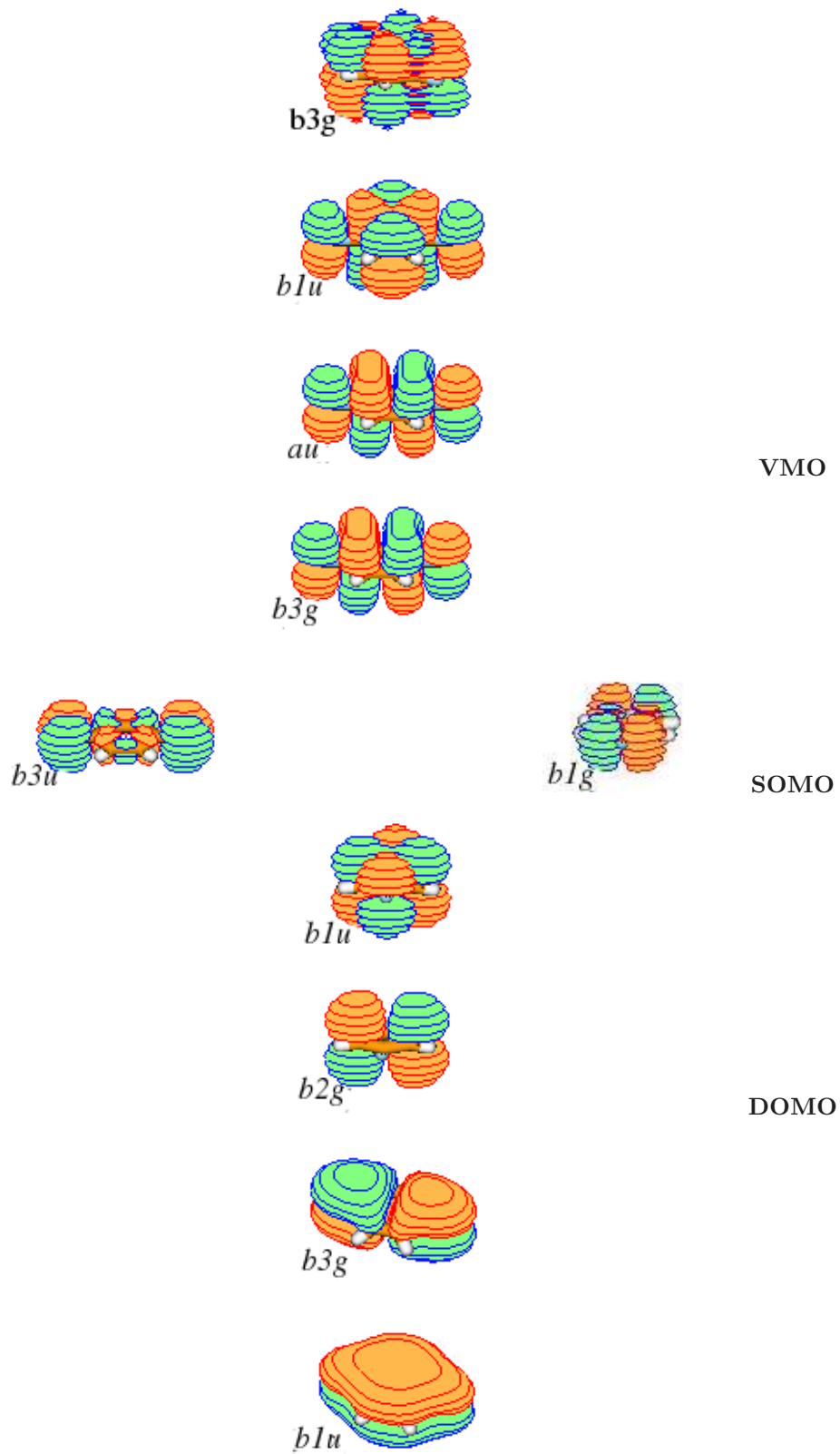


Figure 5.4: MOLDEN plots of the active space orbitals used in the computations of 1,4-phenylenedinitrene.

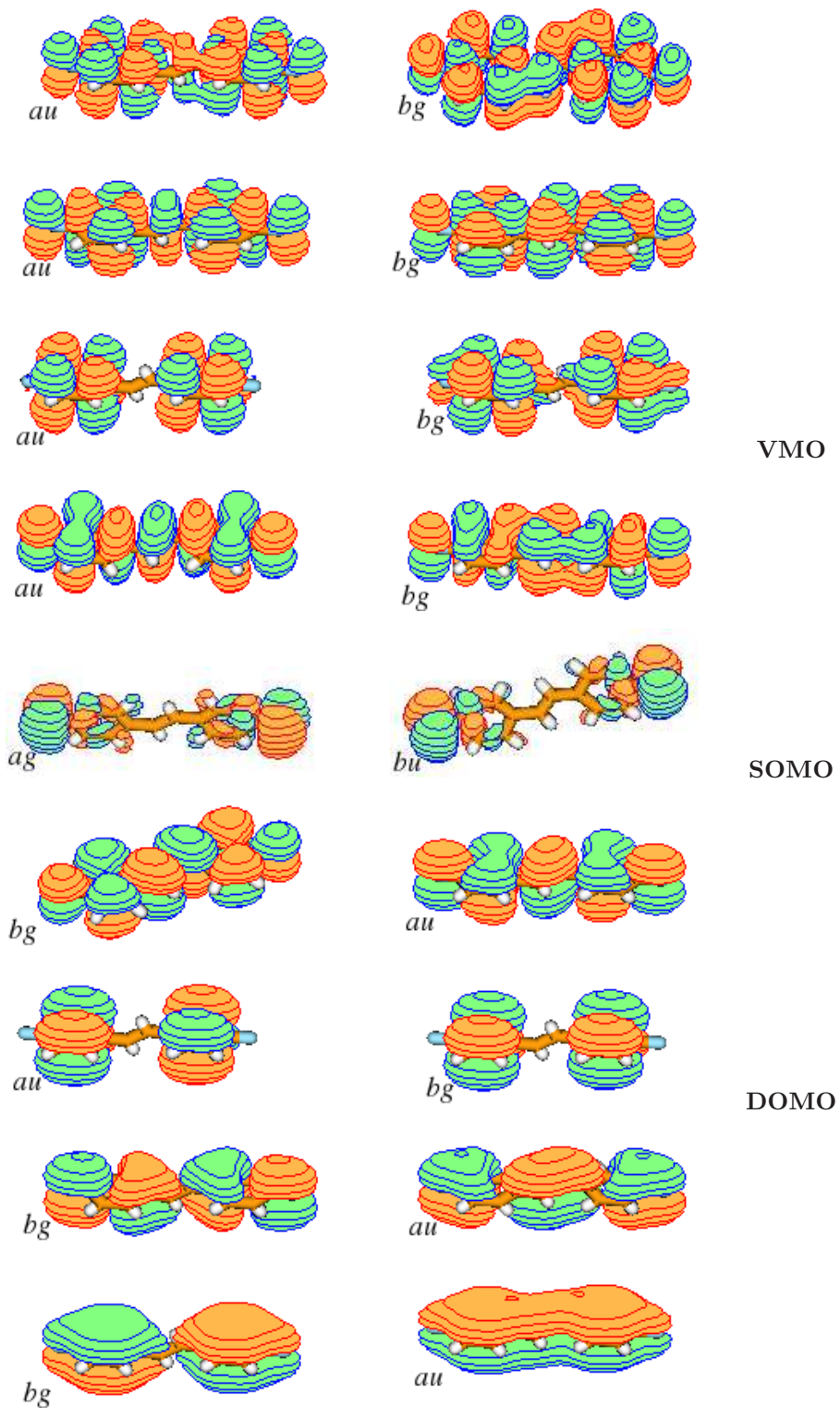


Figure 5.5: MOLDEN plots of the active space orbitals used in the computations of 4,4'-stilbenedinitrene.

5.3.2 Spin splitting

With the appropriate identification of the active spaces, we proceed to computing the spin splitting. Looking at the MCSCF geometries at various CASSCF active spaces (Table 5.3), the change in active space composition does not affect the relaxed geometry. The geometry of any the CASSCF active spaces could be used for single point calculation. Using the MCSCF (CASSCF[10, 10], 6-311G*) relaxed geometry, single point calculations are carried out on 1,4-phenylenedinitrene for the following CASSCF active spaces:[6, 6], [8, 8], [10, 10] and [12, 12]. We repeat the single point calculations with the same CASSCF active spaces, but this time using DFT (B3LYP, 6-311G*) geometry.

Table 5.1: Spin splitting from the DFT (B3LYP, 6-311G*) geometry of the 1,4-phenylenedinitrene triplet with MCSCF single point at different active spaces. units are in Kelvin (kcal/mol) for the spin splitting and in Hartree (E_h) for the electronic state energies

States	[6, 6]	[8, 8]	[10, 10]	[12, 12]	Expt.(Kcal/mol)
$E_{triplet}$	-338.31116	-338.34157	-338.39511	-338.40804	–
Spin	58.459	569.722	583.880	353.670	412.64
splitting	(0.116)	(1.132)	(1.160)	(0.703)	0.82[106]
$E_{singlet}$	-338.31135	-338.34338	-338.39695	-338.40916	–

Table 5.2: Spin splitting from the MCSCF (CASSCF[10, 10], 6-311G*) geometry of the 1,4-phenylenedinitrene with MCSCF single point at different active spaces. units are in Kelvin (kcal/mol) for the spin splitting and in Hartree (E_h) for the electronic state energies

States	[6, 6]	[8, 8]	[10, 10]	[12, 12]	Expt.(Kcal/mol)
$E_{triplet}$	-338.30851	-338.34255	-338.39615	-338.40254	–
Spin	72.059	837.769	713.100	681.914	412.64
splitting	(0.143)	(1.335)	(1.417)	(1.355)	0.82[106]
$E_{singlet}$	-338.30874	-338.34520	-338.39841	-338.40469	–

The results of Table 5.1 and Table 5.2 display common features: Single point calculations for both geometries show a lower energy state for the singlet. In general, the single point energies of the, [6, 6], [8, 8], and [10, 10] active space singlet with CASSCF[10, 10] geometry are about 0.0002 E_h (0.1401kcal/mol) on average lower than the single point energies for similar active spaces with the triplet DFT geometry. Therefore, by using the DFT geometry of the triplet or any geometry of a CASSCF configuration with the active space confined to the valence electrons, we arrived at the same conclusion.

Table 5.3: Inter-nuclear angles θ of the MCSCF(6-311G*) at CASSCF active spaces of [6, 6], [8, 8], [10, 10] for singlet(S), triplet(T) and triplet DFT geometries. For clarity, the MCSCF θ is indexed with the electronic state and the number of electrons.

center 1	center 2	center 3	θ_{S6}	θ_{T6}	θ_{S8}	θ_{T8}	θ_{S10}	θ_{T10}	θ_{DFT}
2 C	1 C	6 C	120.41	120.16	120.09	120.10	120.24	121.36	117.40
2 C	1 C	12 N	119.79	119.92	119.95	119.95	119.88	119.32	121.30
6 C	1 C	12 N	119.79	119.92	119.95	119.95	119.88	119.32	121.30
1 C	2 C	3 C	119.79	119.92	119.95	119.95	119.88	119.32	121.30
1 C	2 C	7 H	117.94	117.80	117.81	117.80	117.92	118.15	117.18
3 C	2 C	7 H	122.27	122.28	122.24	122.25	122.20	122.53	121.52
2 C	3 C	4 C	119.79	119.92	119.95	119.95	119.88	119.32	121.30
2 C	3 C	8 H	122.27	122.28	122.24	122.25	122.20	121.36	121.52
4 C	3 C	8 H	117.94	117.80	117.81	117.80	117.92	118.15	117.18
3 C	4 C	5 C	120.41	120.16	120.09	120.10	120.24	121.36	117.40
3 C	4 C	11 N	119.79	119.92	119.95	119.95	119.88	119.32	121.30
5 C	4 C	11 N	119.79	119.92	119.95	119.95	119.88	119.32	121.30
4 C	5 C	6 C	119.79	119.92	119.95	119.95	119.88	119.32	121.30
4 C	5 C	9 H	117.94	117.80	117.81	117.80	117.92	118.15	117.18
6 C	5 C	9 H	122.27	122.28	122.24	122.24	122.20	122.53	121.52
1 C	6 C	5 C	119.79	119.92	119.95	119.95	119.88	119.32	121.30
1 C	6 C	10 H	117.94	117.80	117.81	117.80	117.92	118.15	117.18
5 C	6 C	10 H	122.27	122.28	122.24	122.25	122.20	122.53	121.52

Given the validation of the computational procedure, we use the MCSCF (CASSCF[6, 6], 6-31g*) geometry as well as that of the DFT (B3LYP, 6-31G*) triplet to compute the MCSCF single point energies of 4,4'-stilbenedinitrene at various CASSCF active spaces as represented in Table 5.4 and Table 5.5. A full representation of the Chemistry, of the targeted system, through the active space require an 18 electrons in 18 MOs configuration space. NWchem [102] can handle a maximum configuration space of 20 electrons in 20 MOs for five hundred basis functions. The single point energy calculations is limited to 12 electrons in 12 MOs CASSCF active space, because our effort to go higher was hindered by IOS problems.

Table 5.4: Spin splitting from the MCSCF (CASSCF[6, 6], 6-31G*) geometry of the 4,4'-stilbenedinitrene singlet. The MCSCF/6-31G* single point calculations are carried out at the specified CASSCF active spaces. The units are Kelvin (kcal/mol) for the spin splitting, and Hartree for the electronic energies

States	[6, 6]	[8, 8]	[10, 10]	[12, 12]	Expt.(Kcal/mol)
$E_{triplet}$	-644.79979	-644.79062	-644.83794	-644.85569	–
Spin	6.688	5.013	1.677	12.299	236.51
splitting	(0.013)	(0.010)	(0.003)	(0.024)	0.47[106]
$E_{singlet}$	-644.79982	-644.79063	-644.83795	-644.855748	–

Table 5.5: Spin splitting from the DFT (B3LYP, 6-31G*) geometry of the 4,4'-stilbenedinitrene triplet. The MCSCF/6-31G* single point calculations are carried out at the specified CASSCF active spaces. The units are Kelvin (kcal/mol) for the spin splitting, and Hartree for the electronic energies

States	[6, 6]	[8, 8]	[10, 10]	[12, 12]	Expt.(Kcal/mol)
$E_{triplet}$	-644.79500	-644.78513	-644.83309	-644.85574	–
Spin	20.9	2.186	3.764	35.176	236.51
splitting	(0.042)	(0.0043)	(0.007)	(0.07)	0.47[106]
$E_{singlet}$	-644.79507	-644.78514	-644.83311	-644.85585	–

Table 5.6: Spin splitting from different experimental techniques. The analysis method used to extract the spin gap is indicated in bracket: population (pop), and Beer’s (Beer). The values in squared brackets correspond to the tuning parameter, The results are compared to the MCSCF results from [106] and this work

Techniques	4,4'-stilbenedinitrene	1,4-phenylenedinitrene
EPR	235k[103]	288k[103] 362K[104] 413K[105]
Optics[T]	190K (pop), 130K (Beer)	230K (pop)[34]
Optics[B]	124K (pop), 90K (Beer)	130K
MCSCF (This work)	35K	354K
MCSCF [106]	20K	352K

The value of the experimental spin splitting vary with the experimental technique. Table 5.6 gives a summary of results obtained using different experimental techniques; from EPR to optics. Magnetic field (B) and Temperature (T) are the experimental tuning parameters used to populate the triplet state. These results are compared to our best MCSCF results and those from [106] (1,4-phenylenedinitrene at CASSCF[8, 8] with 6-31G* and 4,4'-stilbenedinitrene at CASSCF[6, 6] with 3-21G)

5.3.3 Vertical Excitations and Frequency Analysis

First principles calculation of the vertical excitation spectra of the target systems confirms most of the features on the experimental spectra. TDDFT predicts the $b_{1g} \rightarrow b_{3u}$ transition to be at 1750 nm while the most intense feature in the singlet CI spectrum is at 251 nm. On the other hand, since the limited CI expansion recovers only a fraction of the correlation energy, the CI transitions are expected to be too high in energy. Nevertheless, the basic trends are apparent Fig. (5.6). The dipole-allowed spectrum of the triplet species is less intense and at higher energy than that of the singlet, the features in common between the singlet and triplet spectra are primarily $\pi \rightarrow \pi^*$, and many of the lower energy features are either of low intensity or dipole forbidden.

We employed a symmetry analysis, comparison with model compounds, and first principles calculations to assign the transitions. In addition to the strong dipole-allowed $\pi \rightarrow \pi^*$ transitions at $\lambda < 300$, 308, and 345 nm [107], several weak features are observed between 400 and 450 nm that we assign as forbidden $\pi \rightarrow \pi^*$ excitations activated by vibronic coupling, analogous to the situation in C60 [108].

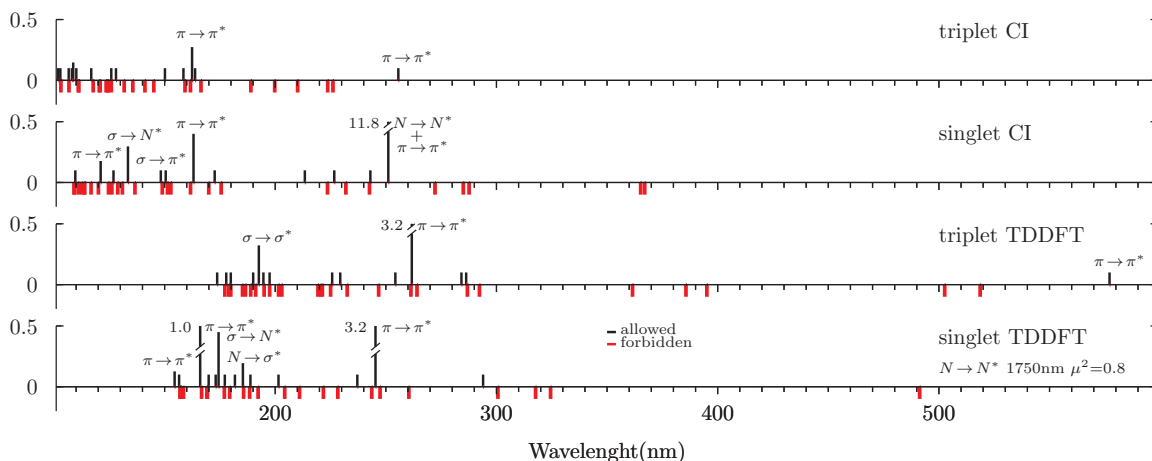


Figure 5.6: TDDFT and selected CI spectra (square of the transition dipole, μ^2 , in atomic units) of 1,4-phenylenedinitrene. For clarity, dipole-allowed transitions are indicated in black. Dipole-forbidden transitions are indicated in red as negative 0.1, weak allowed transitions are increased to 0.1, and intense transitions truncated to 0.5. The most intense feature in the singlet CI spectrum at 251 nm (predominantly $N \rightarrow N^*$ single excitation, with lesser $\pi \rightarrow \pi^*$ single excitation) has $\mu^2 = 12$ and does not appear in the triplet spectrum that has its most intense feature with $\mu^2 = 0.3$ at 162 nm. The spurious low energy features in the singlet TDDFT spectrum are omitted. N and N^* indicate the b_{1g} and b_{3u} orbitals, respectively

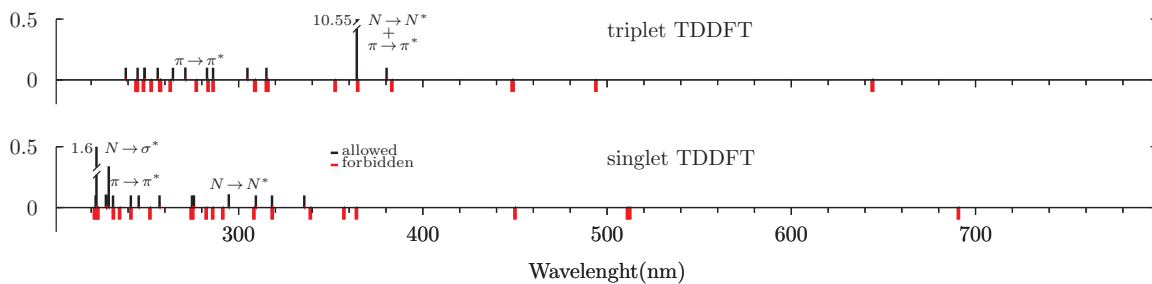


Figure 5.7: TDDFT spectra (square of the transition dipole, μ^2 , in atomic units) of 4,4'-stilbenedinitrene. For clarity, dipole-allowed transitions are indicated in black. Dipole-forbidden transitions are indicated in red as negative 0.1, weak allowed transitions are increased to 0.1, and intense transitions truncated to 0.5. The most intense feature in the triplet TDDFT spectrum occurs at 364 nm (equal contributions from $N \rightarrow N^*$ and $\pi \rightarrow \pi^*$ excitations) has $\mu^2 = 10.55$ and does not appear in the singlet spectrum that has its most intense feature with $\mu^2 = 1.607$ at 222.8489 nm. The spurious low energy features in the singlet TDDFT spectrum are omitted. N and N^* indicate the a_g and b_u singly occupied orbitals, respectively

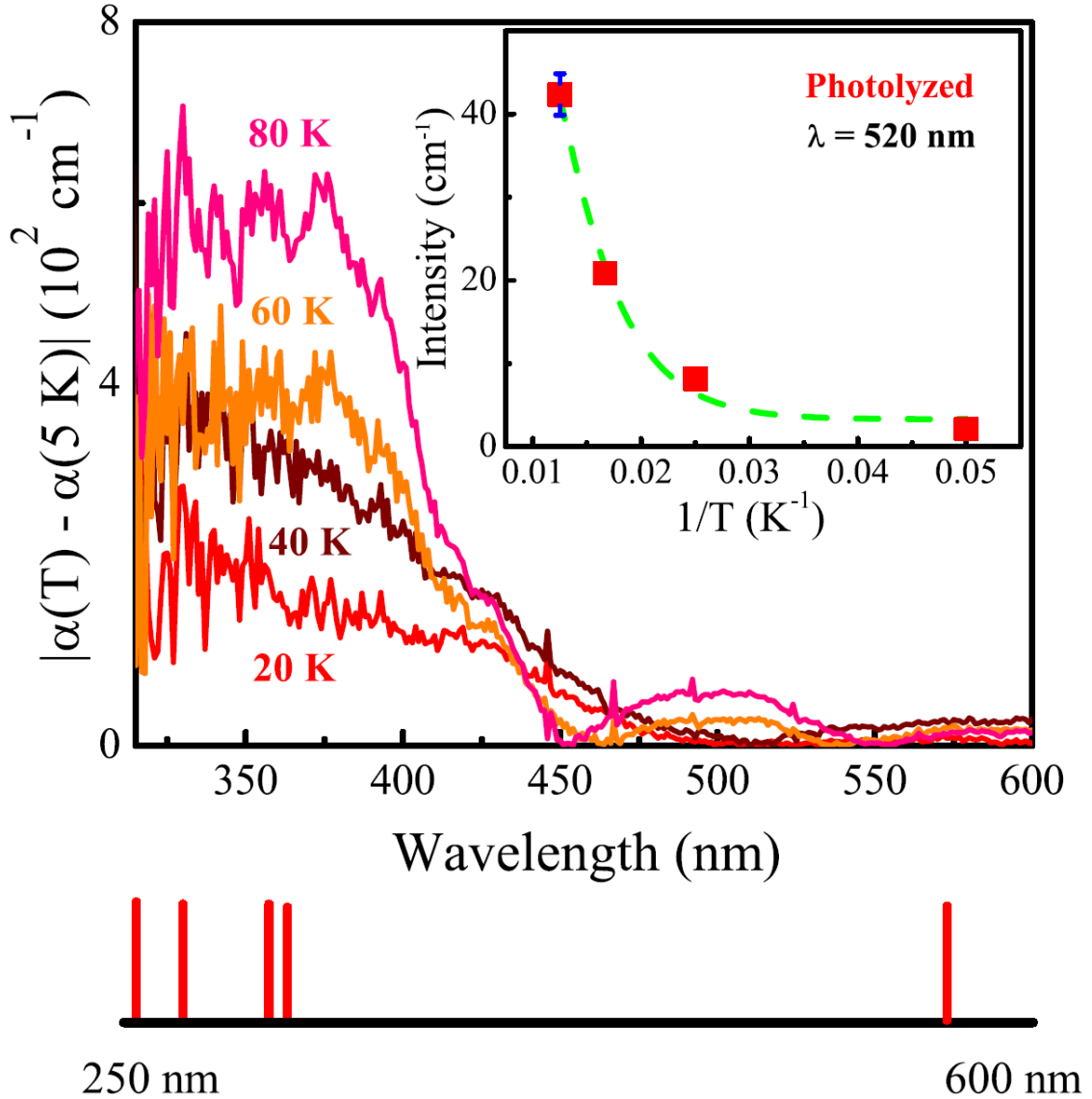


Figure 5.8: Absolute value of the absorption difference, $|\Delta\alpha| = |\alpha(T)| - |\alpha(T = 5K)|$, vs. wavelength for the photolyzed biradical film at 80, 60, 40, and 20 K. Inset: Example Curie [34] fit at 520 nm. These data allow a direct comparison of electron paramagnetic resonance and optical methods of spin gap determination. The determined $\theta = 230 \pm 22K$, which compares well with that from electron spin resonance (288 K). A schematic view of the calculated triplet state excitations using the TDDFT method (shown at the bottom) in reasonable agreement with the $|\Delta\alpha|$ data in the main panel. The fine structure in the absorption difference spectrum is discussed in the supplementary material

From Fig. 5.6, we see that the singlet and triplet state spectra of 1,4-phenylenedinitrene are predicted to be quite different. The selected-CI results indicate that in the singlet spectrum $\pi \rightarrow \pi^*$ excitations acquire significant intensity through simultaneous excitation of $b_{1g} \rightarrow b_{3u}$, whereas the triplet spectrum is dominated by single excitations. At the lowest temperature, the excitations are essentially those assigned to the singlet ground state, with weaker features of triplet origin growing at higher temperatures Fig. (5.8).

The TDDFT spectrum of 4,4'-stilbenedinitrene is very similar to that of 1,4-phenylenedinitrene. The singlet and triplet spectrum are dominated by $\pi \rightarrow \pi^*$ excitations as well as excitations from the ag and bu MOs. The most intense peak on the singlet spectrum occurs at 223 nm ($N \rightarrow \sigma^*$, $\mu^2 = 1.61$), whereas the triplet spectrum is dominated by one very intense peak occurring at 364 nm (with equal contributions from $N \rightarrow N^*$ and $\pi \rightarrow \pi^*$, $\mu^2 = 10.55$). The dipole-allowed spectrum of the triplet species is more intense and at higher energy than that of the singlet, the features in common between the singlet and triplet spectra are primarily $\pi \rightarrow \pi^*$, and many of the lower energy features are either of low intensity or dipole forbidden.

5.3.4 Structure Property Relationship

Spin splitting has been shown to reduce (Section 5.3.2) with the addition of spacer groups between the spin carrying atoms. Using a two state problem coupled with the molecular properties Fig. 5.9, we provide physical insight to features and trends observed in the spectrum and the electronic structures.

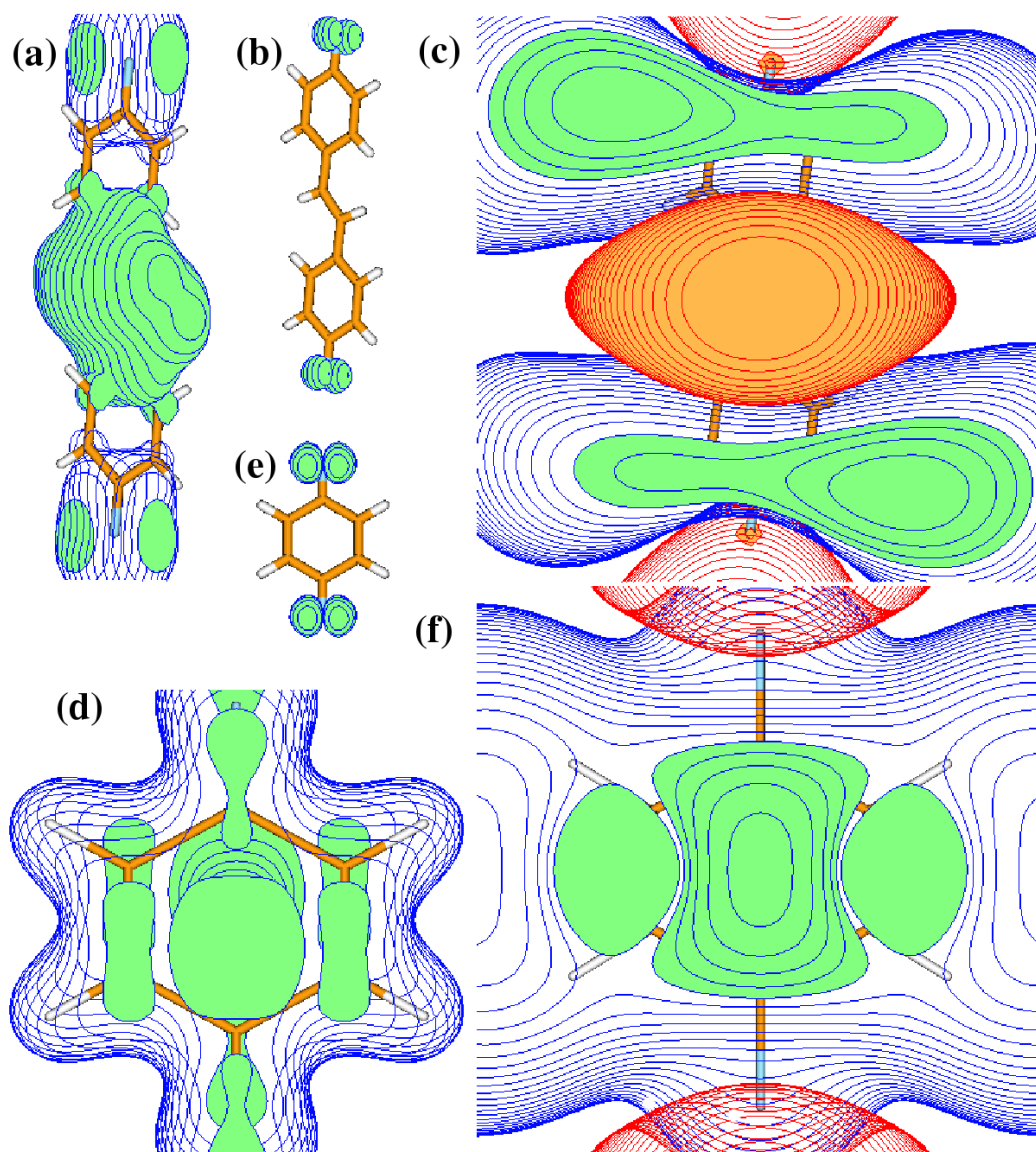


Figure 5.9: Molecular properties of 4,4'-stilbenedinitrene (**a**, **b**, **c**) and 1,4-phenylenedinitrene (**d**, **e**, **f**) (**a**) Electronic charge density distribution (contour spacing = 0.01) (**b**) Spin density distribution (contour spacing = 0.02) (**c**)Molecular electrostatic potential(contour spacing = 0.05) (**d**)Electronic charge density distribution (contour spacing = 0.05) (**e**) Spin density distribution (contour spacing = 0.01) and (**f**) Molecular electrostatic potential(contour spacing = 0.01). The electronic charge density of 1,4-phenylenedinitrene is uniformly distributed over the entire molecule whereas the bulk of the electronic charge density in 4,4'-stilbenedinitrene is accumulated over the spacer groups, between the nitrogen atoms. Spin density distribution is localized on the nitrogen atoms in both structures. In (c) and (f) the blue and red contours represent the positive and negative potentials respectively.

We will consider the singly occupied molecular orbitals (SOMO), of the active space Fig. 5.4, of 1,4-phenylenedinitrene and simplify the bi-radical into two equivalent atomic orbitals, a and b, localized on the nitrogen atoms (Fig. 5.9e). The b_{1g} and b_{3u} SOMO are the symmetric and anti-symmetric combinations respectively. The various configuration state function are obtained by putting the two electrons into the orbitals (Table 5.7.) To simplify the expressions and avoid repeating the irreducible representation each time, we simply define

Table 5.7: Configuration state functions (ψ_I). I is the state function index, $\hat{\mathbf{H}}$ is the Hamiltonian, $\langle S^2 \rangle$ is the electron spin expectation value and n_1 and n_2 are the occupation numbers of the orbitals.

I	n_1	n_2	Symm.	$\langle S^2 \rangle$	$H_{II} = \langle \psi_I \hat{\mathbf{H}} \psi_I \rangle$
1	2	0	1A_g	0	$2h_{11} + \langle 11 11 \rangle$
2	1	1	${}^3B_{2u}$	1	$h_{11} + h_{22} + \langle 11 22 \rangle - \langle 12 12 \rangle$
3	1	1	${}^1B_{2u}$	0	$h_{11} + h_{22} + \langle 11 22 \rangle + \langle 12 12 \rangle$
4	2	0	1A_g	0	$2h_{11} + \langle 22 22 \rangle$

$$\begin{aligned}\phi_1 = \phi_{b_{1g}} &= \frac{1}{\sqrt{2}}(a + b) \\ \phi_1 = \phi_{b_{3u}} &= \frac{1}{\sqrt{2}}(a - b)\end{aligned}\tag{5.5}$$

The only non-zero off-diagonal matrix element between the two 1A_g states is

$$\langle \psi_1 | \hat{\mathbf{H}} | \psi_2 \rangle = \langle 11 | 22 \rangle - \langle 12 | 12 \rangle\tag{5.6}$$

In order to get a better interpretation of the states interaction and correlate it to the electronic structure of the system, we revert to the atomic orbital basis and set some definitions as well as integrals (making use of the symmetry between a and b)

$$\begin{aligned}h_{aa} &= h_{bb} = h \\ h_{ab} &= -\nu\end{aligned}\tag{5.7}$$

The one- electron integrals are simplified as follows:

$$\begin{aligned}h_{11} &= h - \nu \\ h_{22} &= h + \nu \\ h_{12} &= 0\end{aligned}\tag{5.8}$$

The two-electron integrals are simplified as follows:

$$\begin{aligned}
\langle 11|11\rangle &= \frac{1}{2}(\langle aa|aa\rangle + \langle aa|bb\rangle) + \langle ab|ab\rangle + 2\langle aa|ab\rangle & (5.9) \\
\langle 22|22\rangle &= \frac{1}{2}(\langle aa|aa\rangle + \langle aa|bb\rangle) + \langle ab|ab\rangle - 2\langle aa|ab\rangle \\
\langle 11|22\rangle &= \frac{1}{2}(\langle aa|aa\rangle + \langle aa|bb\rangle) - \langle ab|ab\rangle \\
\langle 12|12\rangle &= \frac{1}{2}(\langle aa|aa\rangle - \langle aa|bb\rangle) \\
\langle 11|22\rangle + \langle 12|12\rangle &= \langle aa|aa\rangle - \langle ab|ab\rangle \\
\langle 11|22\rangle - \langle 12|12\rangle &= \langle aa|bb\rangle - \langle ab|ab\rangle
\end{aligned}$$

The singly occupied molecular orbitals in both 1,4-phenylenedinitrene and 4,4'-stilbenedinitrene are solely Nitrogen p_x atomic functions; With the two atomic functions, a and b, at $y = -Y$ and $y = +Y$ respectively, a probable transition dipole moment is (assuming $\langle a|y+Y|a\rangle = 0$ and similarly for b, which is true if they are pure atomic orbitals).

$$\langle 1|y|2\rangle = \frac{1}{2}(\langle a|y|a\rangle - \langle b|y|b\rangle) = -Y \quad (5.10)$$

Thus the further apart the Nitrogen centers are, the more intense the features. Table 5.8 and Table 5.9 illustrates the relationship between transitions and the electronic structure of 4,4'-stilbenedinitrene (singlet and triplet respectively). The intensities of the features are further enhanced when mixing occurs between the $N \rightarrow N^*$ and the $\pi \rightarrow \pi^*$ transitions. The features at (364nm, 10.55a.u) on the TDDFT spectrum of triplet 4,4'-stilbenedinitrene (Fig. 5.7) and at (251nm, 11.8a.u) on the selected-CI spectrum of 1,4-phenylenedinitrene (Fig. 5.6) are very intense, consequence of the $N \rightarrow N^*$ and the $\pi \rightarrow \pi^*$ transition mixing.

Table 5.8: Transition dipole moments (X, Y) of singlet 4,4'-stilbenedinitrene for selected transitions, at computed wavelength (λ) with the squared dipole oscillator strength (μ^2 , in atomic units)

Transitions	(X, Y)	μ^2 (a.u)	λ (nm)
$N \rightarrow \pi^*$	0.043, -1.30	0.0026	1008
$N \rightarrow N^*$	0.103, -0.9663	0.0094	295
$N \rightarrow N^*$	-0.196, -0.251	0.000099	309
$N \rightarrow \sigma^*$	0.227, -0.0163	0.000033	275
$N \rightarrow \sigma^*$	0.398, 0.0389	0.00035	257
$\sigma \rightarrow N^*$	-0.0458, 0.8148	0.0079	228
$N \rightarrow \sigma^*$	0.1488, -3.046	1.61	223

Table 5.9: Transition dipole moments (X, Y) of triplet 4,4'-stilbenedinitrene for selected transitions, at computed wavelength (λ) with the squared dipole oscillator strength (μ^2 , in atomic units)

Transitions	(X, Y)	μ^2 (a.u)	λ (nm)
$\pi \rightarrow \pi^* + N \rightarrow N^*$	-0.105, 6.24	10.55	364
$\pi \rightarrow N^*$	-0.229, -0.884	0.000035	315
$N \rightarrow \pi^*$	-0.034, -0.279	0.000061	309
$N \rightarrow \sigma^*$	-0.0342, 0.0516	0.000000	245

The integrals (Eq. 5.9) can be further simplified by assuming that the atomic orbitals do not overlap (This does not mean that $h_{ab} = -\nu = 0$, since this is an effective one-particle interaction that can be carried out through space via other orbitals). The integrals then become

$$\begin{aligned}
\langle 11|11\rangle = \langle 22|22\rangle &= \langle 11|22\rangle = \frac{1}{2}(\langle aa|aa\rangle + \langle aa|bb\rangle) & (5.11) \\
\langle 12|12\rangle &= \frac{1}{2}(\langle aa|aa\rangle - \langle aa|bb\rangle) \\
\langle 11|22\rangle + \langle 12|12\rangle &= \langle aa|aa\rangle \\
\langle 11|22\rangle - \langle 12|12\rangle &= \langle aa|bb\rangle \\
\epsilon_1 &= h - \nu + \langle aa|bb\rangle \\
\epsilon_2 &= h + \nu + \langle aa|bb\rangle
\end{aligned}$$

Table 5.10: Non-zero matrix elements, from integral simplification, of the Hartree-Fock equation. We observe that $\langle aa|aa\rangle > \langle aa|bb\rangle > 0$

Label	Terms
H_{11}	$2h - 2\nu + \frac{1}{2}(\langle aa aa\rangle + \langle aa bb\rangle)$
H_{22}	$2h + \langle aa bb\rangle$
H_{33}	$2h + \langle aa aa\rangle$
H_{44}	$2h + 2\nu + \frac{1}{2}(\langle aa aa\rangle + \langle aa bb\rangle)$
H_{14}	$\langle aa bb\rangle$

The non-zero matrix elements (outcome of integral simplifications) of the Hartree-Fock equation is then represented in Table 5.10.

The eigenvalues of the state functions can then be obtain. First we establish the following relationships:

$$\begin{aligned}\frac{1}{2}(\epsilon_2 - \epsilon_1) &= \nu \\ \frac{1}{2}(\epsilon_2 - \epsilon_1) &= h + \langle aa|bb \rangle\end{aligned}\tag{5.12}$$

The eigenvalues of the 1A_g state functions are:

$$\begin{aligned}E_1 &= 2h + \frac{1}{2}(\langle aa|aa \rangle + \langle aa|bb \rangle) - \sqrt{4\nu^2 + (\langle aa|bb \rangle)^2} \\ E_4 &= 2h + \frac{1}{2}(\langle aa|aa \rangle + \langle aa|bb \rangle) + \sqrt{4\nu^2 + (\langle aa|bb \rangle)^2}\end{aligned}\tag{5.13}$$

Empirically, ν is small (0.0012) whereas $\langle aa|bb \rangle = O(Y^{-1})$. It is thus save to make the approximation that $\langle aa|bb \rangle \gg |\nu|$ and Taylor expand the square root about $\nu = 0$. Eq. 5.13 then reduces to

$$\begin{aligned}E_1 &= 2h + \frac{1}{2}(\langle aa|aa \rangle + \langle aa|bb \rangle) + O(Y^{-1}) \\ E_4 &= 2h + \frac{1}{2}(\langle aa|aa \rangle + \langle aa|bb \rangle) + O(Y^{-1})\end{aligned}\tag{5.14}$$

The eigenvalues of the $^1B_{2u}$ and the $^3B_{2u}$ state functions are:

$$\begin{aligned}E_3 &= 2h + \langle aa|aa \rangle \\ E_2 &= 2h + \langle aa|bb \rangle\end{aligned}\tag{5.15}$$

The spin splitting and the vertical electronic transition can now be expressed in atomic orbital basis. The singlet-triplet splitting is written as

$$E_2 - E_1 = \frac{1}{2}(3\langle aa|bb \rangle - \langle aa|aa \rangle)\tag{5.16}$$

and the ${}^1A_g \rightarrow {}^1B_{2u}$ transition energy is

$$E_3 - E_1 = \frac{1}{2}(\langle aa|aa \rangle - \langle aa|bb \rangle) \quad (5.17)$$

Since $\langle aa|bb \rangle = O(Y^{-1})$ whereas $\langle aa|aa \rangle$ is constant, making the molecule longer should stabilize the triplet because for these molecules, the states are essentially degenerate. This predicts that adding, for instance, more ring spacer should make the triplet the ground state, giving rise to isolated radicals (double doublets). In reality, the through-molecule Coulomb interaction will be screened (through correlation effects) by the intervening ring, and the atomic states, a and b, are readily mixed with the ring sigma framework. The through-molecule Coulomb interaction is also screened by the accumulated electronic charge density Fig. 5.9(a) over the spacer group in 4,4'-stilbenedinitrene which is well illustrated by the negative electrostatic potential Fig. 5.9(c) with red contour lines between the nitrogen atoms on which the spins are localized Fig. 5.9(b)

The through-molecule coulomb interaction term contributes to the energy of both the 1A_g and the ${}^3B_{2u}$ states such that additional ring spacers will lower the energy of the 1A_g states and at the same time, the energy of the ${}^3B_{2u}$ states is also changed but the change is quantitatively less than it is for the triplet state (The singlet-triplet splitting of 1,4-phenylenedinitrene is 354K whereas that of 4,4'-stilbenedinitrene is 35K.). As more ring spacers are added, the singlet-triplet splitting is expected to reduce, and constitutes a measure of the bi-radical character.

The fact that the $\langle aa|aa \rangle$ term is constant results in the energy of the ${}^1B_{2u}$ not being affected by the addition of ring-spacer. Given that the energy of the 1A_g states change with additional ring-spacers, the intensity of the ${}^1A_g \rightarrow {}^1B_{2u}$ is quantitatively affected (The singlet spectrum of 4,4'-stilbenedinitrene is less intense than that of 1,4-phenylenedinitrene). The vibrational modes (Table 5.11) have shown high amplitude ring stretching which may also be a factor in enhancing the bi-radical character.

Table 5.11: Vibrational fine structure extracted from the absorption difference data of the 1,4-phenylenedinitrene biradical (supporting material of [34]) compared with B_u symmetry mode frequencies and assignments from MCSCF-CASSCF (10, 10)/ 6-311G* calculations. The calculated frequencies correspond to the singlet state. Those of the triplet state were not much different.

Obs. (cm^{-1})	Calc. (cm^{-1})	Displacement patterns
1633, 1630, 1608	1612	C-C asym. stretch on ring + C-H wag
1494, 1436, 1421	1349, 1391	Asym. C-C stretch in ring + C-H scissoring
1208, 1182, 1150	1180	Sym. C1-C ring stretch + assym. C-H bend
921	908	C1-C4 bend in ring (oop) + C-H bend
896	837	C-H bend (oop)
708, 712	748	Out-of-plane ring bending centered on C1
400	393	CN wagging (in-plane) scissor + CN bend (oop)
312, 285	291	CN wagging (oop)

5.4 Conclusion

We have investigated the role played by both triplet and singlet electronic structures of 1,4-phenylenedinitrene and 4,4'-stilbenedinitrene in tuning the singlet-triplet equilibrium. The red-shift (observed in experiment) of both singlet spectra with respect to the triplet spectra in both targeted systems was confirmed by *ab initio* calculations. Furthermore other spectral features such as the high intensity of the triplet spectrum at higher temperatures and the low intensities of the singlet spectrum at lower temperatures (no triplet features at lower temperatures) were confirmed.

The importance of Coulombic interaction through spin exchange has been illustrated. The spin splitting is inversely proportional to the separation between the spin carrying centers. The mixing of the transitions from spin carrying centers with $\pi \rightarrow \pi^*$ transitions, significantly enhances the transition. The vibrational modes have shown high amplitude ring stretching which may also be a factor in enhancing the bi-radical character (defined by the size of the separation between the spin carrying centers).

Chapter 6

Conclusions

Two solvation models with different molecular cavities have been designed, implemented, and tested in MADNESS [70]. We have designed, implemented and have applied geometric topology to study environmental and confinement effects of solvation on a physisorbed molecule. In collaboration with experimentalist we have investigated, for the first time, the tunability of singlet-triplet equilibrium using a high magnetic field in organic biradical materials.

The surface volume polarizable electrostatic (SVPE) solvation model that we have developed, not only captures surface polarization as is the case with the polarizable continuum model [39, 40, 41, 42, 43, 44, 45, 46, 47, 48, 49, 50, 51], but also captures,efficiently, volume polarization. The surface and volume polarization contributions are computed simultaneously (this reduces roundoff errors and the cost of computation), unlike other SVPE models [52, 53, 56, 57, 58] where the surface and volume pieces are often computed separately. The dielectric function (Eq. 3.16) has been developed to efficiently handle discontinuity. The Heaviside step function (Eq. 3.6) is used to smoothly switch between the inside and the outside of the molecular cavity. The improved dielectric function expression is derived using the log-derivative as shown in Eq. 4.39; this form of discontinuous dielectric function, assures that the charge distribution is always localized exactly on the surface

of the molecular cavity, and this leads to a much improved numerical behavior and more rapid convergence to the limit $\sigma = 0$. Selected molecular systems have been used to illustrate surface and volume polarization. Free energy of solvation (contributions from the cavitation and the electrostatic solvation free energies) agrees favorably well with the experimental values (Table 3.3).

Contrary to the cavity of the interlocking sphere used to describe the SVPE model, the dielectric function of the isodensity model is a functional of the electronic charge density (of the molecular system) Eq. 3.14. Just as in the interlocking sphere model where the switching function is used to switch smoothly between the inside and outside of the molecular cavity, a similar parameter exists here to allow for a smooth decay of the dielectric function in the proximity of the solute-solvent boundary. The dielectric functional is accurately computed and represented without having to augment the electronic density with some Gaussian function as is the case in [?]. The isodensity solvation model has been revised to overcome the challenges encountered in the previous developments [114, 55]: a new mesh function with much improved numerical behavior, refined approach to computing the molecular quantum surface area and quantum volume. The overall performance of the methodology over the free energies in water on a selected set of molecules compares favorably with the experimental results, other theoretical methods of similar physical background and the parameter intensive methods as well.

In this work, we have revised the SVPE and the isodensity solvation models wherein, both the solute and the solvent environment are represented with the same adaptive, multi-wavelet basis functions, thereby, within the user-specified precision, eliminating the basis set error and greatly simplifying their implementations. We have reformulated both methods to use integral equations throughout as well as a conscious management of the numerical properties of the basis.

Using the geometric topologies developed for the solvation models, we have designed, implemented and tested the polarizable continuum colloid. We have used the spherical polarizable continuum colloid to study the environmental effects of

solvation on a molecule physisorbed on a metal particle. The numerical differentiation of the dipole to compute the polarizability and higher order moments of molecules provides results with sufficient numerical accuracy (Table 4.3, and Table 4.2). On the other hand, numerical differentiation of energy does not provide results with numerical accuracy (Table 4.4). We have used the polarizability of molecules to analyze environmental effects on physisorbed molecules.

We have shown that the electrostatic interaction between molecules and the polarizable continuum colloid (PCC) results in a magnified reflected electric field (Table 4.6 and Table 4.7). The magnitude of the reflected electric field depends on the PCC-molecule separation. A similar magnification effect has been shown for the reflected field from the PCC-field (external electric field) interaction: a PCC-pyridine separation of 2.0 \AA , gives rise to a reflected electric field that is four times the magnitude of the incident electric field. The presence of the solvent, reduces the PCC-molecule interaction as well as the enhancement of the reflected electric field (Table 4.8 and Table 4.9)

Confinement effects have been observed through the change in the mean polarizability of the solvated, physisorbed and solvated-physisorbed molecules: the mean polarizability of the solvated pyridine and solvated methane are respectively $46.92a.u^3$ and $12.60a.u^3$, and are equal in magnitude to the polarizabilities of the solvated-physisorbed pyridine or methane at any given PCC-molecule separation (Table 4.8 and Table 4.9). The mean polarizability of free methane and pyridine are respectively $61.30a.u^3$ and $15.84a.u^3$. We have illustrated the enhancement of the effective polarizabilities through the environmental effects. The effective polarizability of the physisorbed molecules in vacuum is greater than that of the solvated-physisorbed molecules which in turn is greater than that of the solvated molecules.

Through our calculations, we have confirmed the observations made (by experimentalist) about the possibility to use high magnetic field to manipulate the singlet-triplet equilibrium in biradical organic compounds [34], which is a departure from the traditional electron paramagnetic resonance-based (EPR) Curie law methods for

determining the spin gap of a reactive biradical. This new approach provides a more efficient way of determining the spin gap in open shell systems (Table 5.6)

The role played by both triplet and singlet electronic structures of 1,4-phenylenedinitrene and 4,4'-stilbenedinitrene in tuning the singlet-triplet equilibrium has been investigated. The red-shift (observed in the experiment) of both singlet spectra with respect to the triplet spectra in both targeted systems was confirmed by *ab initio* calculations (Fig. 5.6 and Fig. 5.7). Furthermore, other spectral features such as the high intensity of the triplet spectrum at higher temperatures and the low intensities of the singlet spectrum at lower temperatures (no triplet features at lower temperatures) were confirmed.

The importance of Coulombic interaction through spin exchange has been illustrated. The spin splitting is inversely proportional to the separation between the spin carrying centers. The mixing of the transitions from spin carrying centers with $\pi \rightarrow \pi^*$ transitions, significantly enhances the transition. The vibrational modes have shown high amplitude ring stretching which may also be a factor in enhancing the bi-radical character (defined by the size of the separation between the spin carrying centers).

Bibliography

- [1] J. D. Jackson, *Classical Electrodynamics*, 1975, 2nd edition, pp.143–162 [2](#)
- [2] D. J. Maxwell, S. R. Emory, S. Nie, *Chem. Mater.*, 2001, 13, 1082 [6](#)
- [3] D. L. Jeanmaire, R. P. Van Duyne, *J. Electroanal. Chem.*, 1977, 84, 1 [5](#)
- [4] F. W. King, R. P. Van Duyne, and G. C. Schatz, *J. Chem. Phys.*, 1978, 69, 4472 [6](#)
- [5] Hohenberg and W. Kohn, *Phys. Rev.*, 1964, 136, B864 [17](#)
- [6] J. T. Krug, G. D. Wang, S. R. Emory, S. Nie, *J. Am. Chem. Soc.*, 1999, 121, 9208 [6](#)
- [7] K. Kneipp, H. Kneipp, I. Itzkan, R. R. Dasari, M. S. Feld, *Chem. Phys.*, 1999, 247, 155 [6](#)
- [8] K. Kneipp, H. Kneipp, R. Manoharan, E. B. Hanlon, I. Itzkan, R. R. Dasari, M. S. Feld, *Appl. Spectrosc.*, 1998 52, 1493 [6](#)
- [9] K. Kneipp, H. Kneipp, R. Manoharan, I. Itzkan, R. R. Dasari, M. S. Feld, *Raman Spectrosc.*, 1998, 29, 743 [6](#)
- [10] K. Kneipp, H. Kneipp, V. B. Kartha, R. Manoharan, G. Deinum, E. B. Hanlon, I. Itzkan, R. R. Dasari, M. S. Feld, *Phys. Rev. E*, 1998, 57,R6281 [6](#)
- [11] K. Kneipp, Y. Wang, H. Kneipp, I. Itzkan, R. R. Dasari, M. S. Feld, *Phys. Rev. Lett.*, 1996, 76, 2444 [6](#)
- [12] K. Kneipp, Y. Wang, H. Kneipp, L. T. Perelman, I. Itzkan, R. R. Dasari, M. S. Feld, *Phys. Rev. Lett.*, 1997, 78, 1667 [6](#)
- [13] W. Kohn and L. J. Sham, *Phys. Rev.*, 1965, 140, A1133 [17](#)
- [14] Lee P. C., Meisel, D., *J. Phys. Chem.*, 1982, 86, 3391 [7](#)

- [15] M. Fleischman, P. J. Hendra, A. J. McQuillan, *Chem. Phys. Lett.*, 1974, 26, 123
5
- [16] M. G. Albrecht, J. A. Creighton, *J. Am. Chem. Soc.*, 1974, 99, 5215 5
- [17] W. C. Meixer and P. R. Antoniewicz, *Phys. Rev. B*, 1976, 13, 3276 6
- [18] S. Corni and J. Tomasi, *Chem. Phys. Letters*, 2001, 342, 135 6
- [19] M. Moskovits, *J. Chem. Phys.*, 1978, 69, 4159 6
- [20] S. Nie, S. R. Emory, *Science*, 1997, 275, 1102 6
- [21] S. R. Emory, W. E. Haskins, S. Nie, *J. Am. Chem. Soc.*, 1998, 120, 8009 6
- [22] Tan S., Erol M. Attygalle, Du H., Sukhishvili S., *Langmuir*, 2007, 23, 9836 7
- [23] W. A. Lyon, S. Nie, *Anal. Chem.*, 1997, 69, 3400 6
- [24] W. E. Doering, S. Nie, *J. Phys. Chem.*, 2002, 106, 3115 6
- [25] Wilson, T. J. *Am. Chem. Soc.*, 1966, 88, 2898 12
- [26] Gordy W., *Theory and Applications of ESR*, Wiley; New York, 1980 12
- [27] N. P. Grilsan, Zhendong Zhu, C. M. Hadad, and M. S. Platz, *J. Am. Chem. Soc.*,
1999, 121, 1202 13
- [28] Horner and Christman, *Angew Chimie (int. ed)* 1963, 2, 599 13
- [29] Abramovitch and Davis, *Chem. Rev.*, 1964, 64, 149 13
- [30] T. Ohana, A. Ouchi, H. Morigama and A. Yabe, *J. Photochem. Photobiol. A:
Chem.*, 1993, 72, 83 13
- [31] Reiser and Fraser, *Nature*, 1965, 208,682 13
- [32] A. Reiser, G. Bowes and R. J. Horne, *Trans. Faraday Soc.*, 1966, 62, 3162 13,
112

- [33] A. Reiser, H. M. Wagner, R. Marley, and G. Bowes and R. J. Horne, *Trans. Faraday Soc.*, 1967, 63, 2403 [13](#)
- [34] Ö. Günaydn-Sen, J. Fosso-Tande, P. Chen, J. L. White, T. L. Allen, J. Cherian, T. Tokumoto, P. M. Lahti, S. McGill, R. J. Harrison, and J. L. Musfeldt, *J. Chem. Phys.*, 2011, 135, 241101 [xiv](#), [xx](#), [13](#), [98](#), [111](#), [115](#), [125](#), [129](#)
- [35] Minato, M.; Lahti, P. M. *J. Phys. Org. Chem.* 1993, 6, 483. [13](#), [14](#)
- [36] M. Minato and Paul M. Lahti, *J. Am. Chem. Soc.* 1997, 119, 2187 [14](#)
- [37] Rikhia G., Prasenjit S., and Swapan C., *J. Phys. Chem. A* 2010, 114, 93 [14](#)
- [38] Henchman R. H. and Essex J. W., *J. Comput. Chem.*, 1999, 20, 499 [8](#)
- [39] S. Miertus, E. Scrocco, and J. Tomasi, *Chem. Phys.*, 1981, 55. 117 [9](#), [127](#)
- [40] A. A. Rashin and K. Namboodiri, *J. Phys. Chem.* 1987, 91. 6003 [9](#), [127](#)
- [41] H. Hoshi, M. Sakurai, Y. Inoue, and R. Chûjô, *J. Chem. Phys.*, 1987, 87. 1107 [9](#), [127](#)
- [42] R. J. Zauhar and R. S. Morgan, *J. Comput. Chem.*, 1988, 9. 171 [9](#), [127](#)
- [43] J. Tomasi, R. Bonaccorsi, R. Cammi, and F. J. Olivares del Valle, *J. Mol. Struct.: THEOCHEM* , 1991, 234. 401 [9](#), [127](#)
- [44] G. E. Chudinov, D. V. Napolov, and M. V. Basilevsky, *Chem. Phys.*, 1992, 160. 41 [9](#), [127](#)
- [45] Y. N. Vorobjev, J. A. Grant, and H. A. Scheraga, *J. Am. Chem. Soc.*, 1992, 114. 3189 [9](#), [127](#)
- [46] G. Rauhut, T. Clark, and T. Steinke, *J. Am. Chem. Soc.*, 1993, 115. 9174 [9](#), [127](#)
- [47] F. J. Luque, M. J. Negre, and M. Orozco, *J. Phys. Chem.*, 1993, 97. 4386 [9](#), [127](#)

- [48] R. Bharadwaj, A. Windemuth, S. Sridharan, B. Honig, and A. Nicholls, *J. Comput. Chem.*, 1995, 16. 898 [9](#), [127](#)
- [49] G. A. Tawa, R. L. Martin, L. R. Pratt, and T. V. Russo, *J. Phys. Chem.*, 1996, 100. 1515 [9](#), [127](#)
- [50] J. B. Foresman, T. A. Keith, K. B. Wiberg, J. Snoonian, and M. J. Frisch, *J. Phys. Chem.*, 1996, 100. 16098 [9](#), [127](#)
- [51] N. Rega, M. Cossi, and V. Barone, *Chem. Phys. Lett.*, 1998, 293. 221 [9](#), [127](#)
- [52] D. M. Chipman, *J. Chem. Phys.*, 1996, 104. 3276 [9](#), [127](#)
- [53] D. M. Chipman, *J. Chem. Phys.*, 1997, 106, 10194 [9](#), [127](#)
- [54] Robert J. Harrison, *J Comput Chem*, 2004, 25, 328 [41](#)
- [55] J. Dziedzic, H. H. Helal, C.-K. Skylaris, A. A. Mostofi and M. C. Payne, *EPL*, 2011, 95,43001 [46](#), [128](#)
- [56] C.-G. Zhan, J. Bentley, and D. M. Chipman, *J. Chem. Phys.*, 1998, 108. 177 [9](#), [127](#)
- [57] C.-G. Zhan, D. W. Landry, and R. L. Ornstein, *J. Am. Chem. Soc.*, 2000, 122. 2621 [9](#), [127](#)
- [58] D. M. Chipman, *J. Chem. Phys.*, 2004, 120. 5566 [9](#), [127](#)
- [59] J. Tomasi and Maurizio Persico, *Chem. Rev.*, 1994, 94, 2027 [8](#)
- [60] T. Ziegler, A. Rauk, E. J. Baerends, *Theoret. Chim. Acta*, 1977, 43, 261 [19](#)
- [61] U. Von Barth, *Phys. Rev. A*, 1979, 20, 1693 [19](#)
- [62] C. Daul, *Int. J. Quantum Chem.*, 1994, 52, 867 [19](#)
- [63] R. M. Dickson, T. Ziegler, *Int. J. Quantum Chem.*, 1996, 58, 681 [19](#)

- [64] S. J. A. Van Gisbergen, J. G. Snijders, E. J. Baerends, *J. Chem. Phys.*, 1995, 103, 9347 [19](#), [20](#)
- [65] Ch. Jamorski, M. E. Casida, D. R. Salahub, *J. Chem. Phys.*, 1996, 104, 5134 [20](#)
- [66] E. K. U. Gross, W. Kohn, *Adv. Quantum Chem.*, 1990, 21, 255 [20](#)
- [67] S. P. Karna, M. Dupuis, *J. Comput. Chem.*, 1991, 12, 487 [20](#)
- [68] J. C. Slater, *Phys. Rev.*, 1930, 36, 57 [22](#)
- [69] S. F. Boys, *Proc. R. Soc. (London) A*, 1950, 200, 542 [22](#)
- [70] <http://code.google.com/p/m-a-d-n-e-s-s/> [23](#), [127](#)
- [71] G. Beylkin and J. M. Keiser, *J. Comput. Phys.*, 1997, 132, 233 [24](#)
- [72] R. J. Harrison, G. I. Fann, Takeshi Yanai, and Zhengting Gan, G. Beylkin, *J. Chem. Phys.*, 2004, 121, 11587 [24](#)
- [73] J. Tomasi and M. Persico, *Chem. Rev. Washington, D.C.*, 1994, 94, 2027 [47](#)
- [74] H. Reiss, H. L. Frisch, and J. L. Lebowitz, *J. Chem. Phys.*, 1959, 31, 369 [47](#)
- [75] H. Reiss, H. L. Frisch, E. Helfand, and J. L. Lebowitz, *J. Chem. Phys.*, 1960, 32, 119 [47](#)
- [76] P. Claverie, in *Intermolecular Interactions: from Diatomics to Biomolecules*, (Wiley, Chichester, 1978) edited by B. Pullman [47](#)
- [77] P. Claverie, J. P. Daudey, J. Langlet, B. Pullman, D. Piazzola, and M. J. Huron, *J. Phys. Chem.*, 1978, 82, 405 [47](#)
- [78] J. Langlet, P. Claverie, J. Caillet, and A. Pullman, *J. Phys. Chem.*, 1988, 92, 1617 [47](#)
- [79] M. Heying and D. S. Corti, *J. Phys. Chem. B*, 2004, 108, 19756 [47](#)

- [80] C. Benzi, M. Cossi, R. Imbrota, and V. Barone, *J. Comput. Chem.*, 2005, 26, 1096
47
- [81] J. Tomasi, B. Mennucci, and R. Cammi, *Chem. Rev. (Washington, D.C.)*, 2005,
105, 2999 47, 54, 73
- [82] H. H. Uhlig, *J. Phys. Chem.*, 1937, 41, 1215 48
- [83] O. Sinanolu, *J. Chem. Phys.*, 1981, 75, 463 48
- [84] I. Tuñón, E. Silla, and J. L. Pascual-Ahuir, *Chem. Phys. Lett.*, 1993, 203, 289 48
- [85] R. C. Tolman, *J. Chem. Phys.*, 1949, 17, 333 48
- [86] D. M. Huang, P. L. Geissler, and D. Chandler, *J. Phys. Chem. B*, 2001, 105, 6704
48
- [87] F. M. Floris, M. Selmi, A. Tani, and J. Tomasi, *J. Chem. Phys.*, 1997, 107, 6353
48
- [88] M. Cococcioni, F. Mauri, G. Ceder, and N. Marzari, *Phys. Rev. Lett.*, 2005,
94, 145501 48
- [89] Li-Dong Gong, Zhong-Zhi Yang, *J. Comput. Chem.*, 2009, 31, 2098 50
- [90] Walker, P. D., Mezey, P. G., *J. Am. Chem. Soc.*, 1993, 115, 12423 50
- [91] Greer J., Bush B. L. *Proc. Natl. Acad. Sci. USA*, 1978, 75, 303 50
- [92] Petitjean M., *J. Comput Chem.*, 1994, 15, 507 50
- [93] Derek A. Long, *The Raman Effect- A Unified Treatment of the Theory of Raman
Scattering by Molecules-*, John Wiley and Sons LTD, (2002) 60
- [94] H. Sekino and R. J. Bartlett, *J. Chem. Phys.*, 1986, 84, 2726 xi, 86

- [95] E. Perrin, P. N. Prasad, P. Mougnot and M. Dupuis, *J.Chem. Phys.*,1989, 91, 4728 [86](#)
- [96] J. R. Hammond, N. Govind, K. Kowalski, J. Autschbach and S. S. Xantheas *J.Chem. Phys.*,2009, 131, 214103 [86](#)
- [97] D. A. Scherlis, J.-L. Fatterbert, F. Gygi, M. Cococcioni, N. Marzari, *J. Chem. Phys.*,2006, 124, 74103 [31](#), [45](#), [48](#), [56](#), [58](#)
- [98] A. J. Ben-Naim, *J. Phys. Chem.*,1978, 82, 792 [47](#), [53](#)
- [99] D. M. Chipman, *J. Chem. Phys.*, 2006, 124, 22411 [x](#), [xi](#), [53](#), [54](#), [56](#)
- [100] A. Marenich et al., *Minnesota solvation database*, version 2009 (University of Minnesota Minneapolis) 2009. [x](#), [xi](#), [53](#), [54](#), [56](#)
- [101] C. J. Cramer and D. G. Truhlar, *J. Am. Chem. Soc.*, 1991, 113, 8305 [x](#), [xi](#), [53](#), [56](#)
- [102] M. Valiev, E. J. Bylaska, N. Govind, K. Kowalski, T. P. Straatsma, H. J. J. van Dam, D. Wang, J. Nieplocha, E. Apra, T. L. Windus, W. A. de Jong, “NWChem: a comprehensive and scalable open-source solution for large scale molecular simulations”, *Comput. Phys. Commun.*2010, 181, 1477 [42](#), [110](#)
- [103] M. Minato and P. Lahti, *J. Am. Chem. Soc.* 1997, 119, 2187 [xviii](#), [99](#), [100](#), [111](#)
- [104] S Nimura, O. Kikuchi, T. Ohana, A. Yabe, M. Kaise, *Chem. Lett.* 1996, 125. [111](#)
- [105] A. S. Ichimura, K. Sato, T. Kinoshita, T. Takui, K. Itoh, P. M. Lahti, *Mol. Cryst. Liq. Cryst. Sci., Technol., Sect. A* 1995, 272, 279. [111](#)
- [106] P. M. Lahti, A. S. Ichimura, and J. A. Sanborn, *J. Phys. Chem. A* 2001, 105, 251 [xiv](#), [107](#), [108](#), [110](#), [111](#), [112](#)

- [107] A. Reiser, G. Bowes, and R. J. Horne, *Trans. Faraday Soc.* 1966, 63, 3162. [13](#),
[112](#)
- [108] S. Leach, M. Vervloet, A. Desprs et al., *Chem. Phys.* 1992, 160, 451. [112](#)
- [109] R. J. Harrison, *J. Chem. Phys.* 1991, 94, 5021. [102](#)
- [110] M. G. Papadopoulos J. Waite, *J. Chem. Phys.* 1985, 82, 1435 [88](#)
- [111] S. Duan, X. Xu, Y. Luo and Zhong-Qun Tian, *Chem. Commun*, 2011, 47, 11438
[89](#)
- [112] P. R. Hilton, and D. W. Oxtoby, *J. Chem. Phys.*, 1980, 72, 6346 [81](#)
- [113] W. C. Meixner, P. R. Antoniewicz, *Phy. Rev. B*, 1976, 13, 3276 [81](#)
- [114] O. Andeussi, I. Dabo, and N. Marzari, *J. Chem. Phys.* 2012, 136, 064102 [128](#)

Appendix

The optimized geometries of molecules reported herein were optimized using NWchem. The optimized geometries all passed the frequency analysis test.

Benzene

(C_6H_6)

units angstrom

C	0.98756089	0.98756089	0.00000000
C	1.34903326	-0.36147237	0.00000000
C	0.36147237	-1.34903326	0.00000000
C	-0.36147237	1.34903326	0.00000000
C	-1.34903326	0.36147237	0.00000000
C	-0.98756089	-0.98756089	0.00000000
H	1.75619462	1.75619462	0.00000000
H	2.39900646	-0.64281184	0.00000000
H	0.64281184	-2.39900646	0.00000000
H	-0.64281184	2.39900646	0.00000000
H	-2.39900646	0.64281184	0.00000000
H	-1.75619462	-1.75619462	0.00000000

Water

(H_2O)

units angstrom

O	0.00000000	0.00000000	-0.11468157
H	-0.75406337	0.00000000	0.45872629
H	0.75406337	0.00000000	0.45872629

Methane

(CH_4)

units angstrom

C	0.00000117	-0.00000369	-0.00000005
H	0.57425115	-0.32269179	0.86047787
H	0.50317965	-0.31185326	-0.90767522
H	-0.09018211	1.07984942	0.01024417
H	-0.98725568	-0.44528227	0.03695350

Acetamide

(CH_3CONH_2)

units angstrom

C	1.28901920	-0.50920515	-0.17082984
C	-0.05141456	0.15792861	0.05145078
N	-1.12848330	-0.66073005	-0.08402011
O	-0.16273189	1.31897421	0.32235204
H	2.08075108	0.14330333	0.26305691
H	1.45554474	-0.61984328	-1.28044749
H	1.31364497	-1.53150970	0.29902746
H	-2.03037970	-0.23725794	-0.08969604
H	-1.04395058	-1.57371645	-0.46634190

Nitroxide

(NO^+)

units angstrom

N	0.00000000	0.00000000	-0.58726848
O	0.00000000	0.00000000	0.51385992

Ammonia

(NH_3)

units angstrom

N	0.00000000	0.00000000	0.11108106
H	0.76718115	0.52856586	-0.25918915
H	0.07416089	-0.92868129	-0.25918915
H	-0.84134203	0.40011544	-0.25918915

Methanol

(CH_3OH)

units angstrom

C	0.01087820	0.65579786	0.00000000
O	0.08603762	-0.74180734	0.00000000
H	-0.49541386	1.03718656	0.88361625
H	-0.49541386	1.03718656	-0.88361625
H	1.02521341	1.02985813	0.00000000
H	-0.78795582	-1.10455976	0.00000000

Acetone



units angstrom

H	2.01607656	0.09998687	0.80468344
C	1.40653656	0.07888687	-0.10790656
H	1.63321656	0.98648687	-0.68240656
H	1.73050656	-0.78252312	-0.70638656
C	-0.06876344	-0.00633312	0.17641344
O	-0.51074344	-0.04752312	1.30894344
C	-0.96042344	-0.03737313	-1.03539656
H	-0.81540344	0.86741687	-1.63990656
H	-0.71669344	-0.90147312	-1.66707656
H	-2.02585344	-0.10079312	-0.77911656

Nitrate



units angstrom

N	0.00000000	0.00000000	0.00011378
O	0.00000000	0.00000000	1.22602830
O	-1.06147167	0.00000000	-0.61306393
O	1.06147167	0.00000000	-0.61306393

Cyanide

(CN^-)

units angstrom

C	0.00000000	0.00000000	-0.62297196
N	0.00000000	0.00000000	0.53397596

1,2-Ethanediol

($HOCH_2CH_2OH$)

units angstrom

C	0.51272494	-0.55627861	0.00000000
C	-0.51272494	0.55627861	0.00000000
O	-0.19084936	-1.76989708	0.00000000
O	0.19084936	1.76989708	0.00000000
H	1.14414533	-0.46154471	-0.87938136
H	1.14414533	-0.46154471	0.87938136
H	-1.14414533	0.46154471	-0.87938136
H	-1.14414533	0.46154471	0.87938136
H	0.41945418	-2.49296713	0.00000000
H	-0.41945418	2.49296713	0.00000000

Propapanoic Acid

($CH_3CH_2CO_2H$)

units angstrom

C	-0.09418117	1.96232856	0.00000000
C	0.73607627	0.68506541	0.00000000
C	-0.10491519	-0.56547060	0.00000000
O	-1.29172331	-0.60940658	0.00000000
O	0.64676539	-1.66543521	0.00000000
H	-0.73124732	2.01272628	0.87452364
H	-0.73124732	2.01272628	-0.87452364
H	0.55638167	2.83008261	0.00000000
H	1.38886352	0.63591958	0.86644012
H	1.38886352	0.63591958	-0.86644012
H	0.06616984	-2.42018015	0.00000000

Methylammonium	$(CH_3NH_3^+)$	units angstrom		
	N	0.00000000	0.00000000	-0.70803263
	C	0.00000000	0.00000000	0.79775348
	H	0.03360854	0.93945487	-1.07777462
	H	0.79678751	-0.49883329	-1.07777462
	H	-0.83039606	-0.44062158	-1.07777462
	H	0.90508977	0.48025235	1.13434380
	H	-0.03663415	-1.02395691	1.13434380
	H	-0.86845562	0.54370456	1.13434380

Methyl ether hydronium $(CH_3OHCH_3^+)$

units angstrom

	C	-0.24320296	0.01602474	1.27596507
	C	-0.24320296	0.01602474	-1.27596507
	O	0.50249447	0.02389681	0.00000000
	H	1.26451655	-0.54881361	0.00000000
	H	-0.87733962	0.88507503	1.24554394
	H	-0.80472182	-0.90244713	1.33765730
	H	0.49904300	0.10004323	2.05138782
	H	-0.87733962	0.88507503	-1.24554394
	H	0.49904300	0.10004323	-2.05138782
	H	-0.80472182	-0.90244713	-1.33765730

Dichloroacetate	$(CHCl_2CO_2^-)$	units	angstrom	
	C	-0.30025730	-0.11193841	0.43153365
	C	1.16373270	0.22335159	0.35836365
	O	1.53734270	1.30775159	-0.06085635
	O	2.07544270	-0.67994841	0.76646365
	Cl	-1.33451730	1.23214159	-0.13093635
	Cl	-0.63705730	-1.54699841	-0.56725635
	H	-0.56636730	-0.33833841	1.48503365
Pyridinium	$(C_5H_5NH^+)$	units	angstrom	
	H	0.00000000	0.00000000	-2.29800577
	N	0.00000000	0.00000000	-1.29708352
	C	0.00000000	1.17603384	-0.66040538
	C	0.00000000	-1.17603384	-0.66040538
	C	0.00000000	1.20596207	0.70982540
	C	0.00000000	-1.20596207	0.70982540
	C	0.00000000	0.00000000	1.40143789
	H	0.00000000	2.05665415	-1.27267201
	H	0.00000000	-2.05665415	-1.27267201
	H	0.00000000	2.14785573	1.22256214
	H	0.00000000	-2.14785573	1.22256214
	H	0.00000000	0.00000000	2.47614261

Pyridine (C_5H_5N)

units angstrom

H	0.00000000	0.00000000	4.67254596
C	0.00000000	0.00000000	2.61854584
C	0.00000000	-2.26500278	1.27196744
H	0.00000000	-4.07772320	2.23478328
C	0.00000000	-2.15844324	-1.36437713
H	0.00000000	-3.89230327	-2.47324704
N	0.00000000	0.00000000	-2.68542530
C	0.00000000	2.15844324	-1.36437713
H	0.00000000	3.89230327	-2.47324704
C	0.00000000	2.26500278	1.27196744
H	0.00000000	4.07772320	2.23478328

1,4-Phenylenedinitrene

($C_6H_4N_2$)

CASSCF[10, 10]

Singlet

units angstrom

C	0.00000000	1.38949273	0.00000000
C	-1.26365775	0.66347452	0.00000000
C	-1.26365775	-0.66347452	0.00000000
C	0.00000000	-1.38949273	0.00000000
C	1.26365775	-0.66347452	0.00000000
C	1.26365775	0.66347452	0.00000000
H	-2.16718824	1.23245129	0.00000000
H	-2.16718824	-1.23245129	0.00000000
H	2.16718824	-1.23245129	0.00000000
H	2.16718824	1.23245129	0.00000000
N	0.00000000	-2.64265911	0.00000000
N	0.00000000	2.64265911	0.00000000

1,4-Phenylenedinitrene

($C_6H_4N_2$)

CASSCF[10, 10]

triplet

units angstrom

C	0.00000000	1.37821878	0.00000000
C	-1.26878034	0.66563197	0.00000000
C	-1.26878034	-0.66563197	0.00000000
C	0.00000000	-1.37821878	0.00000000
C	1.26878034	-0.66563197	0.00000000
C	1.26878034	0.66563197	0.00000000
H	-2.17004437	1.24037479	0.00000000
H	-2.17004437	-1.24037479	0.00000000
H	2.17004437	-1.24037479	0.00000000
H	2.17004437	1.24037479	0.00000000
N	0.00000000	-2.62786693	0.00000000
N	0.00000000	2.62786693	0.00000000

4,4'-Stilbenedinitrene ($C_{14}H_{10}N_2$)		CASSCF[6, 6]	Singlet	
units angstrom				
C	-0.11417471	4.72436535	0.00000000	
C	1.24319142	4.11191330	0.00000000	
C	1.39111300	2.79449856	0.00000000	
C	-1.26984871	3.78301465	0.00000000	
C	0.25412971	1.85650286	0.00000000	
C	-1.08730343	2.46869129	0.00000000	
C	0.49419432	0.53323056	0.00000000	
C	-0.49419432	-0.53323056	0.00000000	
C	-0.25412971	-1.85650286	0.00000000	
C	1.08730343	-2.46869129	0.00000000	
C	1.26984871	-3.78301465	0.00000000	
C	0.11417471	-4.72436535	0.00000000	
C	-1.24319142	-4.11191330	0.00000000	
C	-1.39111300	-2.79449856	0.00000000	
N	-0.28212035	5.96980015	0.00000000	
N	0.28212035	-5.96980015	0.00000000	
H	2.09001516	4.77152070	0.00000000	
H	2.37792185	2.36577550	0.00000000	
H	-2.25573512	4.20750428	0.00000000	

	H	-1.94597628	1.82540894	0.00000000
	H	1.52647172	0.23654159	0.00000000
	H	-1.52647172	-0.23654159	0.00000000
	H	1.94597628	-1.82540894	0.00000000
	H	2.25573512	-4.20750428	0.00000000
	H	-2.09001516	-4.77152070	0.00000000
	H	-2.37792185	-2.36577550	0.00000000
4,4'-Stilbenedinitrene	($C_{14}H_{10}N_2$)	CASSCF[6, 6]	Triplet	
units	angstrom			
	C	-0.11785639	4.73011638	0.00000000
	C	1.24674423	4.11197071	0.00000000
	C	1.39715861	2.79549066	0.00000000
	C	-1.27163546	3.77709819	0.00000000
	C	0.26090928	1.85389833	0.00000000
	C	-1.08249187	2.46397820	0.00000000
	C	0.49837834	0.53046182	0.00000000
	C	-0.49837834	-0.53046182	0.00000000
	C	-0.26090928	-1.85389833	0.00000000
	C	1.08249187	-2.46397820	0.00000000
	C	1.27163546	-3.77709819	0.00000000

4,4'-Stilbenedinitrene(cont)	($C_14H_10N_2$)	CASSCF[6, 6]	Triplet	
C	0.11785639	-4.73011638	0.00000000	
C	-1.24674423	-4.11197071	0.00000000	
C	-1.39715861	-2.79549066	0.00000000	
N	-0.28421831	5.97519444	0.00000000	
N	0.28421831	-5.97519444	0.00000000	
H	2.09238729	4.77408931	0.00000000	
H	2.38548684	2.36966018	0.00000000	
H	-2.25987145	4.19806332	0.00000000	
H	-1.93975856	1.81864666	0.00000000	
H	1.52945916	0.22878845	0.00000000	
H	-1.52945916	-0.22878845	0.00000000	
H	1.93975856	-1.81864666	0.00000000	
H	2.25987145	-4.19806332	0.00000000	
H	-2.09238729	-4.77408931	0.00000000	
H	-2.38548684	-2.36966018	0.00000000	

Vita

Jacob Fosso Tande was born on January 26th, 1976 in the small village of Bamougoum in the west region of the Republic of Cameroon. He completed elementary education at the Government Bilingual Primary School in his home town of Bafoussam. He spent the first 3 years of his secondary education at Unity Bilingual Academy in Bafoussam after which he moved to the Government Bilingual High School where in 1994, he graduated with a GCE/OL. In 1996 he graduated from the Government Bilingual High School, Mbengwi (North West region of Cameroon) with a GCE/AL. At the University of Buea in Cameroon, he studied Chemistry, with minor in Chemical Process Technology and graduated in 2002 with a Bachelor of science in Chemistry. After Teaching high school Chemistry and Physics for three years, he started graduate school in 2005, at East Tennessee State University (Johnson City, Tennessee, U.S.A) where he graduated, in 2007, with a Masters of science in Chemistry and moved on to obtained a PhD in Chemistry in 2012 from the University of Tennessee in Knoxville (Tennessee, U.S.A)